

Microwave Noise Detection of a Quantum Dot with Stub Impedance Matching

Inauguraldissertation

zur
Erlangung der Würde eines Doktors der Philosophie
vorgelegt der
Philosophisch-Naturwissenschaftlichen Fakultät
der Universität Basel

von

**Thomas Hasler
aus Hellikon AG**

Basel, 2016

Originaldokument gespeichert auf dem Dokumentenserver der Universität Basel
edoc.unibas.ch

Genehmigt von der Philosophisch-Naturwissenschaftlichen Fakultät
auf Antrag von

Prof. Dr. Christian Schönenberger
Prof. Dr. Thomas Ihn
Dr. Fabien Portier

Basel, 24.5.2016

Prof. Dr. Jörg Schibler
Dekan

Contents

1. Introduction	1
2. Microwave Transmission Lines	3
2.1. Lumped-Element Circuit Model for Transmission Lines	3
2.1.1. The Telegraph Equations	3
2.1.2. Wave Solutions of the Telegraph Equations	4
2.1.3. Low-Loss Approximation	6
2.2. Terminated Transmission Line	6
2.3. Coplanar Transmission Line	8
2.3.1. Basic Properties	8
2.3.2. Kinetic Inductance	11
2.4. Transmission Line Resonators	11
2.4.1. Scattering Parameters	13
2.4.2. Resonator Basics	14
2.4.3. Loss Mechanisms	15
2.4.4. Measurements at 4.2 K	16
2.5. Miscellaneous	18
2.5.1. Transmission Line versus Waveguide	18
2.5.2. Why 50 Ω ?	18
3. Impedance Matching	19
3.1. Stub Impedance-Matching Circuit	20
3.1.1. Matching with a Lossless Stub Tuner	20
3.1.2. Input Impedance of a Stub Tuner	22
3.1.3. Reflectance of a Lossless Stub Tuner	23
3.1.4. Effect of Losses	25
3.1.5. Reflection Measurements of an Open Stub Tuner	26
3.1.6. Output Impedance of a Stub Tuner	28
3.1.7. Transmission Coefficient of a Stub Tuner	29
3.1.8. Figure of Merit for Noise Measurements	32
3.2. <i>LC</i> Matching Network	34
3.2.1. Basic Properties	34
3.2.2. Towards a Microwave Realisation	37
3.3. Bode-Fano Criterion	38
4. Fabrication of Carbon Nanotube Samples	39
4.1. Carbon Nanotube Stamping	39
4.1.1. Carbon Nanotube Growth	39
4.1.2. How to Get an On-Chip Stub Tuner	40
4.1.3. Stamping Procedure	40

4.2. Fabrication Steps	42
4.2.1. Bottom Gates	42
4.2.2. Stub Tuner	43
4.2.3. Normal Metal Contacts to Carbon Nanotubes	45
4.2.4. Superconducting Niobium Contacts to Carbon Nanotubes	46
4.2.5. Lead Contacts to Carbon Nanotubes	47
5. Microwave Measurement Setup	49
5.1. Sample Puck	50
5.2. RF Wiring	51
5.3. DC Wiring	52
5.4. Possible Improvements of RF Wiring	54
5.5. RF Dipstick	55
6. Conductance in the Quantum Dot Regime	56
6.1. Electronic Structure of Carbon Materials	56
6.1.1. Graphene Bandstructure	56
6.1.2. From Graphene to Carbon Nanotubes	57
6.2. Quantum Dots in Carbon Nanotubes	58
6.2.1. Quantum Dot States	59
6.2.2. Transport through Quantum Dots	61
6.2.3. Double Quantum Dots	63
6.3. Conductance Measurements of a Quantum Dot	64
6.3.1. Stub Tuner Characterisation	67
6.3.2. DC and RF Conductance	68
6.4. Quantum Dot with One Niobium Lead	70
6.5. Reflectometry on a Carbon Nanotube Double Dot	72
7. Noise Measurements with Stub Impedance Matching	74
7.1. Noise Characteristics	74
7.1.1. Thermal Noise	75
7.1.2. Shot Noise	76
7.1.3. Shot Noise in Different Wire Regimes	77
7.1.4. Other Noise Sources	78
7.1.5. Quantum Noise	79
7.2. Noise Detection Techniques	79
7.2.1. Low-Frequency Cross-Correlation	79
7.2.2. Resonant Circuit for Intermediate Frequencies	80
7.2.3. High-Frequency Schemes Using Rectifying Elements	81
7.2.4. Full Counting Statistics	83
7.3. Noise Detection with a Stub Tuner	83
7.3.1. Setup Analysis	83
7.3.2. Setup Gain Calibration	85
7.4. Noise Measurements in the Single Dot Regime	88
7.4.1. Stub Tuner Transmission	88
7.4.2. Noise Calibration	89
7.4.3. Shot-Noise Results	90

8. Summary and Outlook	94
Bibliography	102
A. Derivations of $\lambda/4$-Resonator Formulas	103
A.1. Quality Factors	103
A.2. Input Impedance	104
A.3. Resonance Frequency	106
A.4. Transmission Coefficient	106
B. Derivations of Stub Tuner Formulas	108
B.1. Reflection	108
B.1.1. General Expression	108
B.1.2. Lossless Stub Tuner with Large Load Resistance	109
B.2. Transmission	112
B.2.1. Voltage Coefficients	112
B.2.2. Lossless Stub Tuner with Large Load Resistance	114
C. Fabrication Recipes	116
D. List of Setup Components	121
Curriculum Vitae	123
Publications	124
Acknowledgements	125

1 Introduction

Noise is defined as random fluctuations of a signal in time. The fundamental requirement for noise is some sort of randomness. Noise is well-known and infamous to every experimentalist - whether he is working in the field of electronics, optics, acoustics or anywhere else - since such fluctuations are inherent and unavoidable in many systems.

For most of us, the word noise has a negative connotation. It is considered to be an unwanted disturbance superposed on a useful signal, which tends to obscure the signal's information. The natural reaction to this nuisance is trying to reduce it as much as possible, be it with a longer averaging time or an improved setup. In this respect, the signal-to-noise ratio, which compares the level of the desired signal with the level of the superposed noise, is the relevant quantity. A signal-to-noise level larger than one has to be achieved in order to observe the requested signal. In fact, noise is often a limiting factor in experiments and there are many examples where a reduced noise level led to the revelation of unexpected features.

In this sense, noise seems to be a tedious, annoying matter and it is a fair question to ask why one would make it the topic of an entire thesis. While noise is primarily an experimental affair, theoretical studies on the statistics of these fluctuations have been carried out for a long time, too. These studies draw an interesting picture. Measuring the average current through a system delivers partial information on the mechanisms responsible for conduction. But a more complete description and further information on the conduction mechanisms are given by the probability distribution of the current, containing both the average current and its fluctuations.

Even though the fluctuations appear randomly, they are caused by well-defined processes like the thermal motion of charges, the discreteness of charge carriers and the probabilistic character of scattering [1]. Each noise source exhibits distinct characteristics. Measuring the noise properties of a system and knowing the underlying process, one might be able to infer complementary insight beyond what is possible with the mean current. Hence, a profound knowledge of the noise processes does not only help to find a way for reducing the noise level, but can also be used as a diagnostic tool [2].

It was Einstein who realised in 1909 that electromagnetic fluctuations differ if the energy is carried by waves or particles [3]. He derived a linear relation between the mean energy and the corresponding fluctuations for waves, whereas the fluctuations scale with the square root of the mean energy for particles. Another example where fluctuations can provide information about the charge carriers was proposed by Schottky in 1918 in the context of vacuum tubes [4]. Shot noise (which is not a dangerous effect at all despite its name) arises from the granularity of charge and therefore scales with the unit of charge. Indeed, the doubled charge of Cooper pairs [5] and the fractional charge of Laughlin quasiparticles appearing in the fractional quantum Hall state [6, 7] was confirmed in this way. In 1928, the dependence of fluctuations due to thermal agitation was studied experimentally by Johnson [8] and theoretically by Nyquist [9]. In the following, the extrapolation of thermal noise to zero amplitude was used to determine

the absolute zero of temperature and a value for the Boltzmann constant was deduced from the temperature dependence of thermal noise.

Typical currents that occur in nanoelectronics are tiny. Current fluctuations coming from these samples are even smaller and more challenging to detect and one has to come up with a clever measurement scheme. We are mainly interested in shot noise, whose spectral density is frequency-independent up to a few gigahertz. In contrast, electronic components add an undesired noise contribution, which is inversely proportional to the frequency f . At gigahertz frequencies, the amplitude of this $1/f$ -noise is considerably reduced. Moreover, measuring at high frequencies has a second advantage. Higher frequencies enable us to measure with a larger bandwidth and consequently to acquire more signal. For these reasons, we started the noise project by building up a microwave measurement scheme.

Our main interest lies in noise studies of high-resistance mesoscopic devices, such as quantum dots. However, the combination of high-frequency measurements with impedances on the order of $R = 100 \text{ k}\Omega$ suffers from the large impedance mismatch to the standard characteristic impedance of the measurement line, $Z_0 = 50 \text{ }\Omega$. According to voltage division, the suppression of detectable signal power on the $50 \text{ }\Omega$ side is on the order of $(Z_0/R)^2$. Hence, there is a solution needed to enhance the transmission from the device to the instrument. This is achieved with impedance matching, for which we use a so-called stub impedance-matching circuit. It is a resonant circuit based on transmission lines.

This thesis about noise detection with a stub impedance-matching circuit is structured as follows: It starts in chapter 2 with an introduction to the characteristics of microwave transmission lines, which are the building blocks of the later used microwave circuit. The development of carbon nanotube samples with an integrated stub impedance-matching circuit for noise detection as well as building up the high-frequency measurement setup were important experimental parts of this PhD project. For this reason, it is documented in detail in the thesis. A description of the stub impedance-matching circuit's properties is found in chapter 3. It also mentions impedance matching with an LC circuit and ends with a comparison of the two approaches. All fabrication considerations and recipes are collected in chapter 4. Chapter 5 gives an overview of the measurement setup, which is partially inside a dilution refrigerator. The remaining two chapters are devoted to results from a quantum dot formed in a carbon nanotube. Chapter 6 discusses RF reflectometry in the presence of a stub impedance-matching circuit. It is shown how to extract the circuit parameters and the device impedances from the reflection spectrum. Finally, noise measurements and their analysis are presented in chapter 7. The good agreement of our noise data in the single quantum dot regime with previous studies is a confirmation that the developed methods for noise detection with stub impedance matching and for calibration are well suited and allow for accurate noise results.

2 Microwave Transmission Lines

This introductory chapter is devoted to the question how to transmit microwave signals and how to characterise such transmission lines. It provides some background for the radio-frequency (RF) circuits discussed in subsequent chapters.

In simple words, a transmission line is an arrangement of conductors for a guided wave propagation. After explaining in general how to model a transmission line and introducing the basic quantities, the following section focuses on coplanar transmission lines. Later, transmission line resonators are discussed and it is demonstrated in theory and experimentally how they can be used to determine the properties of transmission lines.

2.1. Lumped-Element Circuit Model for Transmission Lines ¹

The description of circuit elements differs strongly if the wavelength of the electrical signal is much larger than or comparable with the element size. In the first case, the voltages and currents within the element are constant and a lumped-element description of the circuit is justified. This usually does not hold for gigahertz frequency signals since the voltages and currents are varying within a circuit element and hence a description with one lumped element is no longer accurate. Instead, it has to be treated as a distributed element.

A transmission line (TL) is clearly a distributed element. Still it can be modelled as a series of infinitesimal lumped-element pieces of length Δx . One of these pieces is shown in Fig. 2.1. In order to carry transverse electromagnetic (TEM) modes, a TL has to consist of (at least) two conductors, illustrated by the top and the bottom lines. The quantities R , G , L and C are all per unit length and describe the following properties:

- R is the series resistance for both conductors caused by conductor losses.
- G is the shunt conductance due to dielectric losses.
- L is the inductance of the two conductors.
- C is the capacitance between the conductors.

2.1.1. The Telegraph Equations

Considering the lumped-element model of TLs, standard circuit theory can be applied to derive the voltage and current distributions along a TL. Kirchhoff's voltage law applied to the circuit in Fig. 2.1 leads to the relation

$$\tilde{V}(x, t) - R\Delta x\tilde{I}(x, t) - L\Delta x\frac{\partial\tilde{I}(x, t)}{\partial t} - \tilde{V}(x + \Delta x, t) = 0, \quad (2.1)$$

¹This section closely follows chapter 2 in [10]

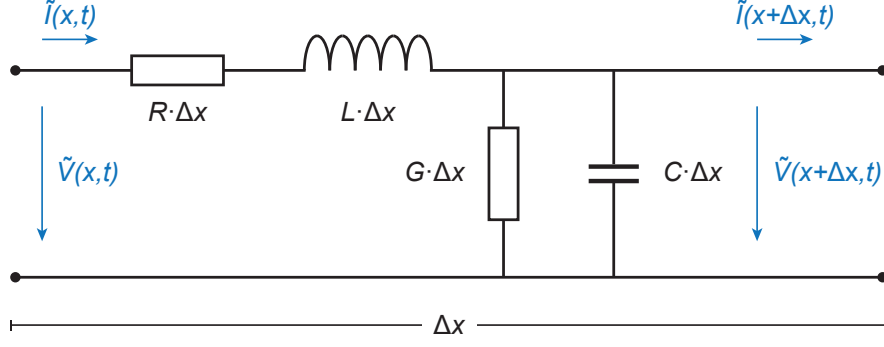


Figure 2.1.: Lumped-element circuit model for an incremental TL piece of length Δx . A description of the elements is found in the text.

and Kirchhoff's current law results in

$$\tilde{I}(x, t) - G\Delta x \tilde{V}(x + \Delta x, t) - C\Delta x \frac{\partial \tilde{V}(x + \Delta x, t)}{\partial t} - \tilde{I}(x + \Delta x, t) = 0. \quad (2.2)$$

Dividing both equations by Δx and taking the limit $\Delta x \rightarrow 0$ results in

$$\begin{aligned} \frac{\partial \tilde{V}(x, t)}{\partial x} &= -R\tilde{I}(x, t) - L\frac{\partial \tilde{I}(x, t)}{\partial t} \quad \text{and} \\ \frac{\partial \tilde{I}(x, t)}{\partial x} &= -G\tilde{V}(x, t) - C\frac{\partial \tilde{V}(x, t)}{\partial t}. \end{aligned} \quad (2.3)$$

These two coupled first order partial differential equations are called the telegraph equations. They can be combined to the following pair of equations:

$$\begin{aligned} \frac{\partial^2}{\partial x^2} \tilde{V} &= LC \frac{\partial^2}{\partial t^2} \tilde{V} + (RC + GL) \frac{\partial}{\partial t} \tilde{V} + RG\tilde{V} \\ \frac{\partial^2}{\partial x^2} \tilde{I} &= LC \frac{\partial^2}{\partial t^2} \tilde{I} + (RC + GL) \frac{\partial}{\partial t} \tilde{I} + RG\tilde{I}. \end{aligned} \quad (2.4)$$

2.1.2. Wave Solutions of the Telegraph Equations

Eqs. (2.4) describe voltages and currents along a TL. In the lossless case, when $R = G = 0$, only the first term on the right-hand side does not vanish and one ends up with wave equations for \tilde{V} and \tilde{I} , whose solutions are plane waves. One can extend the plane wave ansatz to the general lossy case and write

$$\begin{aligned} \tilde{V}(x, t) &= \text{Re}\{V(x) \cdot e^{i\omega t}\} \\ \tilde{I}(x, t) &= \text{Re}\{I(x) \cdot e^{i\omega t}\}, \end{aligned} \quad (2.5)$$

where ω is the angular frequency. $V(x)$ and $I(x)$ are the voltage and current amplitudes, respectively. With this ansatz, Eqs. (2.4) read

$$\begin{aligned} \frac{\partial^2}{\partial x^2} V(x) - \gamma^2 V(x) &= 0 \\ \frac{\partial^2}{\partial x^2} I(x) - \gamma^2 I(x) &= 0, \end{aligned} \quad (2.6)$$

where the complex propagation constant in units [1/m] is defined as

$$\gamma = \sqrt{(R + i\omega L)(G + i\omega C)} = \alpha + i\beta. \quad (2.7)$$

The general solutions to Eqs. (2.6) are

$$\begin{aligned} V(x) &= V^+ e^{-\gamma x} + V^- e^{\gamma x} \\ I(x) &= I^+ e^{-\gamma x} + I^- e^{\gamma x}, \end{aligned} \quad (2.8)$$

which is a superposition of right-moving and left-moving waves, whose amplitudes are denoted with plus and minus signs, respectively. A relation between current and voltage can be derived with the help of the telegraph equations (2.3):

$$I(x) = \frac{\gamma}{R + i\omega L} [V^+ e^{-\gamma x} - V^- e^{\gamma x}]. \quad (2.9)$$

The characteristic impedance Z_0 is defined as the ratio of the voltage to current amplitudes

$$Z_0 = \frac{V^+}{I^+} = -\frac{V^-}{I^-}. \quad (2.10)$$

Comparing Eq. (2.9) with the second line of Eq. (2.8) leads to the expression for the characteristic impedance

$$Z_0 = \frac{R + i\omega L}{\gamma} = \sqrt{\frac{R + i\omega L}{G + i\omega C}}. \quad (2.11)$$

The current of Eq. (2.8) can be written in the form

$$I(x) = \frac{V^+}{Z_0} e^{-\gamma x} - \frac{V^-}{Z_0} e^{\gamma x}. \quad (2.12)$$

By inserting the first line of Eq. (2.8) and the definition of γ in Eq. (2.7) into Eq. (2.5), the voltage along a TL becomes the form

$$\tilde{V}(x, t) = V^+ \cdot e^{-\alpha x} \cos(\omega t - \beta x) + V^- \cdot e^{\alpha x} \cos(\omega t + \beta x). \quad (2.13)$$

The real part of the propagation constant γ in Eq. (2.7), α , causes an amplitude damping. The movement of the wave is given by the cosine terms. Considering the first term, to stay on a fixed point of the wave requires that the argument $\omega t - \beta x = \text{const.}$ With increasing time t , the position x is moving to the positive direction. The phase velocity is the speed at which a specific point x on the wave is changing position:

$$v_p = \frac{dx}{dt} = \frac{d}{dt} \left(\frac{\omega t - \text{const.}}{\beta} \right) = \frac{\omega}{\beta} = \lambda f, \quad (2.14)$$

with the wavelength $\lambda = \frac{2\pi}{\beta}$ being the peak to peak distance at a certain time.

The wavenumber for a plane wave in a lossless medium is given by the permittivity ϵ and the permeability μ and reads $k = \omega \sqrt{\mu \epsilon}$. The dielectric constant (or relative permittivity) $\epsilon_r = \frac{\epsilon}{\epsilon_0}$ is defined relative to the permittivity of free space, ϵ_0 . In the same way, the relative permeability $\mu_r = \frac{\mu}{\mu_0}$ is defined with respect to the permeability of free space, μ_0 . The propagation constant reads with these relative parameters $k = \omega \frac{\sqrt{\epsilon_r \mu_r}}{c}$. Here, we have used that the speed of light is

$c = \frac{1}{\sqrt{\epsilon_0 \mu_0}}$. In order to extend the free propagation of plane waves in an homogeneous medium to the guided wave propagation in a TL, we set the imaginary part of the wavenumber $\beta = k$, leading to

$$\beta = \omega \frac{\sqrt{\epsilon_{\text{eff}}}}{c}. \quad (2.15)$$

Here, it is assumed that $\mu_r = 1$ and the effect of the dielectric substrate and the TL geometry are combined in the effective dielectric constant ϵ_{eff} . According to Eq. (2.14), a phase velocity $v_p = c/\sqrt{\epsilon_{\text{eff}}}$ is obtained. Since it is frequency independent, there is no dispersion in a TL.

2.1.3. Low-Loss Approximation

In most practical cases, especially when using superconducting metals, the loss α is small, which allows to make some useful approximations. Stopping the Taylor expansion of the propagation constant γ given in Eq. (2.7) after the first two terms leads to

$$\gamma \approx \frac{1}{2} \left(R \sqrt{\frac{C}{L}} + G \sqrt{\frac{L}{C}} \right) + i \cdot \omega \sqrt{LC}, \quad (2.16)$$

and thus the wavenumber $\beta \approx \omega \sqrt{LC}$ is the same as in the lossless case. In the same way, the characteristic impedance of Eq. (2.10) can be approximated to

$$Z_0 \approx \sqrt{\frac{L}{C}}, \quad (2.17)$$

which is again the same as for a lossless TL.

2.2. Terminated Transmission Line

So far, infinitely long TLs were considered. Now, the we will discuss the effect of a load impedance Z_L terminating the TL as sketched in Fig. 2.2.

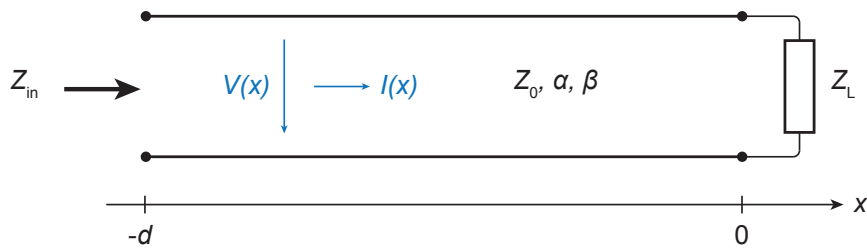


Figure 2.2.: Schematic of a transmission line with length d , characteristic impedance Z_0 , loss α and wavenumber β , which is terminated by a load impedance Z_L .

We start by assuming that a right-moving wave of the form $V^+ \cdot e^{-i\gamma x}$ is excited at the left side of the TL. At this moment, the voltage to current ratio is Z_0 . But this ratio has to be Z_L after the wave arrived at the load resistance. To fulfil this condition, a second reflected

wave has to be evoked. In general, the total voltage and current on the line have the form [see Eq. (2.8)]

$$\begin{aligned} V(x) &= V^+ e^{-\gamma x} + V^- e^{\gamma x} \\ I(x) &= \frac{V^+}{Z_0} e^{-\gamma x} - \frac{V^-}{Z_0} e^{\gamma x}. \end{aligned} \quad (2.18)$$

The boundary condition at the end of the line ($x = 0$) mentioned above requires that

$$Z_L = \frac{V(0)}{I(0)} = Z_0 \cdot \frac{V^+ + V^-}{V^+ - V^-}. \quad (2.19)$$

Solving for the amplitude ratio of reflected to incident voltage, called the reflection coefficient, gives

$$\Gamma = \frac{V^-}{V^+} = \frac{Z_L - Z_0}{Z_L + Z_0}. \quad (2.20)$$

Generalising Eq. (2.19) to a distance d away from the load leads to

$$Z_{\text{in}} = \frac{V(-d)}{I(-d)} = Z_0 \cdot \frac{V^+ e^{i\gamma d} + V^- e^{-i\gamma d}}{V^+ e^{i\gamma d} - V^- e^{-i\gamma d}}. \quad (2.21)$$

By using the boundary condition at $d = 0$ [Eq. (2.19)], the input impedance looking towards the load at a distance d can be brought to the form

$$Z_{\text{in}}(d) = Z_0 \cdot \frac{Z_L + Z_0 \tanh(\gamma d)}{Z_0 + Z_L \tanh(\gamma d)}. \quad (2.22)$$

In words, the impedance along the TL - the ratio of the total incoming and reflected voltage to the total current - becomes position dependent. Due to the imaginary part of γ , $Z_{\text{in}}(d)$ is periodic.

The two special cases of an open ($Z_L = \infty$) and a short end ($Z_L = 0$) are like mirrors for microwaves. The reflection coefficient Γ of Eq. (2.20) is $+1$ and -1 respectively. And Eq. (2.22) for the impedance along the TL simplifies to

$$\begin{aligned} Z_{\text{open}} &= Z_0 \coth(\gamma d) \\ Z_{\text{short}} &= Z_0 \tanh(\gamma d). \end{aligned} \quad (2.23)$$

One can also calculate the average power in the line at position d by combining Eqs. (2.18) and (2.20) to be

$$P = \frac{1}{2} \text{Re}\{V(d)^* I(d)\} = \frac{1}{2} \frac{|V^+|^2}{Z_0} (1 - |\Gamma|^2), \quad (2.24)$$

where the star symbol (*) denotes the complex conjugate. The equation shows that the power is constant along the line (independent of d), even though the impedance is changing periodically. In the case of a matched load impedance, when $\Gamma = 0$, all the incident power $\frac{1}{2} \frac{|V^+|^2}{Z_0}$ is delivered to the load while if Γ is non-zero, a fraction $|\Gamma|^2$ of the power is reflected.

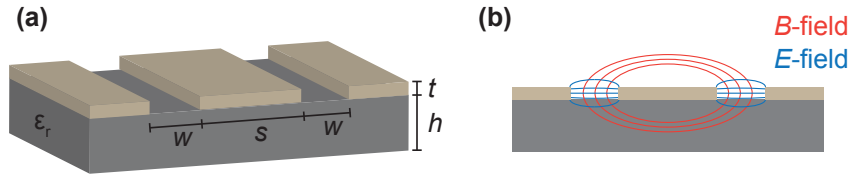


Figure 2.3.: (a) Illustration of a coplanar transmission line. The centre conductor width is s and the size of the gap to the ground planes is w . The metal thickness is t and the substrate thickness h . (b) Electric and magnetic field lines of the fundamental quasi-TEM mode.

2.3. Coplanar Transmission Line

A coplanar transmission line (CTL), as sketched in Fig. 2.3 (a), is composed of a centre conductor and ground planes on both sides. All conductors are on the same plane, which makes them convenient to fabricate and which is probably the reason why CTLs are so widespread.

The centre conductor of width s is separated by a gap of size w from the ground planes on both sides. These metallic parts of thickness t lie on a substrate of height h and with dielectric constant ϵ_r . To minimise the conductor losses, we use niobium, which becomes superconducting below 9.25 K. As a substrate, we take undoped silicon with a thin layer of silicon oxide on top. It is important to have an undoped substrate because free charge carriers in the substrate would absorb energy from the microwave field and hence would increase the dielectric loss significantly. The silicon oxide layer helps for the fabrication, as explained later in the fabrication section 4.2.2.

2.3.1. Basic Properties

The fundamental, preferred mode in a CTL is quasi-TEM, meaning that it is a TEM mode in a good approximation [11]. A rough sketch of the electric and magnetic field lines is shown in Fig. 2.3 (b).

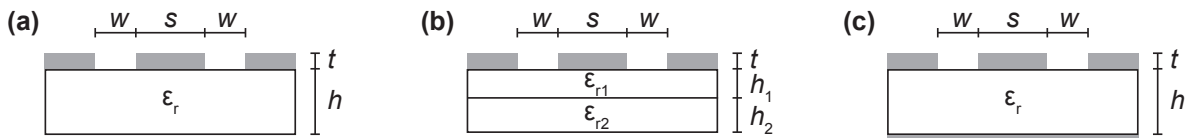


Figure 2.4.: Cross-sections through different kinds of coplanar transmission lines. The grey area is metal and the white are dielectric. (a) Basic type as already shown in Fig. 2.3. (b) Substrate consisting of two dielectric layers. (c) With grounded back plane.

The CTL dimensions and the dielectric constant of the substrate determine its characteristic impedance Z_0 and its wavenumber β . For this, the conformal mapping method can be used. It basically maps the CTL geometry to a plate capacitor, for which it is straightforward to derive the desired quantities. A cross-section through the basic CTL type is shown in Fig. 2.4 (a). If the finite metal thickness t is neglected, which is a good approximation since usually this is by

far the smallest dimension of the structure, the effective dielectric constant is found to be [12]

$$\epsilon_{\text{eff}} = 1 + \frac{\epsilon_r - 1}{2} \cdot \frac{K(k_1)K(k'_0)}{K(k'_1)K(k_0)}. \quad (2.25)$$

The functions K are the complete elliptical integrals of the first kind. Their arguments are defined by the CTL geometry as

$$\begin{aligned} k_0 &= \frac{s}{s + 2w} \\ k'_0 &= \sqrt{1 - k_0^2} \\ k_1 &= \frac{\sinh(\pi s/4h)}{\sinh(\pi(s + 2w)/4h)} \\ k'_1 &= \sqrt{1 - k_1^2}. \end{aligned} \quad (2.26)$$

The wavenumber β is related to the effective dielectric constant via Eq. (2.15). Moreover, the characteristic impedance is

$$Z_0 = \frac{30\pi}{\sqrt{\epsilon_{\text{eff}}}} \cdot \frac{K(k'_0)}{K(k_0)}. \quad (2.27)$$

Because of the elliptical integrals, the influence of the CTL parameters on Z_0 is not intuitive. Fig. 2.5 helps to capture the main characteristics. The dependence of Z_0 on the centre conductor width s and gap size w is plotted in Fig. 2.5 (a) when assuming a silicon substrate with $\epsilon_r = 11.9$ [10] and thickness $h = 500 \mu\text{m}$. $Z_0 = 50 \Omega$ is highlighted by the red contour line. As long as the substrate height h is by far the largest dimension ($h \gg s, w$), the characteristic impedance does almost not depend on h . It can be seen in Fig. 2.5 (b) that Z_0 is inversely proportional to the dielectric constant ϵ_r .

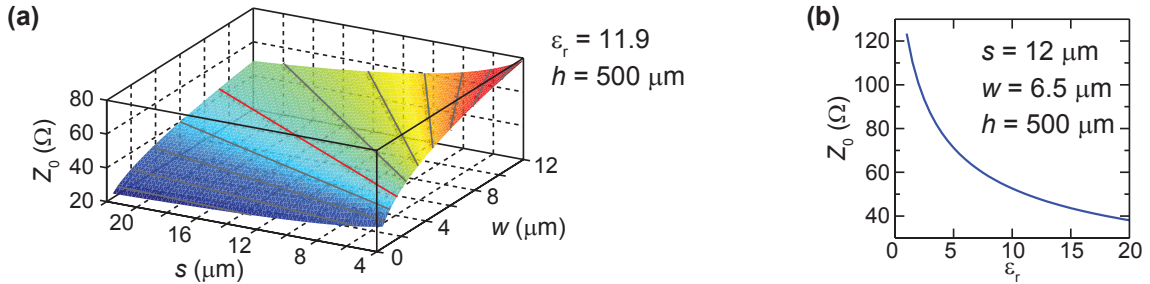


Figure 2.5.: **(a)** Characteristic impedance Z_0 of a CTL as a function of conductor width s and gap size w . Eq. (2.27) for a basic CTL as shown in Fig. 2.4 (a) is used. The red contour line marks $Z_0 = 50 \Omega$. **(b)** Dependence of Z_0 on the substrate's dielectric constant for a geometry on the red 50Ω line in panel (a).

The CTL properties are altered by other environment configurations, like a conducting back plane or a layered dielectric substrate. These are actually the situations occurring in our experiments, but the deviations to the results for a basic CTL given in Eqs. (2.25) and (2.27) are tiny in our cases.

Our Si/SiO₂ bilayer substrate has a SiO₂ top layer with dielectric constant ϵ_{r1} and a bulky Si bottom layer with ϵ_{r2} . For this bilayer substrate, as depicted in Fig. 2.4 (b), the formulas

are modified to [13]

$$\begin{aligned}\epsilon_{\text{eff}} &= 1 + \frac{\epsilon_{r1} - \epsilon_{r2}}{2} \cdot \frac{K(k_1)K(k'_0)}{K(k'_1)K(k_0)} + \frac{\epsilon_{r2} - 1}{2} \cdot \frac{K(k_2)K(k'_0)}{K(k'_2)K(k_0)} \\ Z_0 &= \frac{30\pi}{\sqrt{\epsilon_{\text{eff}}}} \cdot \frac{K(k'_0)}{K(k_0)}.\end{aligned}\quad (2.28)$$

If the top layer height is h_1 and the height of the bottom layer h_2 , the arguments of the elliptical integrals are

$$\begin{aligned}k_0 &= \frac{s}{s + 2w} \\ k_1 &= \frac{\sinh(\pi s/4h_1)}{\sinh(\pi(s + 2w)/4h_1)} \\ k_2 &= \frac{\sinh(\pi s/4(h_1 + h_2))}{\sinh(\pi(s + 2w)/4(h_1 + h_2))} \\ k'_i &= \sqrt{1 - k_i^2} \quad \text{with } i = 0, 1, 2.\end{aligned}\quad (2.29)$$

Even though the SiO_2 layer is closest to the CTL and thus penetrated by the largest fields, it only has a minor effect in our case since its thickness of 170 nm is very thin compared to the silicon thickness of 500 μm .

Printed circuit boards (PCBs) usually have a conducting back plane, which is also grounded. Also our samples are placed on a grounded plane. For this situation, as sketched in Fig. 2.4 (c), the formulas are [14]

$$\begin{aligned}\epsilon_{\text{eff}} &= \frac{1 + \epsilon_r \cdot \frac{K(k_1)K(k'_0)}{K(k'_1)K(k_0)}}{1 + \frac{K(k_1)K(k'_0)}{K(k'_1)K(k_0)}} \\ Z_0 &= \frac{60\pi}{\sqrt{\epsilon_{\text{eff}}}} \cdot \frac{1}{\frac{K(k_0)}{K(k'_0)} + \frac{K(k_1)}{K(k'_1)}},\end{aligned}\quad (2.30)$$

with the elliptical integral arguments

$$\begin{aligned}k_0 &= \frac{s}{s + 2w} \\ k_1 &= \frac{\tanh(\pi s/4h)}{\tanh(\pi(s + 2w)/4h)} \\ k'_i &= \sqrt{1 - k_i^2} \quad \text{with } i = 0, 1.\end{aligned}\quad (2.31)$$

It is not very surprising that a back plane behind a 500 μm -thick substrate does not affect the fields around the CTL much.

Nowadays, there also exists software to conduct electromagnetic simulations of CTLs and actually any structure you can imagine. They are especially helpful when dealing with more complex structures, for which analytical expressions are lacking, or to figure out parasitic effects of junctions, discontinuities and so on. In our lab we use Sonnet, a finite-element analysis software. It basically solves Maxwell's equations with the boundary conditions given by the structure by dividing the space into small boxes of constant electromagnetic fields.

2.3.2. Kinetic Inductance

As stated by Lenz' rule, a change of current through a conductor is opposed by a change in the induced magnetic field. The corresponding self-inductance or magnetic inductance for a CTL can be calculated with the conformal mapping technique [15]:

$$L_m = \frac{\mu_0}{4} \cdot \frac{K(k'_0)}{K(k_0)}. \quad (2.32)$$

In an ideal conductor, a change of current is additionally opposed by the mass of the charge carriers, since they have to be accelerated. Although the origin is different, the effect is the same as for a magnetic inductance and hence a second inductance, the kinetic inductance L_k is defined. For the kinetic inductance to be significant, the collision time of the charge carriers has to be much longer than the inverse of the AC signal frequency. Otherwise, the effect of accelerated charge carrier is lost rapidly by collisions. Therefore, kinetic inductance is only relevant in superconductors or in normal metals at optical frequencies.

Again, conformal mapping leads to an expression for the kinetic inductance of a superconducting CTL [15]:

$$L_k = \mu_0 \cdot \frac{\lambda_L(T)^2}{ts} \cdot g(s, w, t), \quad (2.33)$$

with the geometry factor g arising from conformal mapping to be

$$g = \frac{1}{2k_0^2 K(k_0)^2} \left[-\ln\left(\frac{t}{4s}\right) - \frac{s}{s+2w} \ln\left(\frac{t}{4(s+2w)}\right) + \frac{2(s+w)}{s+2w} \ln\left(\frac{g}{s+w}\right) \right]. \quad (2.34)$$

The London penetration depth λ_L is the depth to which supercurrents flow. Since the derivation for L_k assumes a uniform current distribution, Eq. (2.33) is only correct for thin films with thicknesses $t < 2\lambda_L$. If the thickness is larger, it might be more accurate to use $2\lambda_L$ instead of the actual thickness t .

The temperature dependence of the kinetic inductance is implicitly given by the penetration depth, which reads in the BCS theory [16]

$$\lambda_L(T) = \frac{\lambda_L(0)}{\sqrt{1 - (T/T_c)^4}} \quad (2.35)$$

Here, $\lambda_L(0)$ is the penetration depth at 0 K and T_c is the critical temperature. If the temperature is raising, λ_L increases and hence L_k as well. The reason for this increase of the kinetic inductance with decreasing Cooper pair density is that to maintain a constant current at a lower density, the velocity has to be higher and as a consequence the kinetic energy is higher, too. Kinetic inductance photon detectors [17] exploited the fact that photons impinging on superconducting CTLs break Cooper pairs and in turn change L_k of high-kinetic inductance superconductors.

In conclusion, the appearance of an extra series inductance in superconducting CTLs, the kinetic inductance L_k , causes a temperature dependent increase of the characteristic impedance Z_0 and a reduction of the resonance frequency of TL resonators, as seen later.

2.4. Transmission Line Resonators

As the name suggests, the purpose of TLs is to transmit microwave signals. Still, they can also be utilised to store electromagnetic waves when arranged into a resonant configuration.

According to Eq. (2.20), short and open TL ends completely reflect microwaves like a mirror. Thus, terminating a TL segment with an open or short end on both sides gives a Fabry-Pérot type resonator.

The shortest version of a TL resonator is a $\lambda/4$ -resonator and is schematically drawn in Fig. 2.6 (a). It consists of a TL segment that is a quarter of the fundamental resonance wavelength long and terminated by one open and one shorted end. The boundary condition at the open end is that the current is zero and therefore the voltage has a maximum. In contrast to the short end, where the current is maximal and the voltage zero. For a discrete set of frequencies, the waves bouncing back and forth in the resonator add up constructively to a standing wave. Fig. 2.6 (b) displays the fundamental mode voltage and current distributions along a $\lambda/4$ -resonator. This first mode contains one quarter of a full wave, the next higher mode three quarters and so on.

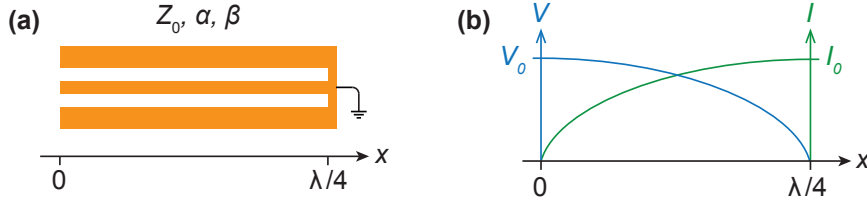


Figure 2.6.: (a) Illustration of a CTL segment of length $\lambda/4$ with an open and a shorted end. (b) Voltage and current amplitudes of the first resonant mode. This forms a so-called $\lambda/4$ -resonator.

Superconducting TL resonators are used nowadays in a variety of applications [18], be it for radiation detectors [17, 19], for parametric amplifiers [20, 21] or for circuit quantum electrodynamics [22]. Our application is more modest. We have seen that a CTL is completely characterised by knowing Z_0 , ϵ_{eff} and its damping α (see section 2.1.2). While the first two parameters can be calculated as described for CTLs in section 2.3.1, α strongly depends on the experimental conditions and TL materials and has therefore to be determined experimentally. In order to achieve a measurable effect caused by a tiny loss α , we make resonators with CTLs, such that the long signal lifetime in the resonator multiplies the effect of CTL losses.

In Fig. 2.7, there is a collection of pictures of our $\lambda/4$ -resonators. A theoretical description of their properties is given in this section and measurements are presented in section 2.4.4.

Fig. 2.7 (f) illustrates a cross-section of the resonators. We sputter a niobium film on a silicon/silicon oxide substrate and then use photo or electron-beam lithography followed by plasma etching to make the transmission line pattern. Details of this process are found in section 4.2.2.

For excitation and read-out, the resonators are capacitively coupled to the measurement line, as shown in Figs. 2.7 (b) and (d). The configuration in Fig. 2.7 (a) allows for reflectometry. One common line - connected to the bond pad on the left hand side - is used for the incoming and the reflected signal. On the other hand, the resonator can be coupled to a feedline as in Fig. 2.7 (c), through which the transmission is measured.

Compared to reflection, transmission measurements with a feedline have two advantages. Firstly, several resonators with different resonance frequencies can be coupled to one common feedline. Secondly, we observe a much weaker frequency dependence in transmission than in reflection. Our explanation for this goes as follows. Such a frequency dependence is caused by

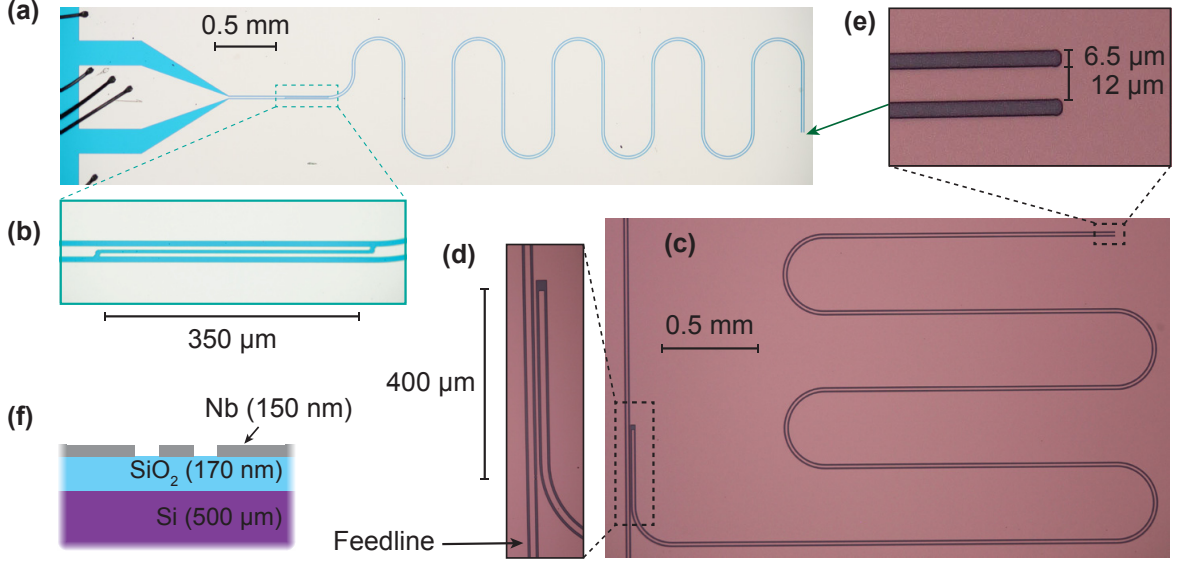


Figure 2.7.: Images of $\lambda/4$ -resonators with their first mode at about 3 GHz. **(a)** Configuration for reflection measurements. The input and output launcher is the pad on the left side. **(b)** Magnified coupling capacitor. **(c)** Configuration for transmission measurements by coupling to a feedline. **(d)** Coupling capacitor and **(e)** shorted end. **(f)** Sketch of the cross-section.

the interference with waves, which are reflected at imperfections along the line (for example at connectors). When measuring reflection, one reflection at an imperfection is enough to see an interference effect. But in transmission, only higher order processes including at least two reflections - one back and one forth - lead to an observable interference. These two advantages are the reason why we focus on transmission experiments in the following.

2.4.1. Scattering Parameters

A common way to describe the properties of microwave elements are scattering parameters or short S -parameters. Considering an general N -port network, they relate the wave amplitudes incident to the ports to those coming back from the ports. The amplitude of the incident voltage on port i is labelled V_i^+ and accordingly the voltage amplitude of the wave coming out from port i is labelled V_i^- . The amplitude vectors with N elements are related by the scattering matrix S via $\vec{V}^- = S\vec{V}^+$. A specific element of the scattering matrix is found by measuring the outgoing voltage V_i^- from port i when port j is driven by the voltage V_j^+ :

$$S_{ij} = \left. \frac{V_i^-}{V_j^+} \right|_{V_k^+ = 0 \text{ for } k \neq j} \quad \text{with } i, k, j = 1, 2, \dots, N. \quad (2.36)$$

The incident waves on all other ports than j have to be zero, which means that all ports must be terminated in matched loads to avoid reflections. These S -parameters can be accessed directly with a network analyser.

2.4.2. Resonator Basics

In the context of $\lambda/4$ -resonators coupled to a feedline as in Fig. 2.7 (c), S_{21} denotes the transmission coefficient from one to the other end of the feedline. It can be derived using the impedance formula for a TL [Eq. 2.22], as explained in appendix A. In the low-loss limit ($\alpha \ll 1$) and close to f_0 (the resonance frequency of the first mode) the transmission spectrum can be approximated by [23]

$$S_{21}(\Delta f) = \frac{S_{21}^{\min} + i \cdot 2Q_1 \frac{\Delta f}{f_0}}{1 + i \cdot 2Q_1 \frac{\Delta f}{f_0}}, \quad (2.37)$$

with the relative frequency defined with respect to the resonance frequency to be $\Delta f = f - f_0$. Here, the two fit parameters are S_{21}^{\min} , the amplitude of the resonance and Q_1 , the loaded quality factor. In fact, three additional fit parameter are used to account for the setup properties, as described at the end of appendix A.4. These are the background attenuation, its slope and an asymmetry factor to take into account contributions from standing waves in the setup.

While the relevant expressions for quality factors are given in the following, the derivations of these formulas are found in appendix A.1. The quality factor is a measure of the loss of a resonator. The lower the loss, the higher the quality factor. Furthermore, the quality factor is inversely proportional to the bandwidth or full width at half minimum Δ_{FWHM} of a resonance:

$$Q = \frac{f_0}{\Delta_{\text{FWHM}}}, \quad (2.38)$$

where Δ_{FWHM} is defined as the frequency range where the transmission coefficient S_{21} is less than $(1 + S_{21}^{\min})/2$.

The total, loaded quality factor Q_1 can be separated into an internal part Q_i arising from damping in the TL and a coupling part Q_c caused by leakage to the measurement line. The quality factors add like resistors in parallel:

$$\frac{1}{Q_1} = \frac{1}{Q_i} + \frac{1}{Q_c}. \quad (2.39)$$

In the so-called overcoupled regime [18], where $Q_c \ll Q_i$, the measured quality factor is dominated by Q_c . With C_c being the coupling capacitance, the coupling quality factor is

$$Q_c = \frac{1}{8\pi(fZ_0C_c)^2}. \quad (2.40)$$

In the other undercoupled limit, Q_1 is restricted by internal losses (expressed by Q_i), which is therefore the preferred regime to determine α . The internal quality factor is related to the CTL parameters via

$$Q_i = \frac{\beta}{2\alpha}, \quad (2.41)$$

where the wavenumber β is given by the CTL geometry, as discussed in section 2.3.1.

The relation of the resonance amplitude, the second fit parameter in Eq. (2.37), to the quality factors is

$$S_{21}^{\min} = \frac{Q_c}{Q_i + Q_c}. \quad (2.42)$$

Hence, the two parameters Q_1 and S_{21}^{\min} obtained by fitting a resonance spectrum to Eq. (2.37) can be transformed to another set of parameters with the help of Eqs. (2.39) and (2.42):

$$\begin{aligned} Q_i &= \frac{Q_1}{S_{21}^{\min}} \\ Q_c &= \frac{Q_1}{1 - S_{21}^{\min}}, \end{aligned} \quad (2.43)$$

which eventually allows to deduce the CTL loss α by using Eq. (2.41).

The bare resonance frequency of the resonator f_r is reduced due to the coupling (expressed by Q_c) to the measured resonance frequency

$$f_0 = f_r \cdot \left(1 - \sqrt{\frac{2}{Q_c \pi}} \right). \quad (2.44)$$

With the relation between frequency and wavelength given in Eq. (2.14) and the fact that the resonator length $l = \lambda_0/4$, the bare resonance frequency can be written as

$$f_r = \frac{c}{\lambda_0 \sqrt{\epsilon_{\text{eff}}}} = \frac{c}{4l \sqrt{\epsilon_{\text{eff}}}} = \frac{1}{4l \sqrt{LC}}, \quad (2.45)$$

where λ_0 denotes the wavelength at resonance and the low-loss approximation given in Eq. (2.16) is used for the last step. Remembering from section 2.3.2 that the inductance in a superconducting CTL is the sum of the magnetic inductance L_m and the temperature dependent kinetic inductance L_k , the resonance frequency becomes

$$f_r(T) = \frac{1}{4l \sqrt{L_m C} \sqrt{1 + L_k(T)/L_m}}. \quad (2.46)$$

Since everything else is set by the CTL geometry, this formula for the bare resonance frequency can be used to extract the kinetic inductance. The temperature dependence of L_k as described by Eqs. (2.33) and (2.35) contains the parameter λ_0 , the London penetration depth at $T = 0$. In other words, a fit of L_k with Eq. (2.33) results in a value for λ_0 .

In conclusion, TL resonators are, apart from multiple other applications, a handy tool to measure the loss α of a CTL. But where are these losses originating from?

2.4.3. Loss Mechanisms

Loss sources for superconducting CTLs in different temperature and power regimes and for several materials are well described in the literature. Here is a short summary of the findings.

As already assumed in the lumped element circuit model for TLs (see Sec. 2.1), there are conductor losses leading to a finite R and dielectric losses, for which G is used. Dielectric loss stems from microwave absorption of nearby two-level states (TLSs) located at defects in the dielectric substrate and at the metal-air and metal-substrate interfaces [24]. The choice of an appropriate substrate is important to minimise these losses. Sapphire [23] and high resistivity silicon [18, 24] are shown to be good candidates. Silicon dioxide and silicon nitride introduce more losses [24, 25], but for some fabrication processes, a thin layer of them is helpful. Another possibility to decrease dielectric losses is to minimise the number of coupled TLSs at the interface. It is shown that an extensive substrate cleaning before the metal deposition

reduces the number of TLSs and an extremely deep anisotropic substrate etching in the gap between the centre conductor and the ground plane moves the interface away from the high electric field region what in turn reduces the coupling to interfacial TLSs [26]. With increasing temperature or power, all TLSs get saturated and they cannot absorb energy any more. Hence, dielectric losses are most relevant at low temperatures.

High quality resonators are fabricated from various superconductors like aluminium [18, 24] and materials with a higher T_c like niobium [25], niobium titanium nitride [26] and molybdenum rhenium [23]. But loss and superconductors, this seems like a contradiction at first sight. The point is that at finite temperatures, apart from superconducting electrons, there are also thermally excited quasiparticles. The coexistence of superconducting and normal electrons is captured in the so-called two-fluid model [16]. A DC current lower than the critical current can flow without resistance because the normal and superconducting electrons provide two channels in parallel and obviously, the zero-impedance superconducting channels carries all the current. The situation changes when an ac current is applied since it acts on all charge carriers, in particular also on the normal electrons, which experience ohmic losses. According to the BCS theory, the number of quasiparticles in a superconductor with an energy gap Δ is proportional to $e^{-\Delta/k_B T}$. Since conductor losses are proportional to the number of quasiparticles, they increase exponentially with temperature, as well.

2.4.4. Measurements at 4.2 K

After the introductory sections from before, some resonator data are discussed. The resonator shown in Fig. 2.7 (c) is put inside a copper box for characterisation in liquid helium at 4.2 K with the dipstick setup (see section 5.5). A picture of the box containing the sample chip is in Fig. 2.8 (a). The two SMA connectors on the outside are connected to both ends of the feedline and the box is closed with a metallic cover for the measurements. The transmission coefficient is detected with a vector network analyser (VNA). The fundamental mode of the coupled $\lambda/4$ -resonator is plotted in Fig. 2.8 (b). By applying Eqs. (2.37) and (2.43), one can extract the internal and the coupling quality factor, as indicated in the figure. Details on the fitting procedure are given at the end of appendix A.4.

The power applied to the TL is -34 dBm, which corresponds to $0.4 \mu\text{W}$. The simple dipstick setup used does not contain amplifiers (see section 5.5). Therefore, a rather high power is needed to achieve a clear signal. But since there is no power dependence of the resonance observed from -24 dBm down to -64 dBm (not shown here), we conclude that the obtained results are reliable and no high-power effects obscure the results.

This measurement serves as a confirmation that the quality of the sputtered niobium is alright and that our fabrication process is suitable for high quality resonators. The same kind of resonator experiments will appear again in section 4.1.2. There, the compatibility of RF circuit fabrication with carbon nanotube growth and the influence of a silicon nitride layer is examined.

One has to say that the quality factors of resonators, which are even fabricated together and are on the same feedline, scatter quite a lot. Quality factors as high as 8000 were measured on several resonators, but other resonators showed only half of it without any optically observable defect in the CTL. In conclusion, we see that with our way of fabrication, it is not possible to achieve consistent quality factors. Nevertheless, we learn the range which we can expect, which is already helpful for further planning.

Looking at the temperature dependence of the resonance leads to further insights. Fig. 2.8 (c)

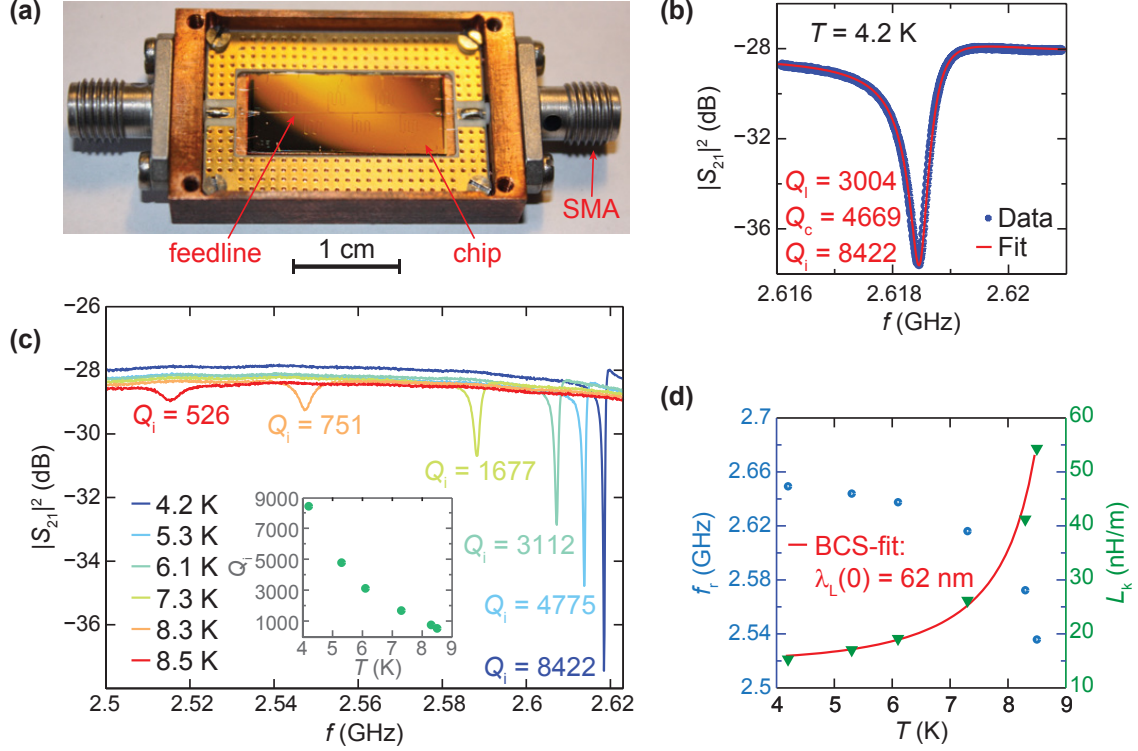


Figure 2.8.: **(a)** Picture of the copper box with a resonator chip inside for dipstick measurements. The horizontal feedline on the chip is slightly visible. **(b)** Transmission spectrum for one of the resonators together with a fit. **(c)** Temperature dependence of the spectrum and the internal quality factor (inset). **(d)** Extracted bare resonance frequency f_r and kinetic inductance L_k with a fit to the BCS-prediction. The power applied to the feedline is -34 dBm for all measurements.

shows the resonance evolution at higher temperatures. As expected, the resonance frequency is decreasing with increasing temperature because of the rising kinetic inductance (see section 2.3.2) and the quality factor is dropping due to enhanced quasiparticle loss (see section 2.4.3).

With the help of Eq. (2.44), the measured resonance frequency can be transformed to the bare resonance frequency f_r . The resulting frequencies are plotted in fig. 2.8 (d). The CTL has a conductor with $s = 12 \mu\text{m}$ and a gap size $w = 6.5 \mu\text{m}$ and consists of a niobium layer on 170 nm silicon dioxide with $\epsilon_r = 3.9$ and silicon beneath with $\epsilon_r = 11.9$. For this bilayer substrate, Eq. (2.28) can be applied and leads to a capacitance of 175 pF/m and a magnetic inductance $L_m = 411$ nH/m. Knowing this, one can extract from the resonance frequency the kinetic inductance according to Eq. (2.46), with the results plotted in the figure. However, we will see in the next paragraph that the London penetration depth of niobium is short and the condition $t < 2\lambda_L$ is not fulfilled for the lowest temperatures, which might add some deviation.

The critical current of our niobium films was previously determined to be 9.25 K. A fit of the kinetic inductance to the temperature dependence given by the BCS theory [Eq. (2.35)] gives a London penetration depth at $T = 0$ of $\lambda_L(0) = 62$ nm, which is quite close to the 43 nm stated in literature for similar niobium film thicknesses [27]. One can conclude from the figure

that at milli-Kelvin temperature, where we want to conduct our later experiments, the kinetic inductance of our niobium films is tiny compared to the magnetic inductance and hence its influence can be neglected when planning the geometry of CTLs and resonators operating at these temperatures.

2.5. Miscellaneous

2.5.1. Transmission Line versus Waveguide

In the literature, transmission lines (TLs) and waveguides are not always strictly and consistently separated. The distinction between the two terms used in this thesis is motivated and explained in the following paragraph.

TLs and waveguides are both structures to carry electromagnetic waves. But due to their geometry, they support different kinds of modes. TLs on the one hand consist of at least two conductors, which are separated by an insulator. Their operating mode is quasi-TEM and they transmit signals from DC up to high frequencies. The most important kind of TLs for this work is a coplanar transmission line. More details on this type are found in section 2.3. Another prominent example is coaxial cables.

On the other hand, waveguides are either made out of one conductor usually in the form of a metallic pipe or out of dielectrics with different dielectric constants, like for instance optical fibres. The transmission in waveguides happens due to reflections at the metallic boundaries or at the dielectric interfaces. The standing wave condition inside the waveguide sets a lower bound to the supported signal frequency depending on the waveguide's lateral dimension. The electromagnetic field pattern in waveguides is either transverse electric (TE) or transverse magnetic (TM), but not TEM.

2.5.2. Why 50 Ω ?

The common characteristic impedance of coaxial cables is 50 Ω . Thus, to be impedance matched and avoid signal reflections, that is also the standard input and output impedance of most components and instruments. A plausible explanation for this convention goes as follows. The attenuation constant α for an air-filled ($\epsilon_r = 1$) coaxial cable has a minimum at 77 Ω . The maximum power handling is limited by voltage breakdown above an electric field of $3 \cdot 10^6$ V/m for room temperature air at sea level pressure. For air-filled coaxial cables, maximal power handling is achieved for a characteristic impedance around 30 Ω . Hence, 50 Ω represents a compromise between both requirements of minimal loss and maximal power handling [10].

3 Impedance Matching

This chapter deals with the electronic engineering task of impedance matching. In particular, it focuses on a microwave impedance-matching circuit based on coplanar transmission lines (CTLs), called stub impedance-matching circuit or short stub tuner. While the general properties of CTLs are the topic of the previous chapter, this chapter contains a detailed description of the CTL-based stub tuner and some proof-of-principle measurements of this circuit. Details on the circuit fabrication and more measurements are found in subsequent chapters. At the end of the chapter, an alternative way of impedance matching with an LC circuit is presented and compared to stub impedance matching.

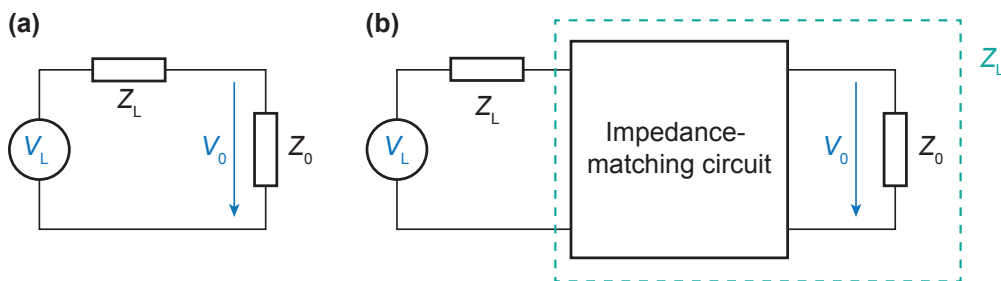


Figure 3.1.: (a) Schematic for simple noise detection without impedance matching. The noise voltage V_L generated at the load impedance Z_L is measured over an impedance Z_0 . (b) An impedance-matching circuit transforms the detection impedance Z_0 to the load impedance Z_L .

But what is our motivation for impedance matching? The aim of this thesis is to detect noise generated by high-resistance devices. Noise emitted by a device of impedance Z_L can be modelled as a voltage source in series. The problem with noise detection of high-resistance samples gets apparent in Fig. 3.1 (a). A high-impedance device of typical impedances $Z_L \sim 0.1 - 1 \text{ M}\Omega$ emits the voltage noise V_L . When measuring the voltage noise with an instrument of input impedance $Z_0 = 50 \text{ }\Omega$, only the tiny fraction Z_0/Z_L of the emitted voltage V_L is measured. This fraction can be increased by adding an impedance-matching circuit between the load and the instrument, as shown in Fig. 3.1 (b). At full matching, the circuit transforms the impedance seen by the load from Z_0 to Z_L .

In principle, it is possible to achieve matching between any complex load impedance and Z_0 for a certain frequency. Impedance matching is a standard task in electronic engineering and there are different types of impedance-matching circuits readily found in textbooks [10]. However, the physical implementation of each method has a limited range of applications for which it works reliably.

One possibility is to use a network consisting of an inductor and a capacitor. While lumped-element LC networks are easy to assemble and well suited up to a few hundreds of megahertz,

parasitic effects get more pronounced at higher frequencies. For example the equivalent circuit of a real inductor consists of the ideal inductance in parallel with an inter-winding capacitance. Whereas at low frequencies this capacitance represents a high-impedance path with low influence, at higher frequencies it starts to become important. Nevertheless, we have recently started to work on a microwave implementation of an LC matching network because it provides a large bandwidth of high transmission. More on this is found in section 3.2.

However, for the operation at GHz frequencies, it seems more natural to use a distributed element approach to achieve well reproducible results. Such a circuit is the so-called quarter-wave transformer; a section of CTL with intermediate characteristic impedance $Z_0^* = \sqrt{Z_0 Z_L}$ and a length of one quarter of the wavelength at resonance. In order to match a device with an impedance in the order of 10 k Ω , a characteristic impedance Z_0^* of a few k Ω is needed, which is difficult to obtain (see section 2.3.1). For this purpose, a CTL containing a series SQUID array at the centre conductor has been developed to boost the CTL inductance [28]. An advantage is that by changing the magnetic field through the SQUID loops, one can change the inductance and thus has a tunable matching circuit for free.

A possibility for a matching circuit made out of low characteristic impedance CTLs is the stub tuner; the main matching circuit utilised in this thesis. As presented in this and the next chapter, stub tuners are easily fabricable and computable. In earlier experiments, stub tuners were fabricated on a PCB, to which the nearby mesoscopic device was bonded [29]. Later on, stub impedance matching has been integrated on-chip [30].

3.1. Stub Impedance-Matching Circuit

An image of a stub tuner made with niobium on silicon together with a schematic are found in Fig. 3.2. Looking from the left low-impedance side, the stub tuner consists of two parallel CTL segments with characteristic impedance Z_0 . One CTL segment of length D_2 has an open end, whereas the other one of length D_1 is terminated by the load impedance Z_L . Both lengths are close to $\lambda_0/4$, with λ_0 being the wavelength at resonance.

The working principle of a stub tuner can be understood by considering it as an interferometer. In a simplified picture, an incident wave at the low-impedance input is split at the T-junction. The wave reaching the open end is completely reflected, while the amplitude and phase of the reflection at the other end depends on Z_L (see section 2.2). In the matched situation, the lengths D_1 and D_2 are such that for a specific frequency and load impedance the reflected waves add destructively at the T-junction, meaning that nothing is coming back from the stub tuner. But now let us turn to a more rigorous description of the circuit.

3.1.1. Matching with a Lossless Stub Tuner

First, the simple case of a stub tuner with lossless CTLs is treated since it has analytical solutions [10] and it provides an illustrative picture of the basic properties. A schematic of the stub circuit is shown in Fig. 3.2 (b).

Stub tuning makes use of the fact that the impedance on a terminated CTL depends on the distance from the load, as expressed by Eq. (2.22). The admittance at the T-junction looking along the terminated CTL is denoted by Y_{D1} . If the load impedance is separated according to $Z_L = R + i \cdot X$, the admittance stemming from the terminated CTL reads

$$Y_{D1} = \frac{1}{Z_{D1}} = \frac{1}{Z_0} \cdot \frac{Z_0 + i \cdot (R + i \cdot X)t_1}{(R + i \cdot X) + i \cdot Z_0 t_1}, \quad (3.1)$$

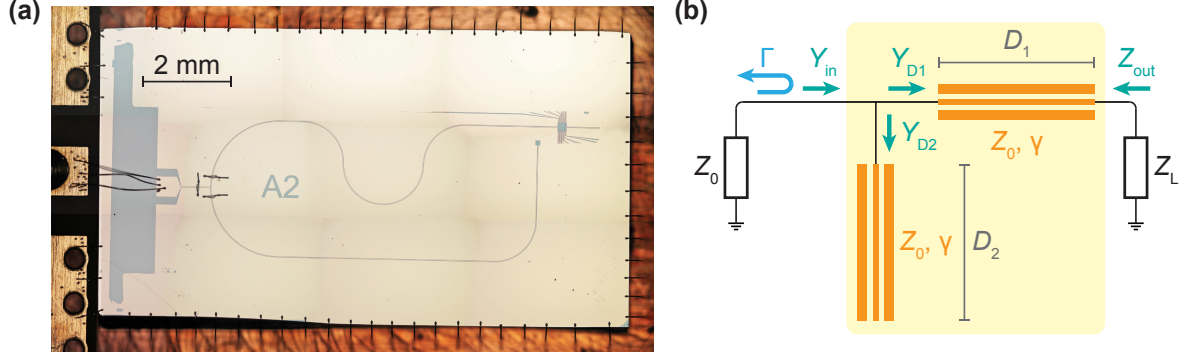


Figure 3.2.: **(a)** Image of an open stub tuner with 150 nm-thick niobium (light area) on a Si/SiO₂ substrate (grey). The stub tuner input is on the left side. The launcher is connected with bond wires (black). At the T-junction, where the two CTLs split, there are three bond wires (black) serving as airbridges between the ground planes. The device area is on the top-right CTL end. Bond wires around the sample edge establish a good connection of the ground plane to the setup ground. The pattern is defined with photolithography followed by plasma etching. **(b)** Schematic of a stub tuner (on a yellow background) consisting of two CTLs in parallel (orange).

with the abbreviation $t_1 = \tan(\beta_0 D_1)$ and β_0 being the wavenumber at the matched frequency f_0 . Separating the expression for $Y_{D1} = G_1 + i \cdot B_1$ into its real and imaginary components leads to

$$\begin{aligned} G_1 &= \frac{R(1 - t_1^2)}{R^2 + (X + Z_0 t_1)^2} \\ B_1 &= \frac{R^2 t_1 - (Z_0 - X t_1)(X + Z_0 t_1)}{Z_0 [R^2 + (X + Z_0 t_1)^2]}. \end{aligned} \quad (3.2)$$

In contrast, the admittance of the open-ended CTL at the T-junction is purely imaginary and reads [see Eq. (2.23)]

$$Y_{D2} = i \cdot B_2 = i \cdot \frac{1}{Z_0} \cdot \tan(\beta_0 D_2). \quad (3.3)$$

The input admittance seen from the low-impedance side in front of the T-junction is the sum $Y_{\text{in}} = Y_{D1} + Y_{D2}$ and is in general complex. Impedance matching requires that $Y_{\text{in}} = 1/Z_0$, which results in the two conditions for the real and imaginary parts

$$G_1 = \frac{1}{Z_0} \quad \text{and} \quad B_1 = -B_2. \quad (3.4)$$

The first condition gives a quadratic equation for t_1 with the two solutions

$$t_1 = \tan(\beta_0 D_1) = \frac{X \pm \sqrt{R[(Z_0 - R)^2 + X^2]}/Z_0}{R - Z_0}, \quad \text{for } R \neq Z_0. \quad (3.5)$$

Solving for D_1 leads to the following two shortest lengths (in terms of λ_0 , the wavelength at resonance)

$$D_1 = \begin{cases} \frac{\lambda_0}{2\pi} \arctan(t_1), & \text{for } t \geq 0 \\ \frac{\lambda_0}{2\pi} [\arctan(t_1) + \pi], & \text{for } t < 0 \end{cases}. \quad (3.6)$$

Due to the periodicity of tangents, $D_1 + n \cdot \lambda/2$ are also (longer) solutions, where n is a non-negative integer. The corresponding imaginary components are found by inserting t_1 in B_1 of Eq. (3.2). The second condition that B_1 has to be cancelled by the open-ended CTL leads to the lengths [using Eq. (3.3)]

$$D_2 = -\frac{\lambda_0}{2\pi} \cdot \arctan(B_1 Z_0), \quad (3.7)$$

with periodicity $\lambda_0/2$, too. If one of the lengths turns out to be negative, $\lambda_0/2$ has to be added.

If we restrict ourselves to a real load impedance ($X = 0$) and to $R > Z_0$, we find the two principal solutions

$$D_1 = \frac{\lambda_0}{2\pi} \cdot \arctan\left(\sqrt{\frac{R}{Z_0}}\right) \quad \text{and} \quad D_2 = \frac{\lambda_0}{2} - \frac{\lambda_0}{2\pi} \cdot \arctan\left(\frac{R - Z_0}{\sqrt{RZ_0}}\right) \quad (3.8)$$

$$\text{or } D_1 = \frac{\lambda_0}{2} - \frac{\lambda_0}{2\pi} \cdot \arctan\left(\sqrt{\frac{R}{Z_0}}\right) \quad \text{and} \quad D_2 = \frac{\lambda_0}{2\pi} \cdot \arctan\left(\frac{R - Z_0}{\sqrt{RZ_0}}\right). \quad (3.9)$$

If there is some loss in the CTL, it is not possible any more to find analytical solutions for the stub tuner lengths. One can use numerical methods to find the minimum of Γ , as for example with the `NMinimize` function of Mathematica. Although being quantitatively not exact, the lossless results from above still capture the features of a stub tuner qualitatively as long as the losses are small and thus they are used for the following analysis.

Without loss of generality, we focus on the solution of Eq. (3.8). The lengths needed for matching at a resonance frequency $f_0 = 3$ GHz as a function of load resistance are plotted in Fig. 3.3 (a). D_1 is always shorter than D_2 . The order would be reversed with the other set of solutions. For large matched resistances R_{match} the *arctan*-terms are converging towards $\pi/2$ and both lengths are approaching $\lambda_0/4$. The flattening for large load resistances points out a fabrication limitation. Small deviations in the CTL lengths (also indirectly induced by changes of the effective dielectric constant ϵ_{eff} or Z_0) cause a larger shift of the matched resistance the larger the desired R_{match} . In other words, the stub tuner becomes more sensitive to fabrication-induced deviations the larger the matched resistance is.

3.1.2. Input Impedance of a Stub Tuner

By looking at the schematic of a stub tuner in Fig. 3.2 (b), it is obvious that the input admittance Y_{in} seen from the low-impedance side is the sum of the admittances of the two CTL arms. Adding these two contributions given in Eqs. (3.1) and (3.3) and taking the inverse leads to the stub tuner input impedance

$$\begin{aligned} Z_{\text{in}} &= \frac{1}{Y_{D1} + Y_{D2}} \\ &= Z_0 \cdot \frac{Z_0 + Z_L \cdot \tanh(\gamma D_1)}{Z_L [\tanh(\gamma D_1) + \tanh(\gamma D_2)] + Z_0 [1 + \tanh(\gamma D_1) \tanh(\gamma D_2)]}. \end{aligned} \quad (3.10)$$

This is the general expression including a finite CTL loss α . The absolute value of the input impedance over a large frequency range is plotted in Fig. 3.4 (a) for a load $R = 100$ k Ω . The stub tuner is matched at 3 GHz to this resistance $R_{\text{match}} = 100$ k Ω . In the zero-frequency limit, it approaches R as expected. The behaviour at higher frequencies is somewhat peculiar. Away from the matched frequency, the stub tuner looks like a short. Only close to matching, the

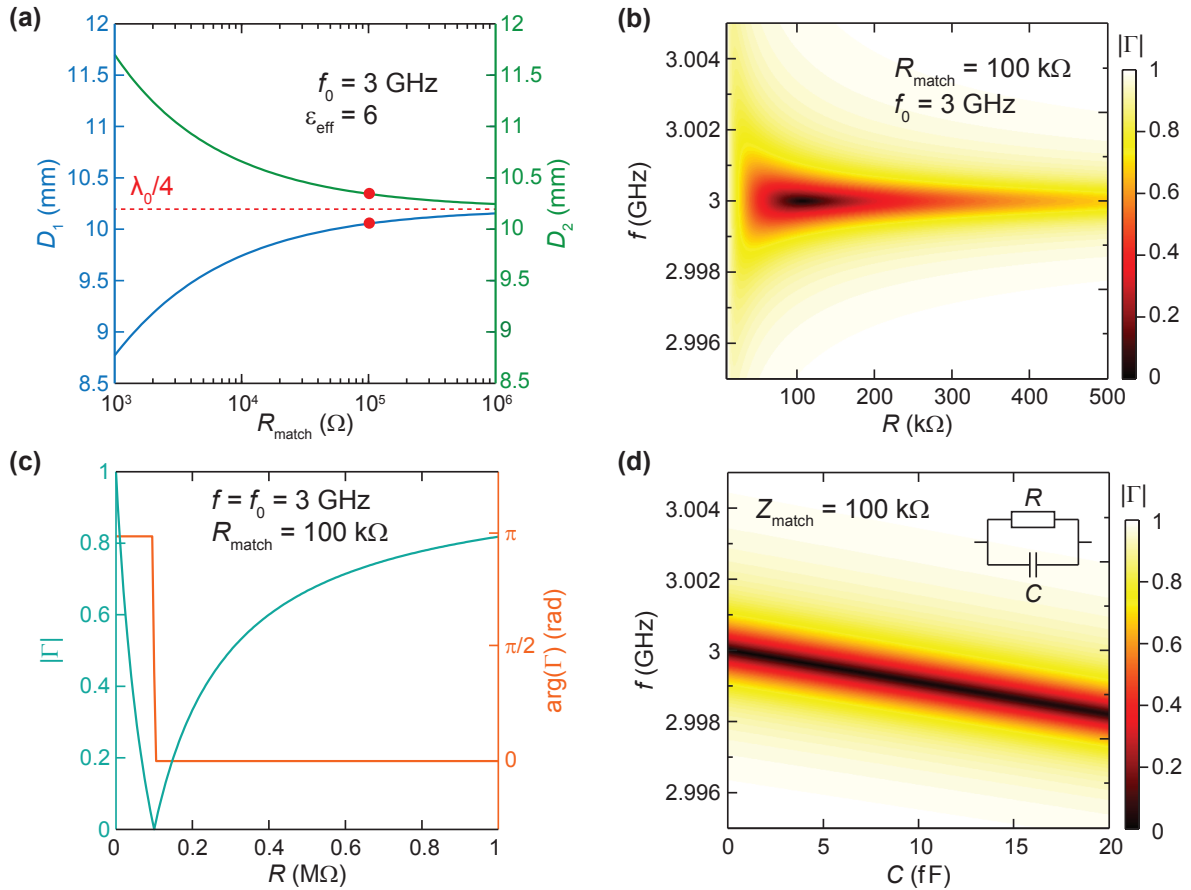


Figure 3.3.: (a) Stub tuner lengths needed to match at 3 GHz with a lossless stub tuner. Red dots indicate the solution at $R = 100$ k Ω , which are used for the remaining plots and for Fig. 3.5, too. (b) Reflectance amplitude dependence on frequency and load resistance. (c) Amplitude and phase of the reflectance as a function of load resistance at the resonance frequency, which corresponds to a horizontal cut of (b) at 3 GHz. (d) Reflectance amplitude when a capacitor C is added in parallel to the load resistor, while the real part is kept at 100 k Ω .

impedance rises to some finite value, as seen in Fig. 3.4 (b). As desired, the input impedance reaches 50 Ω at full matching (red curve). If R is higher than the matched resistance (blue curve), Z_{in} goes above 50 Ω at the resonance frequency and if R is smaller than the matched resistance (green curve), Z_{in} stays below 50 Ω .

3.1.3. Reflectance of a Lossless Stub Tuner

The purpose of reflection measurements on a stub tuner is twofold. First of all, it enables to obtain the stub tuner parameters α , D_1 and D_2 from fitting the reflection spectrum at a known load impedance Z_L (see section 3.1.5). Once the stub tuner parameters are known, the variable load impedance value can be deduced from the reflection amplitude (see section 6.3.2). In this way, reflectometry on a stub tuner is a fast and sensitive way to measure impedances

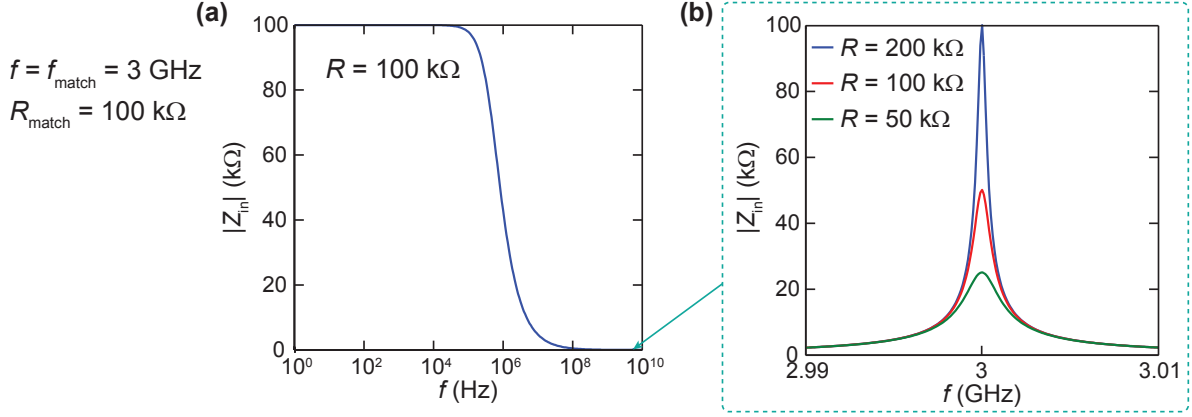


Figure 3.4.: Input impedance magnitude of a lossless stub tuner matched at 3 GHz to a load of 100 kΩ. (a) Plot over a large frequency range with the load being $R = R_{\text{match}} = 100$ kΩ. (b) Enlarged around the first resonance for three different load resistances.

at high frequencies [31].

The reflection coefficient at an impedance step from Z_0 to Z_{in} is defined in Eq. (2.20) to be $\Gamma = (Z_{\text{in}} - Z_0)/(Z_{\text{in}} + Z_0)$. For a lossless stub tuner, the input impedance of Eq. (3.10) becomes

$$Z_{\text{in}} = Z_0 \cdot \frac{Z_0 + i \cdot Z_L \cdot \tan(\beta D_1)}{i \cdot Z_L [\tan(\beta D_1) + \tan(\beta D_2)] + Z_0 [1 - \tan(\beta D_1) \tanh(\beta D_2)]}. \quad (3.11)$$

As seen in section 3.1.2, the stub tuner transforms the load impedance to Z_0 at full matching and thus the reflection coefficient Γ vanishes. The general load impedance Z_L can be divided into real and imaginary parts: $Z_L = R + i \cdot X$. In the beginning, we will consider a purely real $Z_L = R$. The reflectance amplitude given a matched load resistance $R = 100$ kΩ is plotted in Fig. 3.3 (b) as a function of frequency and load. If the load resistance R moves away from the matched value, the resonance dip is increasing, but the resonance frequency stays constant.

The influence of a load resistance modification on the reflection coefficient becomes more evident in Fig. 3.3 (c), which is a cut of Fig. 3.3 (b) at $f = f_0$. The phase is jumping by π when crossing the matched load and the reflection dip is increasing by moving away from the matched load. This shows the possibility to deduce the load resistance R from Γ when knowing the stub tuner parameters D_1 and D_2 .

The influence of an imaginary part X in the load Z_L is different. For example, a capacitance C parallel to the load resistor leads to the load impedance $1/Z_L = 1/R + i \cdot \omega C$. The corresponding reflectance spectrum is shown in Fig. 3.3 (d). Here, the real part is kept at the matched value of 100 kΩ while the capacitance is increased. In addition to the change of the resonance amplitude because one is moving away from matching, the resonance frequency is decreasing. This demonstrates the use of a stub tuner as a capacitance or inductance detector.

Now, we will turn back to a purely real load resistance. For a more quantitative discussion, Fig. 3.5 (a) shows the reflectance spectrum at different load resistances, which corresponds to vertical cuts in Fig. 3.3 (b). The plots reveal the resonant nature of a stub tuner. In the limit $R \gg Z_0$, the two CTL segments have both roughly the length $\lambda_0/4$. The sum of these two segments can be considered as being a $\lambda/2$ -resonator with one open end and one almost open end. In contrast to the usual $\lambda/2$ -resonators used in circuit QED [18], the coupling to the

resonator is not capacitive. Instead, the $50\ \Omega$ measurement line is directly connected at the voltage node in the centre of the stub tuner CTL. The direct connection of the RF line to the stub tuner allows to apply a DC voltage in addition to the RF excitation to the device via the same port.

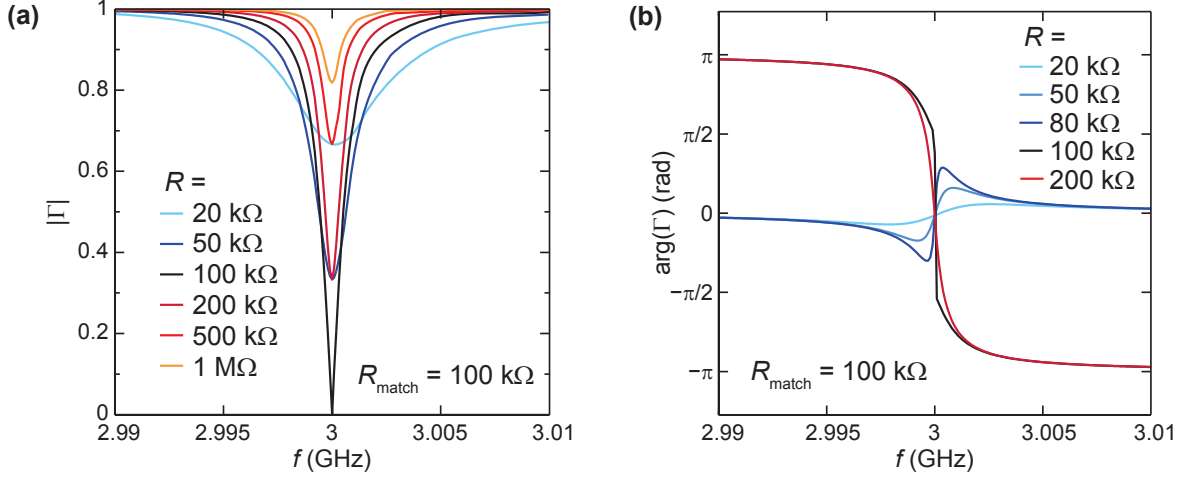


Figure 3.5.: Reflection spectrum of a lossless stub tuner for several load resistances, with the matched load being $100\ \text{k}\Omega$ at $3\ \text{GHz}$. (a) Amplitude and (b) phase.

When considering the stub tuner as a resonator, the load resistance R represents a resonator leak. This leak gives rise to a load quality factor (see section 2.4.2), which is in the limit $R \gg Z_0$

$$Q_L = \frac{\pi}{4} \cdot \frac{R}{Z_0}, \quad (3.12)$$

as derived in appendix B.1.2. On top of the resonance dip behaviour discussed earlier, one observes in Fig. 3.5 (a) a monotonic decrease of the bandwidth with rising resistance, which can be understood with the proportionality of the load quality factor to the resistance.

The phase dependence of Γ on the resistance is found in Fig. 3.5 (b). The slope at the resonance frequency has a different sign for resistances below and above matching. This phase jump when crossing the matched resistance is also seen in Fig. 3.3 (c).

3.1.4. Effect of Losses

A stub tuner consisting of a lossy CTL can be described as a resonator with a second, internal leak in addition to the load leak. This leak gives rise to an additional quality factor, Q_i . The same argument as for $\lambda/4$ -resonators given in appendix A.1 leads again to the expression for an internal quality factor

$$Q_i = \frac{\beta}{2\alpha}. \quad (3.13)$$

According to Eq. (2.39), the total quality factor is a combination of the load and internal quality factors: $Q = Q_L Q_i / (Q_L + Q_i)$. In order to be sensitive to the load resistance, the internal quality factor must be larger than the external one. In this case, the total quality factor is dominated by the load quality factor, and consequently the resonance is sensitive to changes of the load.

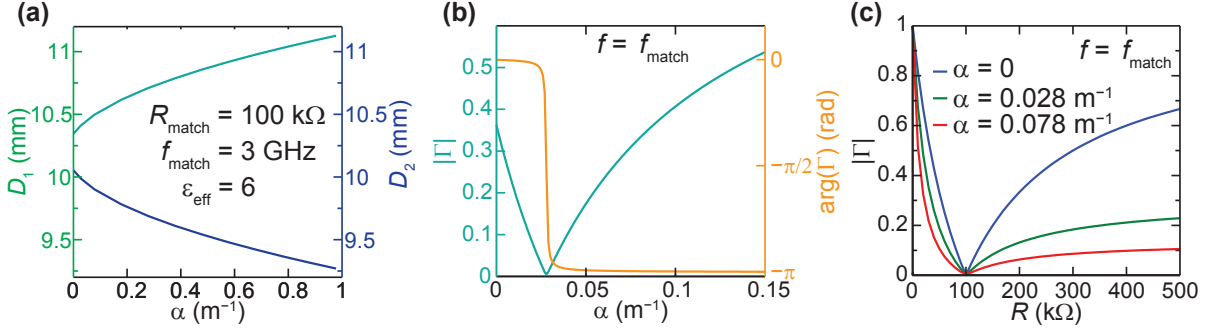


Figure 3.6.: In all three figure, the stub tuner is fully matched for $R_{\text{match}} = 100 \text{ k}\Omega$ and $f_0 = 3 \text{ GHz}$. **(a)** CTL lengths D_1 and D_2 needed to achieve full matching as a function of α . **(b)** Reflection amplitude and phase dependence on α at the resonance frequency. The circuit is matched when $\alpha = 0.028 \text{ m}^{-1}$. **(c)** Reflection amplitude dependence on the load resistance at the resonance frequency when being matched for three different losses α .

In case of a lossy stub tuner, there is no analytical formula to find the required CTL lengths D_1 and D_2 for matching, as it exists in the lossless case [see Eqs. (3.8) and (3.9)]. Instead, the reflection coefficient amplitude

$$|\Gamma| = |(Z_{\text{in}} - Z_0)/(Z_{\text{in}} + Z_0)|. \quad (3.14)$$

can be minimised numerically. Here, Z_{in} is the stub tuner input impedance from Eq. (3.10). The resulting CTL lengths needed to match a load of $100 \text{ k}\Omega$ at 3 GHz as a function of damping α are plotted in Fig. 3.6 (a). The higher the loss, the larger is the difference between D_1 and D_2 .

Fig. 3.6 (b) shows the reflection amplitude and phase dependence on α when being matched to one specific value of α . The important message is that there are two possible values of α for one given reflectance amplitude. Consequently, fitting to the magnitude of a resonance spectrum as for instance done in Fig. 3.7 (b) can converge to two different values of α . To find the correct damping, one can either take into account the phase of Γ or compare the bandwidth of the measured spectrum with $f_0/Q_{\text{int}} = f_0 \cdot 2\alpha/\beta$ [see Eq. (3.13)]. Those two bandwidths are only equal for one α .

Fig. 3.6 (a) confirms that full matching with a lossy stub tuner is still possible. A larger difference between the CTL lengths compensates for a finite α . But as expected, loss reduces the sensitivity of the stub tuner resonance on the load resistance. In Fig. 3.6 (c), the reflection amplitude at the matched frequency is plotted as a function of load resistance. When the loss is increasing, the curves get flatter or in other words the resonance dip is less sensitive to resistance changes.

3.1.5. Reflection Measurements of an Open Stub Tuner

We will discuss now the first experiments we carried out with stub tuners. The bare stub tuner shown in Fig. 3.2 (a) was cooled down to 4.2 K and later even to milli-Kelvin temperatures for reflection measurements. The area at the end of the upper CTL, where we eventually intend to connect the high resistance device, is left open in this sample. These measurements

serve as a test of the circuit fabrication and of the fitting routine used to extract the stub tuner parameters from the reflection spectrum. Furthermore, since these were one of the first measurements performed on the newly build cryogenic RF setup, they also served as a check of the setup. While this section is devoted to the measurements results, the stub tuner fabrication procedure is explained in section 4.2.2.

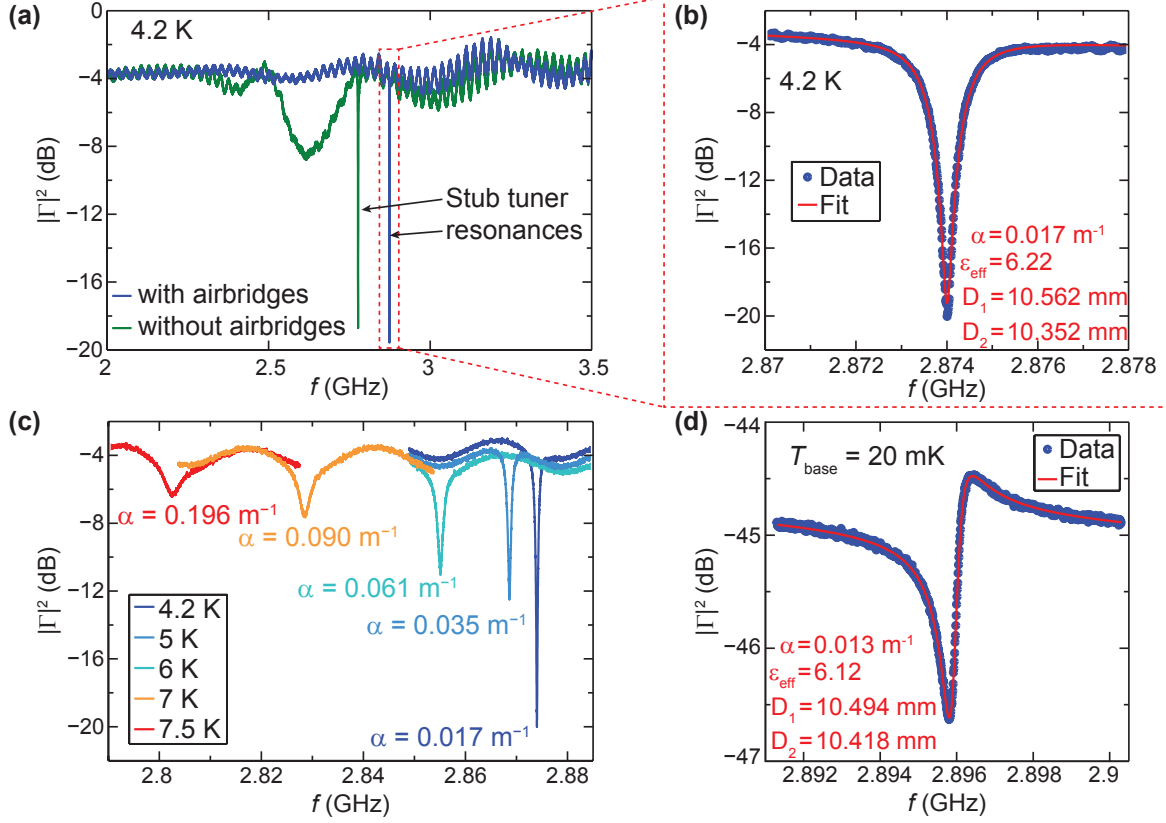


Figure 3.7.: Measurements of the open stub tuner shown in Fig. 3.2 (a). (a) Reflection coefficient with and without airbridges close to the T-junction at 4.2 K probed with -24 dBm. (b) Close-up view in the range of the red dashed area in (a). Dots are measured points of the stub tuner resonance probed with -34 dBm. The fitted curve is plotted in red and the corresponding parameters are written in the figure. (c) Resonance at higher temperatures. The fitted values of α are indicated. (d) The same stub tuner in the dilution refrigerator with a base temperature of 20 mK measured with an excitation power of -102 dBm.

Considering first the green reflectance curve of Fig. 3.7 (a) measured at 4.2 K, one sees apart from the narrow stub tuner resonance a broad resonance. The difference to the blue curve, where the broad resonance is absent, is that there are no airbridges yet close to the T-junction. Such airbridges, connecting the different ground planes close to the junction where the CTL splits, can be seen as black lines in Fig. 3.2 (a). These airbridges prove to be crucial to suppress spurious resonances evolving from potential variations between the different parts of the ground plane. For the same reason, it is important to nicely connect the ground plane all along the sample edges with bond wires to the sample holder ground. Still, the bond wires

around the chip turn out to be not enough, as they were already there when the green curve was measured.

This measurement is conducted in the RF dipstick (see section 5.5). In the large range scan of Fig. 3.7 (a), wiggles on top of the background reflection appear. From their period, a wavelength in the range of meters is estimated. Therefore, they are attributed to standing waves in the coaxial cables going to the instrument. These resonances could be damped with attenuators interrupting the coaxial cable.

A close-up view on the reflection amplitude is given in Fig. 3.7 (b). It can be accurately fitted to Eq. (3.14) with reasonable parameters. The fitting parameters α , ϵ_{eff} , D_1 and D_2 can be found in the figure. Details on the fitting method can be found in appendix B.1.1. The requirement that $Q_i > Q_L$ to be sensitive to the load (see section 3.1.4) allows to judge the usability of this stub tuner with a loss of $\alpha = 0.017 \text{ m}^{-1}$: The load quality factor is dominating as long as the load resistance is smaller than $\sim 300 \text{ k}\Omega$.

In Fig. 3.7 (c), the temperature dependence of the stub tuner resonance is investigated. With higher temperatures, the increased loss broadens the resonances and the increased kinetic inductance lowers the resonance frequency. This behaviour is very similar to what is observed with $\lambda/4$ -resonators in section 2.4.4.

The reflection of the same open stub tuner probed in a dilution refrigerator with a base temperature of 20 mK can be seen in Fig. 3.7 (d). The loss α is almost as high as at 4.2 K. The most striking difference to the 4.2 K data is the lineshape, which is much more asymmetric. Reasons for the enhanced asymmetry can be spurious modes in the setup or an enhanced effect of spurious modes in the niobium ground plane due to lower temperatures [32]. Since several later measurements on other samples showed more symmetric resonances in this setup, the asymmetry is attributed to not ideal grounding of this sample. Probably, the asymmetry could be lowered by making the bond wires to the ground plane around the chip denser than the chosen spacing of about 0.5 mm.

The findings from the open stub tuner measurements are very similar to the ones from the $\lambda/4$ -resonator measurements in section 2.4.4. For CTL characterisations alone, $\lambda/4$ -resonators are preferable because of their less complex structure, which results in fewer fit parameters and a more straightforward and reliable analysis. In addition, $\lambda/4$ -resonators need less space, which makes it is easier to couple several of them to one feedline for obtaining statistics. However, the stub tuner circuit is the one we intend to use for noise studies and in this respect, the open stub tuner measurements presented here give us more confidence to go towards the final circuit with a nanoscaled device attached to the stub tuner.

3.1.6. Output Impedance of a Stub Tuner

So far, the input impedance of a stub tuner seen from the low-impedance side and the resulting reflection properties were discussed. Intuitively, it is quite obvious that at matching, when there are no reflections for a signal entering the stub tuner, a signal generated at the device can leave the stub tuner without reflections, too. With the formulas given above, this argument can be confirmed. According to the schematic in Fig. 3.1 (b) that the output impedance seen by the load looking towards the stub tuner input is

$$Z_{\text{out}} = Z_0 \cdot \frac{Z_{\text{out,T}} + i \cdot Z_0 \tan(\beta D_1)}{Z_0 + i \cdot Z_{\text{out,T}} \tan(\beta D_1)}, \quad (3.15)$$

where $Z_{\text{out},T} = Z_0 Z_{D2} / (Z_0 + Z_{D2})$ is the output impedance at the T-junction. Using Eq. (3.3) and inserting the matching conditions given in Eqs. (3.5) and (3.7), a lengthy but simple calculation leads indeed to the result $Z_{\text{out}} = Z_L = R + i \cdot X$. In summary, the matching circuit transforms Z_L to an input impedance Z_0 and in turn, looking into the other direction, transforms Z_0 to an output impedance of Z_L .

This conclusion does not entirely hold any more when introducing loss in the CTL. Full impedance matching is always possible from both sides, because adjustments of the stub tuner lengths can account for the loss contributions [see Fig. 3.6 (a)]. But since the stub tuner is not a symmetric circuit, one ends up with a different set of stub tuner lengths depending on which side needs to be matched.

3.1.7. Transmission Coefficient of a Stub Tuner

Now, we turn to the transmission properties of a stub tuner. What is relevant for noise measurements is to know the transmission function from the high-resistance device side to the 50Ω instrument side. The goal of this section is to derive an expression for the transmission coefficient and to clarify its properties.

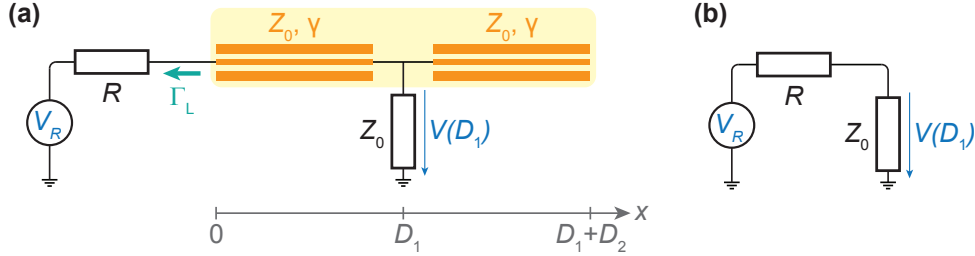


Figure 3.8.: (a) Sketch showing the stub tuner consisting of two CTL segments (orange) on a yellow background. It is connected to a load of resistance R and to the measurements line of impedance Z_0 . (b) Schematic for wideband detection in the absence of any impedance-matching circuit.

In Fig. 3.8, a schematic of a stub tuner is drawn. It is equivalent to the schematic of Fig. 3.2 (a) from before. We consider the case when a real load resistance R is attached. According to Eq. (2.8), the voltage in a CTL has the general waveform $V(x) = V^+ e^{-\gamma x} + V^- e^{\gamma x}$ resulting from the telegraph equations. The voltage coefficients of the left CTL segment, where $0 \leq x \leq D_1$, are called V_1^+ and V_1^- for the waves moving in positive and negative direction, respectively. It is derived in appendix B.2.1 how the boundary conditions at the two CTL ends and at the T-junction lead to the following expressions for the voltage coefficients:

$$\begin{aligned} V_1^- &= -V_R \cdot \frac{Z_0}{R + Z_0} \cdot \frac{1}{\Gamma_L + e^{2\gamma D_1} \cdot [1 + 2 \coth(\gamma D_2)]} \\ V_1^+ &= -V_1^- \cdot e^{2\gamma D_1} \cdot [1 + 2 \coth(\gamma D_2)], \end{aligned} \quad (3.16)$$

by using the definition $\Gamma_L = (R - Z_0) / (R + Z_0)$, which is the reflection coefficient directly at the load before the stub tuner.

We assume a noise voltage V_R to be emitted by the device with resistance R . What is detected at the stub tuner input side is the voltage $V(D_1)$ dropping over a resistance of Z_0 .

Using the coefficients from Eq. (3.16) leads to the voltage transmission function of a stub tuner

$$\begin{aligned}
 t_V(f) &= \frac{V(D_1)}{V_R} \\
 &= \frac{V^+ e^{-\gamma D_1} + V^- e^{\gamma D_1}}{V_R} \\
 &= \frac{2Z_0}{R + Z_0} \cdot \frac{e^{\gamma D_1} \cdot \coth(\gamma D_2)}{\Gamma_L + e^{2\gamma D_1} \cdot [1 + 2 \coth(\gamma D_2)]}.
 \end{aligned} \tag{3.17}$$

All relevant stub tuner parameters can be deduced from reflection measurements, as demonstrated in the previous section 3.1.5. The frequency dependence is implicitly given by the frequency dependent wavenumber β appearing in the propagation constant $\gamma = \alpha + i \cdot \beta$ [see Eq. (2.7)].

Under some conditions, the transmission function can be simplified, as derived in appendix B.2.2. If the stub tuner is fully matched to a resistance R at f_0 , $R \gg Z_0$ and furthermore the frequency is close to resonance ($\Delta f \ll f_0$, where $\Delta f = f - f_0$), the voltage transmission function is well approximated by

$$t_V(\Delta f) \approx \frac{2Z_0}{R} \cdot \frac{\frac{\pi}{2} \cdot \frac{\Delta f}{f_0} \mp \sqrt{\frac{Z_0}{R}}}{\pm 4 \frac{Z_0}{R} + i \cdot 2\pi \frac{\Delta f}{f_0}}. \tag{3.18}$$

The upper (lower) signs are valid for the set of solutions in Eq. (3.9) [Eq. (3.8)], where $D_1 > D_2$ ($D_1 < D_2$), respectively. See the end of appendix B.2.2 for more details on this.

In both cases, the amplitude squared has approximately the form of a Lorentzian:

$$|t_V(\Delta f)|^2 \approx \frac{Z_0}{4R} \cdot \frac{1}{1 + \left(\frac{\pi}{2} \cdot \frac{R}{Z_0} \cdot \frac{\Delta f}{f_0}\right)^2}. \tag{3.19}$$

The transmission peak value at $\Delta f = 0$ is $|t_V|^2 = 1/4 \cdot Z_0/R$. For comparison, the schematic in the absence of an impedance-matching circuit is drawn in Fig. 3.8 (b). In this case, the voltage transmission squared would be $t_V^2 \approx (Z_0/R)^2$ when $R \gg Z_0$ due to voltage division. In contrast, the $1/R$ -dependence of the stub tuner peak value implies a significantly higher transmission within a small frequency window when dealing with high load resistances R . The FWHM of the transmission function in Eq. (3.19) is found to be $\Delta f_{\text{FWHM}} = f_0 \cdot 4/\pi \cdot Z_0/R$, which is the same result as in Eq. (3.12) obtained for the reflection coefficient.

Some example spectra of the stub tuner transmission amplitude, assuming lossless CTLs, are shown in Fig. 3.9 (a). These curves are calculated using Eq. (3.17). The load resistance is fixed to the matched value for each curve. Full matching happens at $f = 3$ GHz. The required CTL lengths for this matching conditions are obtained via Eq. (3.8). In agreement with Eq. (3.19), the peak values and the bandwidth are both proportional to $1/R$. It gets apparent that the stub tuner behaves like a band-pass filter.

The peak values at the matched frequency of 3 GHz as a function of load resistances are plotted in Fig. 3.9 (b). The red curve represents an upper bound of the transmission achievable with any impedance-matching circuit since the matching is perfect at each point. In contrast, the blue curve shows the peak transmission with the stub tuner lengths fixed to get full matching at 100 k Ω .

Fig. 3.9 (c) focuses on the bandwidth of the transmission resonance. Again, the bandwidth when being matched to each resistance is plotted in red and the bandwidth when being matched

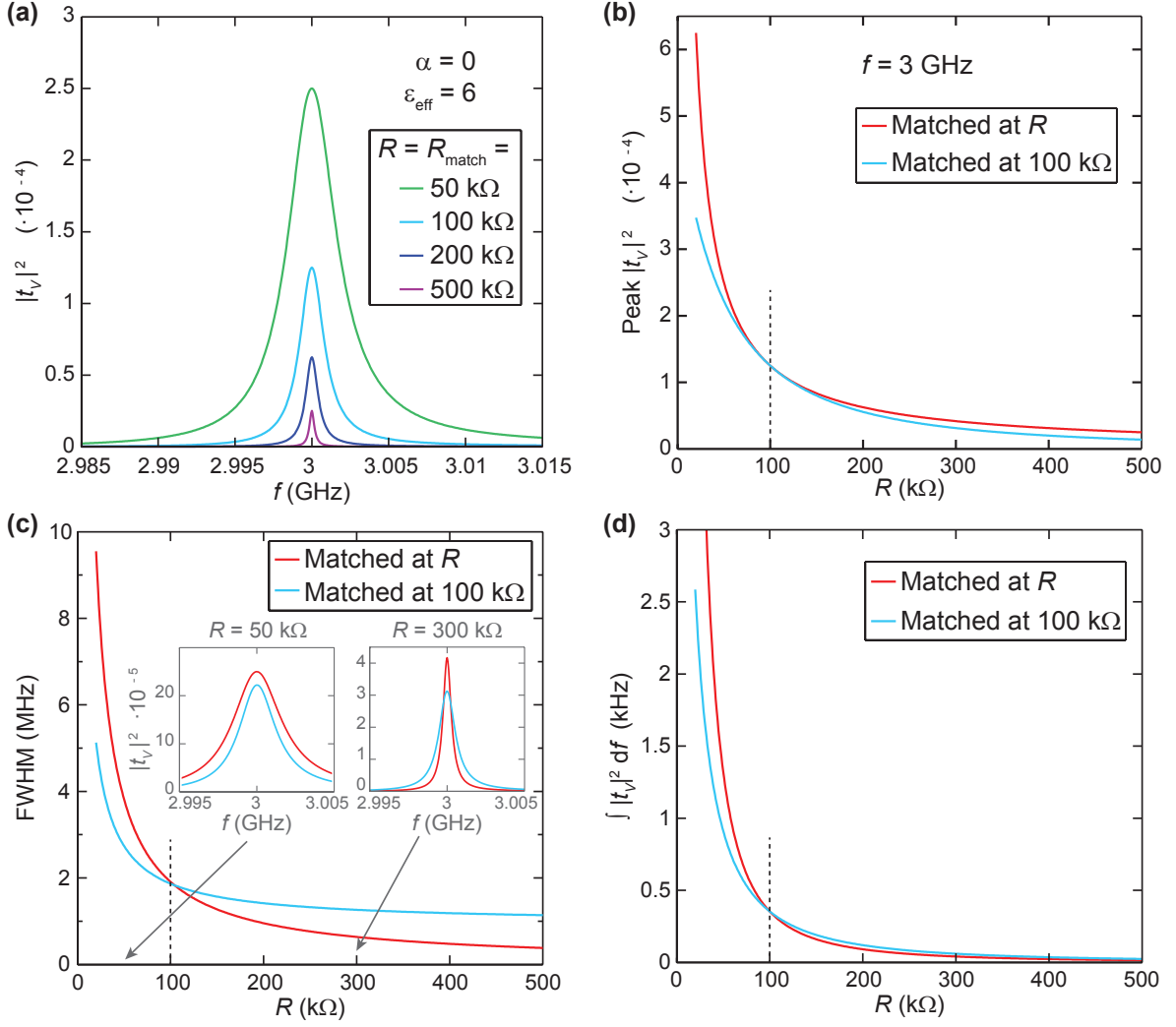


Figure 3.9.: Voltage transmission amplitude $|t_V|^2$ of a lossless stub tuner. **(a)** Frequency dependence when being matched at 3 GHz to four different load resistances. **(b)** Peak value at the matched frequency as a function of load resistance R . While the red curve shows the optimum achieved by matching to each resistance R , the stub tuner parameters are fixed for the blue curve to have full matching at 100 k Ω . **(c)** Full width at half maximum (FWHM) again matched to each load resistance (red) and matched to 100 k Ω (blue). The insets show two spectra for resistances below and above 100 k Ω . **(d)** Transmission amplitudes integrated over frequency.

only at 100 k Ω is plotted in blue. Surprisingly, there is a crossover at 100 k Ω . For lower resistances, the bandwidth for perfect matching is larger. However, the order changes above 100 k Ω and the bandwidth is even larger in the not perfectly matched case. The situation becomes more evident by looking at the two sample spectra shown in the insets. The peak transmission at f_0 is lower for both resistances when not being matched (blue curves). But while the bandwidth of the non-matched blue curve is smaller for resistances below matching (left inset), the bandwidth for resistances above matching (right inset) is in fact larger when

being not matched (blue curve) than when being matched (red curve).

In our experiments, we are going to detect the transmitted signal integrated over a frequency range. The integrated transmission coefficients over all frequencies from zero to infinity are shown in Fig. 3.9(d). Below the matched resistance of $100\text{ k}\Omega$, the integrated signal shown in blue is smaller than the optimal value achieved when always being matched. But above $100\text{ k}\Omega$, the effects of lower peak values and larger bandwidths seen in the right inset of Fig. 3.9(c) compensate each other and it is possible to gain as much signal without full matching as with perfect matching. However, being matched is still favourable in terms of signal to noise. In order to reach the same integrated signal, the required integration bandwidth is larger without matching than with perfect matching, but a larger integration bandwidth implies picking up more background noise, as well. If the signal integrated over a small frequency range around f_0 was plotted, the matched circuit would always deliver a larger signal than the non-matched one. This is further explained in the next paragraph.

3.1.8. Figure of Merit for Noise Measurements

In this last section about stub tuners, we are going to quantify the benefit of a stub tuner for noise measurements. To this end, the situations with and without impedance matching are compared. In the later case, the signal is strongly reduced due to impedance mismatch, but it offers significantly more bandwidth. However, in reality, the bandwidth (BW) is not infinite but always limited by circuit components like circulators and amplifiers. In our setup, the component with the smallest bandwidth of about 500 MHz is the circulator (see appendix D).

Schematics for the two cases of narrowband detection with a stub tuner and of wideband detection without impedance matching are in Fig. 3.8(a) and 3.8(b), respectively. In any case, the voltage drop over Z_0 caused by a voltage generated at the resistance side, V_R , can be expressed with the help of the transmission function as $V(D_1)^2 = V_R^2 \cdot \int_{\text{BW}} |t_V|^2 df$. Then, the signal power detected over Z_0 and integrated in a bandwidth BW is

$$P = \int_{\text{BW}} \frac{V(D_1)^2}{Z_0} df = \frac{V_R^2}{Z_0} \cdot \int_{\text{BW}} |t_V|^2 df. \quad (3.20)$$

In the absence of impedance matching, the transmission function is simply a constant given by voltage division:

$$t_V = \frac{Z_0}{Z_0 + R} \approx \frac{Z_0}{R}, \quad (3.21)$$

for $R \gg Z_0$. Hence, the detected power of Eq. (3.20) can be evaluated without impedance matching to be

$$P_0 = \text{BW} \cdot \frac{V_R^2 Z_0}{R^2}. \quad (3.22)$$

For a lossless stub tuner at full matching, the transmission function of Eq. (3.19) can be integrated analytically over the stub tuner bandwidth $f_0 \cdot 4/\pi \cdot Z_0/R$:

$$\int_{-\text{BW}/2}^{\text{BW}/2} |t_V|^2 df = \frac{f_0}{4} \cdot \left(\frac{Z_0}{R}\right)^2, \quad (3.23)$$

where f_0 is the resonance frequency. This leads to the ideal detected signal power for a lossless stub tuner at full matching

$$P_{\text{stub}} = \frac{f_0}{4} \cdot \frac{V_R^2 Z_0}{R^2}. \quad (3.24)$$

In comparison with P_0 of Eq. (3.22), the stub tuner provides an improvement in detected power as soon as $f_0/4 > \text{BW}$.

One may argue that it is not worth making the setup more complex by adding a stub tuner in consideration of the small gain in signal. However, the real strength of a stub tuner is that it enables to measure with a much smaller bandwidth of only some MHz. To make this evident, one has also to consider the background noise which is added after the matching circuit. The main noise source in our setup is coming from the amplifier chain. Assuming a constant background noise power spectral density S_{bg} , the collected background noise depends linearly on the measurement bandwidth. In this respect, narrowband detection is very beneficial. This is captured by the signal to noise ratio (SNR), which is given in general by

$$\text{SNR} = \frac{P}{S_{\text{bg}}\text{BW}} = \frac{\int_{\text{BW}} |t_V|^2 df}{\text{BW}} \cdot \frac{V_R^2}{S_{\text{bg}}Z_0}, \quad (3.25)$$

when using Eq. (3.20) for the signal power. Without matching circuit, the signal power given in Eq. (3.22) leads to

$$\text{SNR}_0 = \frac{V_R^2 Z_0}{S_{\text{bg}} R^2}. \quad (3.26)$$

While the BW drops out in the case of no impedance matching, the SNR of a stub tuner depends on the chosen BW. Integrating the transmission function of a lossless stub tuner at matching, as done in Eq. (3.19), results in

$$\text{SNR}_{\text{stub}} = \frac{V_R^2 f_0}{\pi S_{\text{bg}} R \text{BW}} \cdot \arctan \left(\text{BW} \cdot \frac{\pi R}{4 f_0 Z_0} \right). \quad (3.27)$$

The BW dependence of the SNR is plotted in Fig. 3.10 (a). It is maximal at zero BW and decreases for higher BWs. On the other hand, the signal increases with larger BWs. This interplay is captured by the product $\text{SNR} \cdot P$, where P is the signal power of Eq. (3.20). For a lossless stub tuner at matching, this product becomes

$$\text{SNR}_{\text{stub}} \cdot P_{\text{stub}} = \frac{V_R^4 f_0^2 Z_0}{2\pi^2 S_{\text{bg}} R^3 \text{BW}} \cdot \arctan^2 \left(\text{BW} \cdot \frac{\pi R}{4 f_0 Z_0} \right). \quad (3.28)$$

It has a maximum slightly higher than the FWHM, as illustrated in Fig. 3.10 (b). Setting its derivative to zero leads to the optimal bandwidth

$$\text{BW}^{\text{opt}} = 1.39 \cdot \text{FWHM} = 1.39 \cdot f_0 \cdot \frac{4}{\pi} \cdot \frac{Z_0}{R}. \quad (3.29)$$

Thus the choice that $\text{BW} = \text{FWHM}$ which we made for the signal power in Eq. (3.24) and which we continue to use is close to the optimal value and moreover simplifies the calculations. With the signal power of Eq. (3.24), the SNR of a stub tuner matched to a resistance $R \gg Z_0$ is

$$\text{SNR}_{\text{stub}} = \frac{\pi}{16} \cdot \frac{V_R^2}{S_{\text{bg}} R}. \quad (3.30)$$

This is an upper bound in the absence of loss and at full matching. The transmission function of Eq. (3.17) can be integrated numerically to obtain the SNR_{stub} under realistic conditions.

In order to compare the efficiency of a matching circuit for different matching conditions and even different impedance-matching circuits, we introduce the figure of merit $g_{\text{SNR}} =$

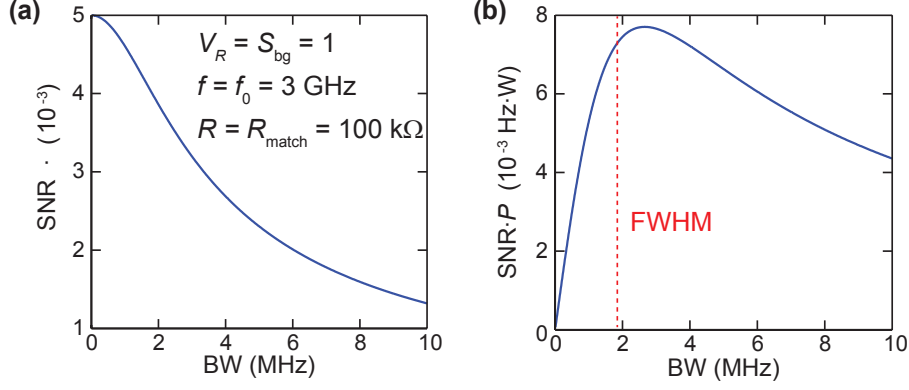


Figure 3.10.: (a) The SNR for measurements with a lossless stub tuner at full matching is decreasing monotonically with the bandwidth (BW). The SNR_0 without stub tuner of Eq. (3.26) would be five orders of magnitude lower. (b) The product SNR times signal power P has a maximum slightly above the FWHM, which is indicated by the red dashed line.

$\text{SNR}_{\text{matching}}/\text{SNR}_0$. With the help of Eqs. (3.25) and (3.26), the general expression for the figure of merit is found to be

$$g_{\text{SNR}} = \frac{\text{SNR}}{\text{SNR}_0} = \left(\frac{R}{Z_0} \right)^2 \cdot \frac{\int_{\text{BW}} |t_V|^2 df}{\text{BW}}, \quad (3.31)$$

and Eq. (3.30) gives an optimal figure of merit of a lossless stub tuner at perfect matching:

$$g_{\text{SNR}} = \frac{\pi}{16} \cdot \frac{R}{Z_0}. \quad (3.32)$$

As the load resistance R is in our case much larger than Z_0 , a stub tuner provides a tremendous increase in performance for noise measurements and other experiments for which a high signal transmission is crucial.

3.2. LC Matching Network

Another, more common lumped-element approach for impedance matching is a combination of an inductor and a capacitor. In this section, the properties of a simple LC matching circuit are introduced and compared with stub impedance matching. Later on, our concept for a microwave LC circuit is briefly mentioned.

3.2.1. Basic Properties

The circuit drawn in Fig. 3.11 is one possibility of an LC matching circuit (not including losses). At first, the matching conditions on L and C are derived. For that, we consider the input impedance seen from the low-impedance side, which is

$$Z_{\text{in}} = i\omega L + \frac{1}{1/R + i\omega C} = \frac{R + i\omega \cdot (L - CR^2 + \omega^2 LC^2 R^2)}{1 + \omega^2 C^2 R^2}. \quad (3.33)$$

The requirement for matching is that $Z_{\text{in}} = Z_0$. Equating the real and imaginary parts results in

$$C \approx \frac{1}{\omega_0 \sqrt{RZ_0}} \quad \text{and} \quad L \approx \frac{\sqrt{RZ_0}}{\omega_0}. \quad (3.34)$$

if $R \gg Z_0$ and with ω_0 being the angular frequency at matching. Equivalently, these relations can be written as

$$\omega_0 = \frac{1}{\sqrt{LC}} \quad \text{and} \quad \frac{L}{C} = RZ_0. \quad (3.35)$$

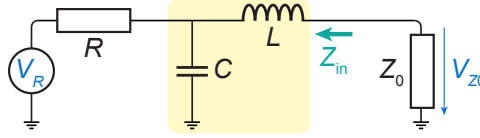


Figure 3.11.: Schematic of a simple lossless LC matching circuit.

The next step is to find a formula for the transmission function from the load to the low-impedance side. Kirchhoff's laws lead directly to the expression

$$t_V = \frac{V_{Z_0}}{V_R} = \frac{Z_0}{R} \cdot \frac{1}{1 + \frac{Z_0}{R} - \omega^2 LC + i\omega \cdot (CZ_0 + \frac{L}{R})}. \quad (3.36)$$

When the circuit is matched to the load R and frequency f_0 , the frequency can be written in terms of the matched frequency as $f = f_0 + \Delta f$ and the capacitance and inductance of Eq. (3.34) can be inserted. This leads to the transmission function

$$t_V = \frac{Z_0}{R} \cdot \frac{1}{1 + \frac{Z_0}{R} + i \cdot 2\sqrt{\frac{Z_0}{R}} \left(1 + \frac{\Delta f}{f_0}\right) - \left(1 + \frac{\Delta f}{f_0}\right)^2}, \quad (3.37)$$

which can be approximated when $R \gg Z_0$ to

$$t_V \approx -\frac{Z_0}{2R} \cdot \frac{1}{\frac{\Delta f}{f_0} - i \cdot \sqrt{\frac{Z_0}{R}}}. \quad (3.38)$$

In this limit, the amplitude squared of the transmission function takes on the Lorentzian lineshape

$$|t_V|^2 \approx \frac{1}{4} \cdot \left(\frac{Z_0}{R}\right)^2 \cdot \frac{1}{\frac{Z_0}{R} + \left(\frac{\Delta f}{f_0}\right)^2}. \quad (3.39)$$

From this, the FWHM can be directly inferred to be

$$\Delta f_{\text{FWHM}} = f_0 \cdot 2\sqrt{\frac{Z_0}{R}}. \quad (3.40)$$

The integral of the transmission in Eq. (3.39) can be evaluated to be

$$\int_{\text{BW}} |t_V|^2 df = f_0 \cdot \frac{\pi}{8} \cdot \left(\frac{Z_0}{R}\right)^{3/2}, \quad (3.41)$$

when the bandwidth is set to the FWHM. This leads to the signal power detected with a lossless LC circuit of [see Eq. (3.20)]

$$P_{LC} = \frac{\pi f_0 V_R^2}{8} \cdot \sqrt{\frac{Z_0}{R^3}}. \quad (3.42)$$

With the help of Eq. (3.25), the SNR becomes

$$\text{SNR}_{LC} = \frac{\pi}{16} \cdot \frac{V_R^2}{S_{\text{bg}} R}, \quad (3.43)$$

and finally the figure of merit for measurements with an LC circuit is obtained by Eq. (3.31):

$$g_{\text{SNR}} = \frac{\pi}{16} \cdot \frac{R}{Z_0}. \quad (3.44)$$

	FWHM	Signal power	SNR	g_{SNR}
Stub tuner	$f_0 \cdot \frac{4}{\pi} \cdot \frac{Z_0}{R}$	$\frac{f_0 V_R^2}{4} \cdot \sqrt{\frac{Z_0}{R}} \cdot \sqrt{\frac{Z_0}{R^3}}$	$\frac{\pi}{16} \cdot \frac{V_R^2}{S_{\text{bg}} R}$	$\frac{\pi}{16} \cdot \frac{R}{Z_0}$
LC circuit	$f_0 \cdot 2\sqrt{\frac{Z_0}{R}}$	$\frac{\pi f_0 V_R^2}{8} \cdot \sqrt{\frac{Z_0}{R^3}}$	$\frac{\pi}{16} \cdot \frac{V_R^2}{S_{\text{bg}} R}$	$\frac{\pi}{16} \cdot \frac{R}{Z_0}$

Table 3.1.: Summary of the key properties of stub tuner and LC matching circuits in the absence of loss, at full matching and when $R \gg Z_0$.

For comparison, table 3.1 summarises the key parameters of stub tuner and LC matching circuits. The bandwidth of the high transmission window of an LC circuit is larger than the one of a stub tuner by a factor $\pi/2 \cdot \sqrt{R/Z_0}$. Also the power of the detectable signal is enlarged by the same factor. This is not very surprising since the peak transmission coefficient at the matched frequency is fixed to $|t_V|^2 = 1/4 \cdot Z_0/R$ for any matching circuit and only the bandwidth varies from circuit to circuit. Consequently, the larger signal power of an LC circuit and the increased background noise due to the larger bandwidth compensate each other, leading to the same SNR and figure of merit g_{SNR} than for a stub tuner.

In conclusion, an LC matching circuit provides the same increase in SNR than a stub tuner. But the bandwidth for an LC circuit scales with $\sqrt{Z_0/R}$ instead of Z_0/R for a stub tuner, which results in a much higher bandwidth when the load resistance is large. This has advantages and disadvantages. If one wants to reduce the read-out time, an LC circuit is a better choice. The downside of a large bandwidth is that the unavoidable frequency dependence of the signal transmission through the setup complicates the calibration. Within the stub tuner bandwidth of some megahertz when being matched at 3 GHz to a high-resistance sample, the setup transmission is well approximated by a linear curve. But for larger bandwidths, a better knowledge of the frequency dependence is necessary.

At the end of the discussion on how to optimise the SNR, we want to note that it is equally important to minimise the background noise S_{bg} in the first place, as for instance with Josephson parametric amplifiers [20, 21]. Furthermore, the SNR is not the only limiting characteristic of an experiment. What counts experimentally is to reach a certain SNR which is high enough for the intended accuracy. Any further increase of the SNR does not reveal new features. But the larger the figure of merit, the smaller is the averaging time needed to reach the same SNR.

3.2.2. Towards a Microwave Realisation

The capacitance and inductance values needed for matching are obtained by Eq. (3.34). For example, to match a load of $100\text{ k}\Omega$ at 3 GHz , a capacitance as low as $C = 24\text{ pF}$ and an inductance as high as $L = 120\text{ nH}$ are needed. Parasitic capacitances and resistances of commercial lumped-element inductors with such a high inductance make it difficult to operate at gigahertz frequencies.

Our approach is to use superconducting spiral inductors [33, 34] as shown on the test sample in Fig. 3.12 (a). As a low-loss substrate, we use an undoped silicon substrate with a 170 nm -thick layer of silicon oxide. This substrate is compatible with our usual fabrication process for nanoscale devices. Therefore, it would be possible to place the high resistance device on the same chip between the inductor and the ground plane. In this way, the stray capacitance between the matching circuit and the device - which would lead to an RC -filtering effect - is minimised. The light grey area in Fig. 3.12 is 150 nm -thick sputtered niobium. The inductor pattern with 9 turns is written by PMMA-base electron-beam lithography and subsequent etching with an Ar/Cl plasma in an inductively coupled plasma (ICP) machine. The outer diameter of the inductor is $240\text{ }\mu\text{m}$, the line width is $2\text{ }\mu\text{m}$ and the spacing between the lines $2\text{ }\mu\text{m}$, as well.

In order to connect the planar coil centre to the outside, a bridge is needed. In the test resonator of Fig. (3.12), the bridge is directly connected to the ground plane. The idea for later samples is to place the high-resistance device between bridge and ground. A closer look on the bridge can be taken in Fig. 3.12 (b). The niobium bridge has a width of $3\text{ }\mu\text{m}$ and is supported by a crosslinked PMMA layer with a height of about 500 nm , which looks black in the picture. Crosslinking PMMA is achieved with an e-beam dose approximately 10 times higher than its clearing dose. The bridge fabrication including two additional lithography steps is actually more difficult than the fabrication of the planar inductor itself.

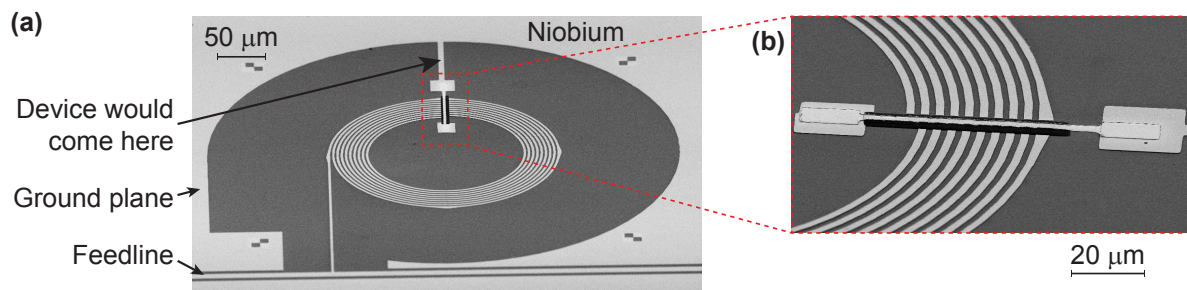


Figure 3.12.: (a) Picture of a spiral inductor with an inductance of about 80 nH . It is made with niobium on Si/SiO_2 . is connected to a feedline on the bottom and at the other side to ground via a bridge. The high-resistance device is going to be placed between bridge and ground. (b) Rotated close-up view on the niobium bridge, which is supported by crosslinked PMMA, which looks black in the picture.

The test sample in Fig. 3.12 (a) is an LC resonant circuit, with the capacitance arising from stray capacitances to the nearby ground plane and to the back plane. A resonance spectrum is gained by measuring the transmission of the attached feedline. By fitting to an appropriate model, values for L and C are obtained. A simple LC model applied to the first measurements on this kind of circuits reveal an inductance in the order of 80 nH for an inductor with 9 turns.

The work on LC matching circuits is successfully carried on by the PhD student Cezar Harabula. In the meantime, he did an extensive study on parasitic effects, worked on a more comprehensive and accurate model than the simple one presented here and achieved good matching to a carbon nanotube quantum dot.

3.3. Bode-Fano Criterion

In the context of the discussion about the resonant circuit bandwidth, the question arises whether there is any fundamental bandwidth limit. This small section is meant as a side remark, as it is not the intention of this thesis to push the bandwidth to the limit.

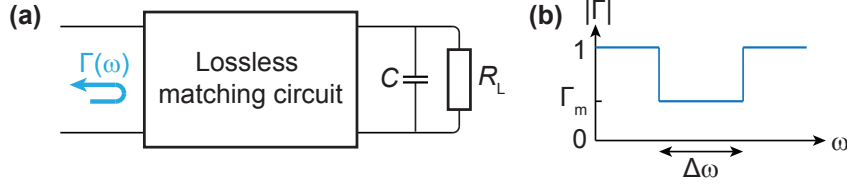


Figure 3.13.: (a) Matching network with a parallel RC load as an example for the Bode-Fano limit. (b) Example reflection coefficient with a transmission window of size $\Delta\omega$.

The Bode-Fano criterion [10] gives a theoretical limit of the bandwidth achievable with any (lossless) impedance-matching circuit. The criterion depends on the type of load impedance. In case the load consists of a resistance R and a capacitance C in parallel, as illustrated in Fig. 3.13 (a), the Bode-Fano criterion states that

$$\int_0^\infty \log\left(\frac{1}{|\Gamma(\omega)|}\right) d\omega \leq \frac{\pi}{RC}. \quad (3.45)$$

It sets a restriction to the frequency dependent reflection coefficient $\Gamma(\omega)$. More precisely, a small reflection coefficient (or good matching) is only possible in a limited frequency range. To clarify this, let us assume we wish to design a circuit with the reflection characteristic shown in Fig. 3.13 (b). Then, the Bode-Fano criterion leads to the restriction

$$\int_0^\infty \log\left(\frac{1}{|\Gamma(\omega)|}\right) d\omega = \int_{\Delta\omega} \log\left(\frac{1}{|\Gamma_m|}\right) d\omega = \Delta\omega \cdot \log\left(\frac{1}{|\Gamma_m|}\right) \leq \frac{\pi}{RC}. \quad (3.46)$$

It shows the trade-off between large bandwidth $\Delta\omega$ and small reflection minimum Γ_m . A perfect matching, meaning that $\Gamma_m=0$, is only possible for a discrete set of frequencies with $\Delta\omega = 0$.

4 Fabrication of Carbon Nanotube Samples

Quantum dots (QDs) formed in single-wall carbon nanotubes (CNTs) have been intensively investigated in our group for a long time. In particular when combining quantum dot physics and superconductivity, exciting results have been achieved. Hybrid device geometries consisting of CNTs with superconducting and normal leads have resulted in the observation of highly-efficient Cooper pair splitting [35], in studies of the interplay between the Kondo effect and superconductivity [36] or in detailed sub-gap spectroscopy revealing Andreev processes [37, 38], to name only a few. In these experiments, the average currents were measured using low-frequency lock-in techniques. Our aim is to extend the measurement scheme by a stub impedance-matching circuit, which allows to additionally measure the noise on top of the average current. These measurements can provide otherwise unattainable insight into transport processes. In spite of profiting from the CNT fabrication knowledge acquired over many years in the group, some adaptations were necessary to make it compatible with the on-chip microwave circuit fabrication.

For optimal RF results with a stub tuner attached to a CNT device, the following requirements should be fulfilled:

1. The microwave losses of the stub tuner must be kept as small as possible, such that its internal quality factor exceeds the load quality factor up to large device resistances (see section 3.1.4).
2. The distance between the stub tuner and the device must be as short as possible. The device resistance together with the stray capacitance of the line, which connects the device with the stub tuner, form an RC low-pass filter. In conclusion, a long distance between the device and the stub tuner causes a signal reduction.

During the PhD time, I have carried out several fabrication test runs and investigations to live up to these requirements. The resulting fabrication procedure is presented in this chapter. A table with a step-by-step description can be found in appendix C.

4.1. Carbon Nanotube Stamping

4.1.1. Carbon Nanotube Growth

CNTs are grown by chemical vapour deposition (CVD) at high temperatures. During the PhD thesis of Jürg Furrer, a dedicated CVD oven was built and a growth recipe was developed, which delivers a large amount of single-wall, high-quality CNTs [39, 40].

The basis for the growth are catalyst particles. We use a mixture of small iron, molybdenum and aluminium oxide particles, which are diluted in isopropanol. This dilution is sonicated with strong power to separate all particle clusters. Then, the catalyst dilution is spin coated on the substrate. If desired, CNTs can be grown locally by spin coating the catalyst on a resist

mask. A careful resist lift-off still keeps most of the catalyst particles on the unprotected area. Finally, the growth is done for 10 minutes at 950 °C in a hydrogen/methane atmosphere. While heating up and cooling down, the oven is flushed with a mixture of argon and hydrogen. The detailed growth recipe can be found in appendix C.

4.1.2. How to Get an On-Chip Stub Tuner

The best way to bring the CNT sample and the matching circuit close together is to place them on the same chip. Apart from minimising the RC -filtering effect as mentioned above, this makes the circuit performance more reproducible, as well. The RF properties of bond wires are not easy to model and to reproduce because they depend strongly on the wires' length, shape and their surrounding.

Combining a microwave circuit with CNTs is complicated by the fact that CNT growth is done at high temperatures. These growth temperatures destroy the superconducting properties of niobium. In contrast, niobium nitride is supposed to be robust against high temperatures. In fact, thermal annealing even causes a higher critical temperature due to less lattice distortions [41]. In order to test the RF quality of niobium nitride after CNT growth, we studied the resonance of $\lambda/4$ -resonators, as it is demonstrated in section 2.4.4. We observed that the quality factors drop below 100 at 4.2 K. In conclusion, fabricating a stub tuner and then growing CNTs on-chip is not an option.

Therefore, we have checked a reversed fabrication order. The idea was to grow CNTs first locally, protect this area with a resist layer and then sputter niobium. Niobium is lifted off in the CNT area and in the following, a stub tuner can be patterned on the niobium layer close to the CNTs. Finally, a CNT can be chosen and connected to the stub tuner in a last evaporation step.

As a test, we have fabricated $\lambda/4$ -resonators on substrate, which was in the CVD oven before. Again, these resonators showed a drastic quality factor reduction to values below 100 at 4.2 K. A possible reason might be amorphous carbon deposited during growth. To confirm this assumption, the substrate surface was cleaned with a long oxygen plasma between growth and niobium deposition. Indeed, the resonances got sharper and quality factors around 500 were measured at 4.2 K, which is on the other hand still considerably smaller than the quality factors of about 5000 obtained with pristine substrate. This indicates that the growth process is also harmful to the Si/SiO₂ substrate itself. Even though a SiO₂ reduction in hydrogen requires temperatures above 1000 °C [42], a reaction at lower temperatures might be possible at defect sites on the surface. When we etch 10 – 20 nm of the SiO₂ surface after growth with an Ar/Cl₂ plasma and then make resonators, the quality factors reach again values up to 3000. An increased surface roughness induced by the plasma etching might be the reason why the quality factors are not anymore as high as with pristine substrate. We observed a similar quality factor degradation with a silicon nitride substrate.

In summary, the results obtained with the order CNT growth and then stub tuner fabrication are not ideal either. This brought us to the idea to make CNT growth and the microwave circuit on two separate substrates and to transfer the CNTs later on.

4.1.3. Stamping Procedure

To overcome the problem of oxide degradation during CNT growth as discussed in the previous section, we have adapted a CNT stamping procedure developed in the group of Takis Kontos

[43]. Fig. 4.1 illustrates our CNT stamping process.

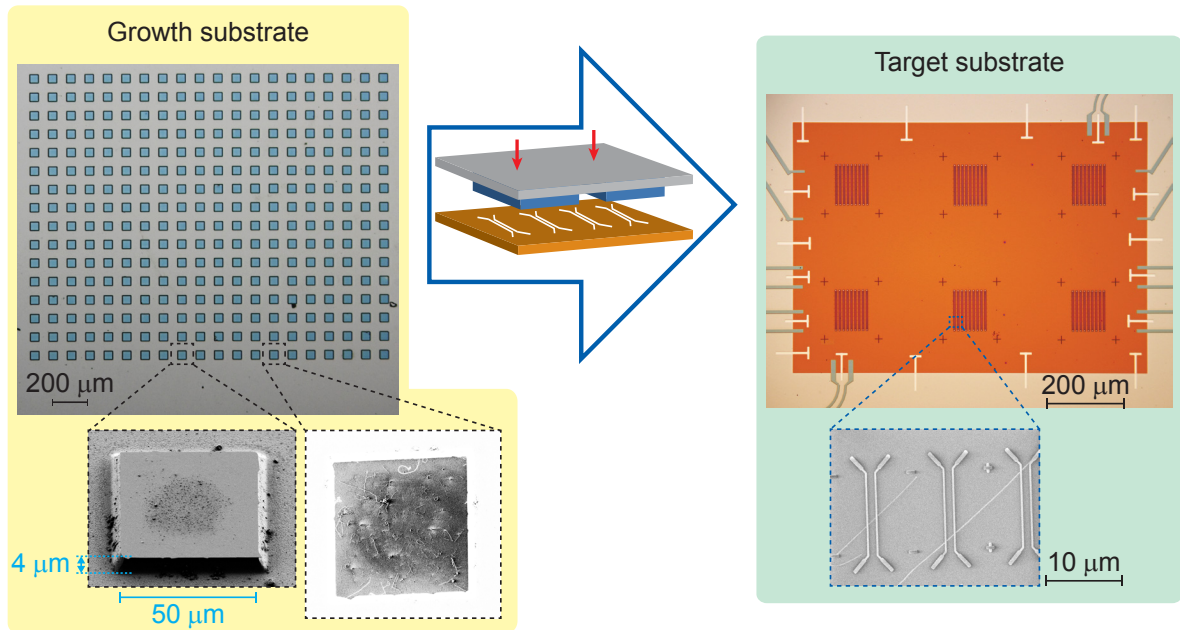


Figure 4.1.: Illustration of the CNT stamping process. CNTs are transferred by pressing the growth substrate and the target substrate together in a mask aligner. The growth silicon substrate is shown on the left half, containing an area of pillars. The left close-up view shows one pillar before CNT growth with dark catalyst particles in the centre. The pillar after growth containing CNTs on the surface is seen in the right close-up view. Images of the target substrate are shown on the right half. Bottom gates (dark lines), markers and T-shaped connecting lines to the surrounding microwave circuit are already prepared. The bottom picture shows an example of stamped CNTs on bottom gates. (Reprinted with permission from [44]. © 2015 by The American Physical Society.)

The growth substrate is silicon with a 170 nm-thick thermal oxide. We want to pattern a $2 \times 2 \text{ mm}^2$ -large area full of little squares with electron beam (e-beam) lithography. The resist has to stay on the exposed squares, which means we are looking for a negative resist. HSQ is a good candidate because it is very resistant to plasma etching. On the other hand, we also need wet HF etching for the stamp fabrication, which easily removes HSQ. Since PMMA withstands HF etching and is easy to remove in solvents, we use a bilayer of thick PMMA ($\sim 1 \mu\text{m}$) resist and a thin layer of HSQ on top. The HSQ development in TMAH after e-beam writing only removes the unexposed HSQ, while the PMMA remains everywhere. A three-step etching leads to the pillars, as described in the following. First, the PMMA not covered with HSQ is removed by an oxygen plasma. In the second step, SiO_2 is removed with HF wet-etching. HF also removes the HSQ layer and thus only a PMMA mask remains. The third step is to etch deeply into silicon with an SF_6 plasma and finally to remove the PMMA on the pillars in acetone. The result are square pillars as shown on the bottom left of Fig. 4.1 with a size of $50 \mu\text{m}$ and a height of $4 \mu\text{m}$.

What remains is to grow CNTs. As explained before in section 4.1.1, Fe/Mo catalyst particles

are spin coated and then the CVD process is done in the growth oven. When stamping, only a small amount of the CNTs plus some catalyst particles are transferred. Therefore, we wish to have a high CNT density on the growth substrate. This is why we use the original catalyst solution [39] without further dilution and we spin coat catalyst solution for 5 times.

In the meantime, the target substrate is prepared. As visible in Fig. 4.1 on the right side, the stamping area contains a grid of bottom gates and markers and connecting lines to the surrounding RF circuit (not visible). For the CNT stamping process, the growth substrate is glued with PMMA on a transparent glass plate and mounted in a mask aligner, which is normally used for UV lithography. The two substrates are aligned with the optical microscope to be on top of each other and pressed together. Since the growth substrate is not transparent, only a rough alignment is possible and the pillar area is larger than the bottom gate area to account for some misalignment. Alternatively, one could use a transparent quartz growth substrate, which would allow for a much preciser alignment with the cost of a more laborious pillar etching process. Once the growth substrate is glued on the glass plate, it is important to do the alignment and stamping quickly in order that the PMMA glue still remains soft and is able to balance any gap caused by not perfectly horizontal substrates. In my experience, one usually ends up with about 3 – 6 straight CNTs of usable length crossing some bottom gates if there are six bottom gate areas on the target substrate, as shown in the top right picture. This is enough for our purpose, since there is only space for 3 stub tuners around one stamping area.

The yield of transferred CNTs decreases rapidly if one uses the same stamp a second time. But the stamps can be reused in the following way. By wet etching with HF, approximately 10 nm of the SiO₂ pillar surface is removed. One gets back a clean pillar surface, which allows to spin coat catalyst again and grow CNTs for a next stamping.

A crucial point for successful stamping is that there are no dirt particles on the pillar surfaces, which would act as spacers during the stamping. For that, the stamp substrate needs to be cut to the final size and thoroughly cleaned before spin coating catalyst. The catalyst solution itself needs to be sonicated for a long time with high power to avoid big particle clusters, which would also separate the two substrates while stamping. The reason for doing many small pillars instead of one large one goes in the same direction. Like this, the contact area is reduced and with it the chance that a big particle on the surface reduces the stamping yield.

This way of stamping transfers many CNTs in a random manner. In contrast, there are also more elaborate ways to stamp single CNTs precisely on source and drain contacts of an otherwise fully prepared and already bonded sample at room temperature [31, 45] or even inside a cryostat [46].

4.2. Fabrication Steps

This section is devoted to the fabrication procedure. It contains descriptions of the different fabrication parts, which lead eventually to a CNT device connected to an on-chip stub tuner. Whereas the main text concentrates on more general considerations and highlights some crucial steps, all fabrication details are listed in appendix C.

4.2.1. Bottom Gates

As mentioned in section 2.4.3 about coplanar transmission line (CTL) loss sources, one cannot build a low-loss RF circuit on a doped substrate. Therefore, the often used gating with a global

doped-substrate backgate [47] is not an option and alternative local gates are needed to define and tune QDs in CNTs.

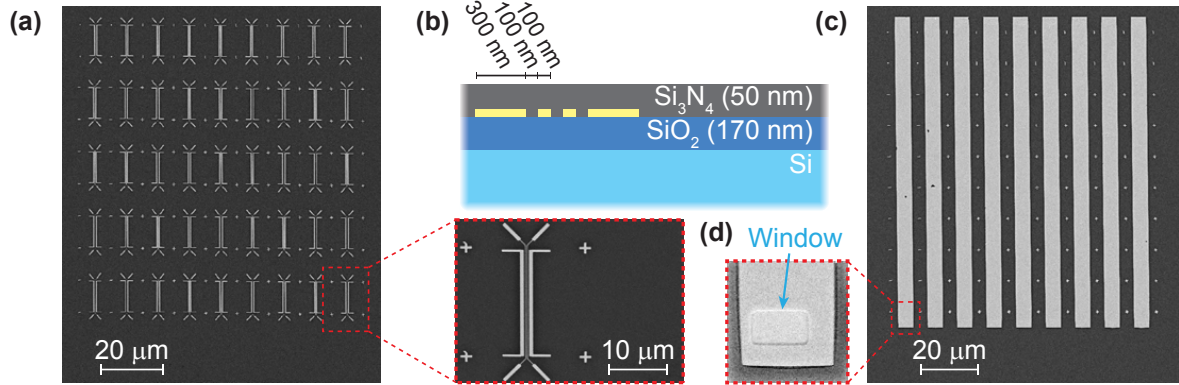


Figure 4.2.: Different kinds of bottom gates, which are covered by Si_3N_4 . (a) Area with narrow gates, allowing to form single and double QDs. The little crosses between the gates are markers. (b) Cross-section showing the gates in yellow (not to scale) (c) Long and wide gate stripes to form single QDs. (d) Si_3N_4 window etched to contact the gate later on.

Two examples of bottom gate structures are shown in Fig. 4.2. Multiple QDs can be formed by the version with several narrow gates illustrated in Figs. 4.2 (a) and (b). With the wide gates in Figs. 4.2 (c) and (d), a single QD can be defined.

In any case, a $100 \times 100 \mu\text{m}^2$ -large area is covered with bottom gates and markers to locate CNTs later on. One stamping area contains six of these gate areas close to each other, as shown in Fig. 4.1 on the right side. The gates are patterned with standard PMMA-based e-beam lithography and subsequently, 5 nm of titanium and 30 nm of gold are deposited in an e-beam evaporation system. The gates are isolated by a silicon nitride (Si_3N_4) layer on top with a thickness of 50 nm, which is deposited in a plasma-enhanced CVD (PECVD) process. This is done externally in the PSI. The temperature of about 300 °C in the PECVD chamber makes it impossible to use any resist mask and therefore the Si_3N_4 layer covers the entire substrate. We open windows at the ends of the gates in the next step to make the gates accessible, as shown in Fig. 4.2 (d). The windows are defined with e-beam lithography and etched with a CHF_3/O_2 plasma.

4.2.2. Stub Tuner

Having the covered bottom gates ready, the next step is to fabricate the stub tuner and in the same step bond pads for the gate lines and their connection to the stamping area. A picture of the resulting circuit with three stub tuners and ten bond pads for the DC gates located around the central stamping area is shown in Fig. 4.3 (a). For this, we cover the bottom-gate area with PMMA resist and deposit 100 – 150 nm of niobium in a magnetron sputtering machine. Lift-off removes the Nb layer on top of the bottom gate area. Then, the CTLs for the stub tuners are defined with e-beam lithography. The same structures could also be patterned with photolithography since our line widths are not smaller than 5 μm. While photolithography is faster and the available writefield is much larger, the structure can be easily modified with

e-beam lithography. This flexibility is an important advantage during the development of a new circuit and the writing time for one stub tuner of about 5 minutes is still reasonably fast for our purpose. The e-beam writefield limitation of our system to $2 \times 2 \text{ mm}^2$ is the reason for the meander-shaped CTLs shown in the figure.

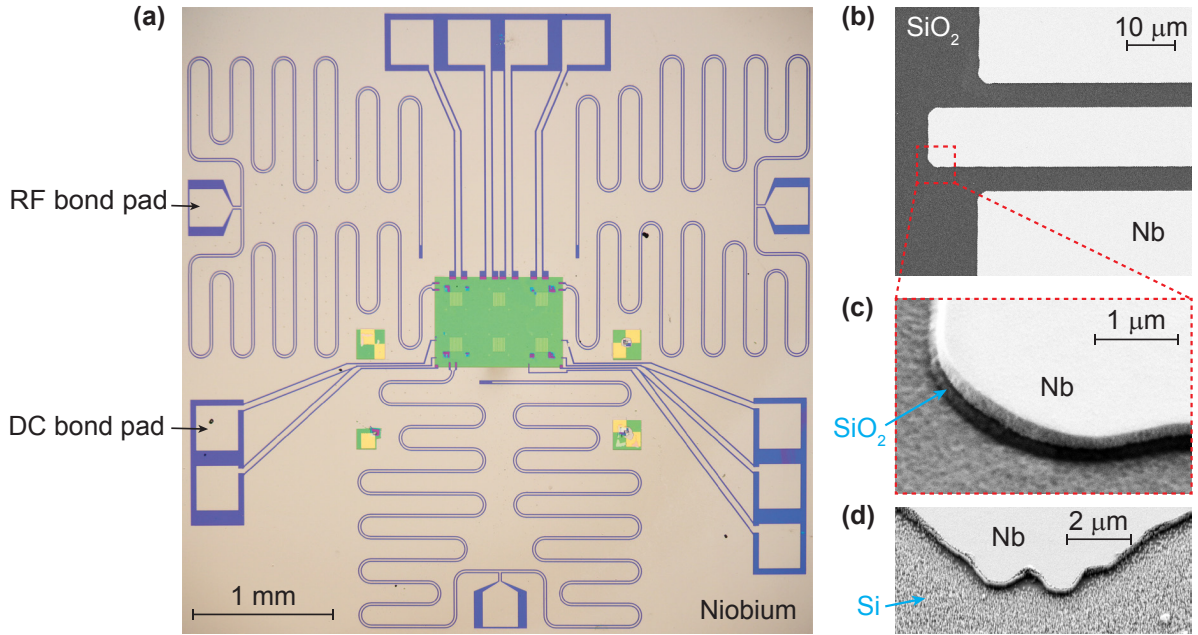


Figure 4.3.: **(a)** Image of the entire chip. The stamping area in the centre is surrounded by three stub tuners and ten DC gate lines. The blue area is SiO_2 and the green area Si_3N_4 . **(b)** Example of a CTL open end made with niobium on SiO_2 . **(c)** Side view on an edge of (b). The cross-section shows the 150 nm-thick niobium layer (light grey) and the SiO_2 below (dark grey). **(d)** Edge of another structure using the same plasma etching process as in (c) but on a silicon substrate without oxide on top. Many pillars appear on the etched surface due to the high etch rate of silicon.

Niobium etching is done in an inductively coupled plasma (ICP) machine. Anisotropic etching is achieved with an Ar/Cl_2 plasma. An example of an open-ended CTL fabricated with niobium on SiO_2 and a tilted close-up view on the edge are shown in Figs. 4.3 (b) and (d), respectively. The etch rates of Si_3N_4 and SiO_2 are not much lower than the one of niobium. It can be seen that the trenches are almost twice as deep as the niobium thickness. First of all, the over-etching ensures that all niobium is definitely gone and secondly, deep etching of the substrates moves possible two-level states (TLS) at the substrate away from the high-field region and can reduce dielectric losses of the CTL [26]. The deep etching of the trenches for the stub tuner removes the entire 50 nm-thick Si_3N_4 layer beneath and the SiO_2 substrate appears in blue in Fig. 4.3 (a). In the central bottom gate area, niobium is removed by lift-off and hence the Si_3N_4 layer is visible in green.

The etch rate of Si is 2-3 times larger than of niobium. As a consequence, it is problematic to have silicon directly beneath niobium. Niobium residue islands building at the instance when almost the entire niobium layer is etched, act like etch masks for the fast Si etching and lead

to pillar-like structures on the Si surface, as it is visible in Fig. 4.3 (d). Because of its smaller etch rate, SiO_2 beneath niobium leads to a much smoother surface [see Fig. 4.3 (c)]. The same is true for Si_3N_4 , which has a similar etch rate to that of SiO_2 .

We applied two different fabrication orders. The first one goes as follows. Bottom gates are fabricated, then the CNTs are stamped and already contacted and afterwards the niobium layer for the stub tuner is sputtered with some overlap between the CNT contact metal and the end of the stub tuner. Niobium on palladium or gold leads to reliable ohmic contacts.

Later on, we changed the order in the sense that the stub tuner is fabricated first and then the CNTs are stamped on the empty central area. The contact between the CNT and the stub tuner end is fabricated as a last step. Niobium oxidises quickly and therefore a short in-situ plasma etching of the oxide layer is needed before evaporating metal on top of niobium. Because the plasma etching would attack the CNT, it is not possible to make a direct connection between the stub tuner end to the CNT at once. Instead, we make short palladium contacts to the stub tuner end, the ground plane and the gate line even before CNT stamping. Such lines are visible in the top right image of Fig. 4.1 as T-shaped elements with light beige colour. This additional lithography step requires more work with the advantage that less lithography steps have to be done after the CNT is on the chip. This reduces the amount of resist residues on the CNTs, which can be harmful to their quality. Furthermore, when making superconducting lead contacts to CNTs (see section 4.2.5), it is crucial to do the lead evaporation as a last step owing to the low melting point of lead and indium.

4.2.3. Normal Metal Contacts to Carbon Nanotubes

After stamping, the CNTs are located and selected with a scanning electron microscope (SEM). To make the CNTs visible, or more precisely to observe their screening effect on the substrate, a low acceleration voltage of 1 kV and the in-lens detector are used [48].

Obviously, we are looking for CNTs crossing a bottom gate and with a reasonable length of at least a micrometre such that it can be contacted on both sides. Apart from that, there is no strict rule how to select the CNTs. Straight CNTs are preferred since curvature and angles are attributed to defects in the CNT lattice. Moreover, very bright and thick CNTs are possibly multi-wall and therefore ignored.

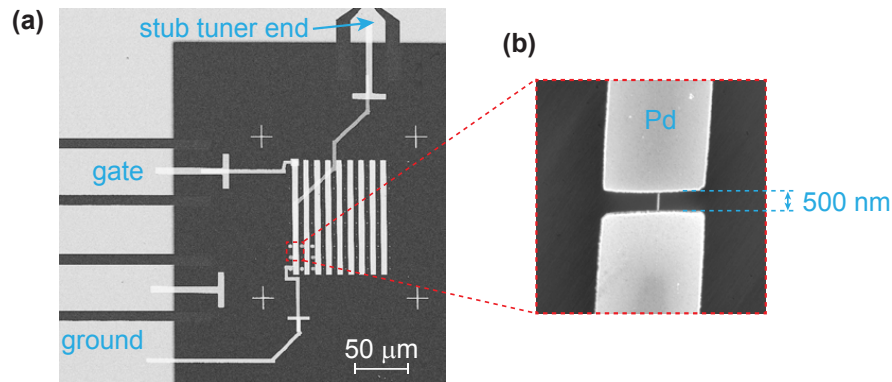


Figure 4.4.: (a) Picture showing the palladium source, drain and gate connections between the device and the surrounding niobium. (b) Palladium (Pd) source and drain contacts to a CNT.

Contacts to the selected CNTs are patterned by e-beam lithography. Instead of the standard PMMA resist, we switched to the resist ZEP for all lithography done after the CNT is on the chip. ZEP is shown to leave less resist residues than PMMA and hence resulting in a higher contact yield [49]. Certainly, clean CNT-metal interfaces are an important prerequisite for reliable metal-CNT contacts. Still, our contact resistances scatter within more than an order of magnitude even for samples on the same chip, which have all experienced the same fabrication conditions.

If a completely transparent contact to a CNT was achieved, the resulting resistance would be $h/4e^2 \approx 6.5 \text{ k}\Omega$ according to the four channels present in a CNT due to the two-fold spin and valley degeneracies. The observed resistances however are often much higher, indicating the formation of a barrier at the metal-CNT interface. On the one hand, these barriers lead to a charge confinement in the CNT for free. On the other hand, the lack of control and tunability of the barrier heights sets limits on experiments with such naturally formed QDs and is one of the main obstacles for the large scale integration of CNTs in mesoscopic devices. In spite of several theoretical and experimental studies on contact resistances, partly contradicting results were obtained and no general conclusion on the underlying mechanism could be drawn yet [50, 51].

The textbook argument for the electrical properties of a metal-semiconductor interface is given by the Schottky-Mott rule [52]. It is based on the different Fermi levels of the two materials. If they are brought into contact, the Fermi level difference is equilibrated by a charge flow across the interface, which in turn leads to the formation of a Schottky barrier. However, experimental data of bulk materials do often not agree with predictions from the Schottky-Mott rule. This is explained by the Fermi-level pinning due to interface states. For one-dimensional semiconductors on the contrary, such as CNTs, Fermi-level pinning is predicted to play a minor role [53]. Nevertheless, it is an experimental fact that metals with similar work functions yield different contacts to CNTs. Interestingly, first-principles studies of the interface properties on the microscopic level reveal the importance of the chemical bonding between metal and CNT [54–58]. According to their studies, the contact resistance depends strongly on the metal’s wetting properties and the hybridisation between metal and CNT.

In any case, it is established that both palladium [59] and titanium [56, 60] can provide highly transparent contacts to CNTs and these are therefore our two materials of choice to contact CNTs.

4.2.4. Superconducting Niobium Contacts to Carbon Nanotubes

In order to observe interesting Cooper pair-involved physics like Andreev processes [61–63], one superconducting contact to the CNT is needed. The type-II superconductor niobium with a relatively large gap (bulk value $\Delta = 1.45 \text{ meV}$ [64]) offers the potential to resolve subgap features up to high magnetic fields [38].

The recipe used here for niobium contacts to CNTs is developed by Jens Schindele [51] and Jörg Gramich [65]. The actual contact to the CNT is established via a 4.3 nm-thick titanium layer, which is sputtered with a very low power. We believe that a too high power might destroy the exposed CNT part. At least we measured very high contact resistances with higher sputtering power. The titanium thickness is a compromise between good CNT wetting and keeping the titanium layer well proximitised by the niobium above.

An example of a niobium-contacted CNT is shown in Fig. 4.5 (a). The white parts at the edges are sticking out flakes, which are sputtered on the resist walls. We intentionally use a

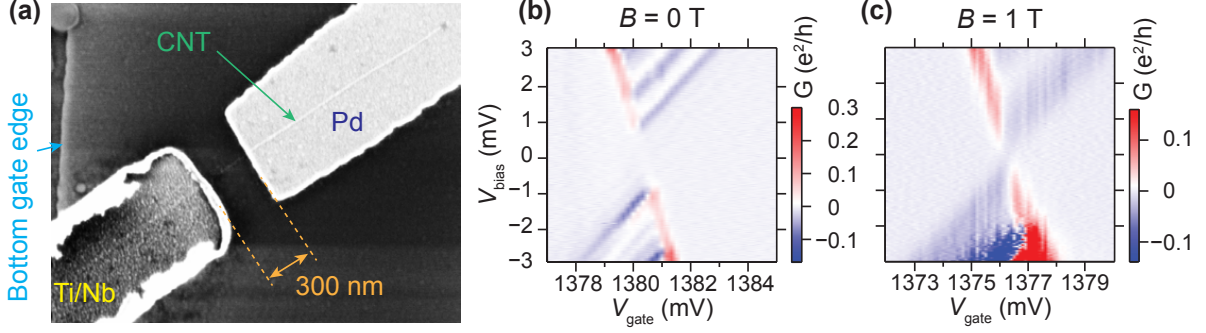


Figure 4.5.: (a) CNT on a silicon nitride substrate with a wide bottom gate beneath. It is contacted on one side with titanium/niobium (Ti/Nb) and on the other side with palladium (Pd). The titanium thickness is 4.2 nm and the niobium is 40 nm-thick. (b) and (c) Differential conductance in the single dot regime at a base temperature of 20 mK. (b) When the magnetic field $B = 0$ T, the conduction suppression for bias voltages $eV_{\text{bias}} < \Delta$ is apparent (with Δ being the superconducting energy gap). (c) The superconducting gap is completely suppressed at $B = 1$ T and the conduction triangles touch.

vertical resist profile. The reason is that sputtering happens quite isotropically and the entire undercut area would be filled with metal, leading to a rather unpredictable stripe width. In contrast, a large resist undercut is desirable to fabricate the thermally evaporated palladium contact. It simplifies the lift-off step, flakes along the edge are not present and since thermal evaporation is anisotropic, no metal residues are left in the undercut area.

The DC conductance of this CNT device with one superconducting niobium contact at a base temperature of 20 mK is shown in Fig. 4.5 (b). A single QD is formed, whose energy levels can be tuned by the wide bottom gate. The superconducting density of states causes a current suppression for bias voltages $V_{\text{bias}} < \Delta/e$. A superconducting gap $\Delta \approx 0.7$ eV is inferred. At a magnetic field of 1 T, the gap is completely closed and the Coulomb blockade triangles touch, as shown in Fig. 4.5 (c).

4.2.5. Lead Contacts to Carbon Nanotubes

Another large-gap superconductor is lead, which is of type I. Its bulk value of the superconducting gap is $\Delta \sim 1.3$ eV [66]. Contact to CNTs is achieved with a three-layer system, deposited successively in an e-beam evaporation machine. This process is developed by Jörg Gramich [67]. The 4.5 nm-thin palladium layer on the bottom makes the actual contact to the CNT. A sample stage cooling to a temperature below -40 °C is crucial to obtain a homogeneous layer. Due to their low melting points, the lead and indium layers are evaporated at a sample stage temperature below -90 °C. The indium capping layer prevents lead from oxidising. It is important that lift-off is done at room temperature, without heating. No high-temperature process is possible at all after lead is evaporated due to the low melting point of lead and indium.

Fig. 4.6 (a) shows a CNT with one lead and one palladium contact. A ring of particles around the lead stripe is observed. Measurements of such a sample are very unstable due to charging and discharging of particles next to the CNT. Diffusion of indium and/or lead to the

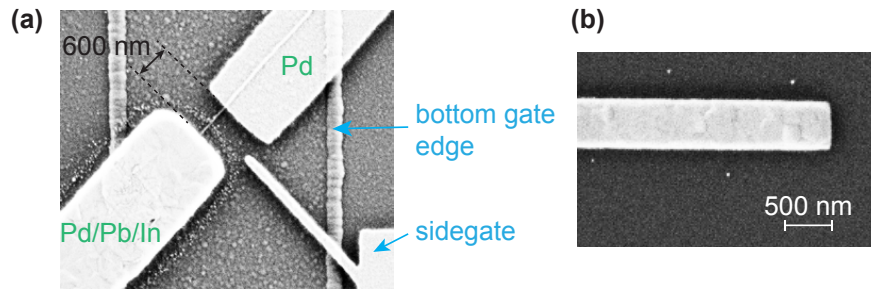


Figure 4.6.: **(a)** CNT device with one palladium/lead/indium (Pd/Pb/In) contact (thicknesses 4.5/110/20 nm) and one Pd contact. There is a side gate plus a wide bottom gate, which is covered with silicon nitride. The Pb stripe is surrounded by a ring of particles. **(b)** A 500 nm-wide Pb stripe with the same capping layers as in (a) on a SiO₂ substrate. There are almost no particles around the stripe because the substrate could be thoroughly cleaned before the ZEP-based lithography.

undercut area causes this particle ring, which is observed on SiO₂ and Si₃N₄ substrate.

If the same lithography with ZEP is repeated on a well cleaned substrate, on which no previous fabrication was done, the number of diffused particles is negligible, as seen in Fig. 4.6 (b). The main difference is that the CNT sample substrate has undergone three PMMA and one ZEP steps before and a thorough surface cleaning was not possible any more because it would destroy the CNT. Resist residues probably turn the substrate surface from hydrophilic to hydrophobic, which enhances the metal diffusion.

In summary, for combining a CNT device with lead contacts and a RF circuit on-chip, a method has to be found to turn the substrate surface hydrophilic again before the lead step without attacking the CNT or perhaps all PMMA steps for fabricating the stub tuner could be replaced by using a thick ZEP resist, which obviously leaves much less residues.

5 Microwave Measurement Setup

A prerequisite for measurements with quantum dots and superconductors is to cool the device to milli-Kelvin temperatures. Only in this temperature range, the thermal energy is well below the energy gap of the superconducting material and the addition energy of a typical quantum dot. We deduced a gap size $\Delta \approx 0.7$ meV for our sputtered niobium (see Fig. 4.5 (b)) and the addition energy of our quantum dots defined in carbon nanotubes is of the order of 15 meV (see Fig. 6.10).

We were in the lucky position to receive a new dilution refrigerator for our project, an Oxford Triton cryogen free system, to build up a dedicated microwave measurement setup. It offers a lot of space inside to place bulky RF components at cold temperatures. The setup is designed to perform RF and DC measurements simultaneously. Inside the cryostat, a base temperature of 20 mK is reached. However, due to the small electron-phonon coupling at low temperature, the conduction electron temperature is higher. Thermal noise measurements indicate an electron temperature of about 100 mK (see Fig. 7.9 (d)) for a device connected to the RF coaxial cable. This corresponds to a thermal energy of $k_B T \approx 90$ μ eV.

Two pictures of the cryostat are shown in Fig. 5.1. The system contains several plates, which are thermally isolated. The temperature decreases stepwise from the top plate to the mixing chamber plate. In operation, metallic cans around the plates act as radiation shields and the entire system is in vacuum to suppress heat exchange. There are two independent, closed cooling cycles. A pulse tube cooler runs the pre-cooling cycle and brings the system to an intermediate temperature. In conventional wet dilution refrigerators, this job is done with a liquid helium bath, which needs to be refilled regularly. Secondly, the dilution cycle running with a mixture of ^3He and ^4He and cools the sample stage to milli-Kelvin temperatures.

Even though the cryostat images look fancy, a clearer understanding of the setup is gained with the help of the sketch in Fig. 5.2. It shows the entire setup and serves as the basis for the rest of the chapter. A detailed list of all components with brand, part numbers and technical specifications is given in appendix D. Since our project included building up the measurement setup, this chapter contains some details on different parts of it and in the end some ideas about possible improvements.

In the meantime, we even received a second cryostat from BlueFors for our project. It is a cryogen free system, too. In this cryostat, we built up a very similar RF setup as in the Triton with some additions. Apart from a measurement line for operation around 3 GHz, there are also lines for 1 and 6 GHz. A very useful component for calibration is a low-temperature RF switch right before the sample holder. It enables to switch the RF connection from the actual device to a reference sample and back. The switching is achieved by sending a voltage pulse to the switch. However, all results presented here are conducted on the Triton setup.

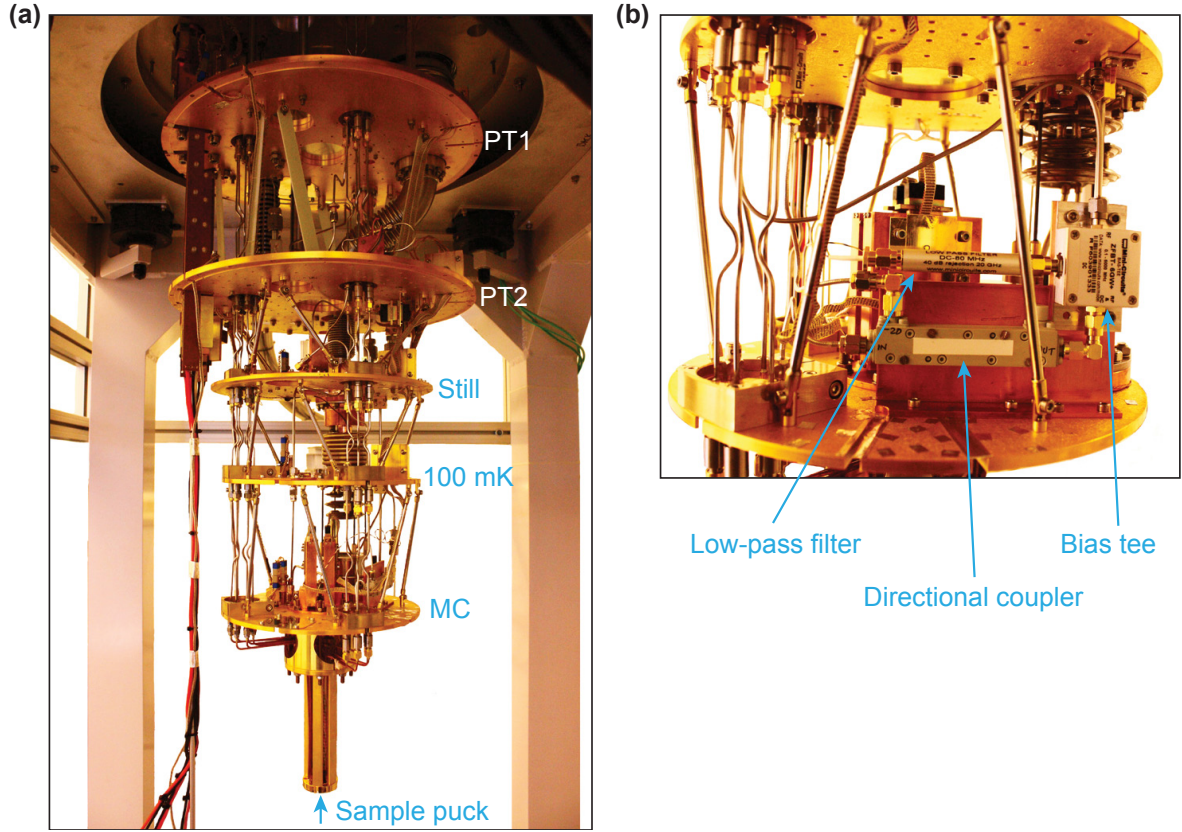


Figure 5.1.: (a) The Triton cryostat without any cans and without magnet. The sample puck is mounted on the circular docking station from below. There are five thermally isolated plates with decreasing temperature from top to bottom. (b) Mixing chamber (MC) plate showing the mounted RF components (without circulator). The MC plate has a diameter of about 40 cm.

5.1. Sample Puck

In this section, we consider the lowermost part, where the sample is mounted. The sample resides inside a so-called puck. A picture of it is seen in Fig. 5.3 (a). The sample holder in the middle is hanging on the DC wires and the coaxial cables. The puck's top part, which is plugged into the docking station of the cryostat, is shown in Fig. 5.3 (b). In this picture, the puck is closed by a metal shield. Round SMP RF connectors are visible, which are connected by pressing (not screwing like SMA connectors).

A printed circuit board (PCB) serves as a sample holder. The first PCB version I designed is shown in Fig. 5.3 (c). Samples are glued into the central area. All connectors are on the front side. There are two SMP connectors for connecting to the coaxial cable and two nano-connectors, which are connected to the two DC looms in the cryostat. The connector pins are soldered to metal lines on the PCB. They lead to the bond pads around the sample area. There are in total 18 pads to connect to DC wires and 2 RF pads. The PCB back side consists of one large ground plane, which is connected by many vias to the ground plane on the front side. The PCB is screwed on a copper plate.

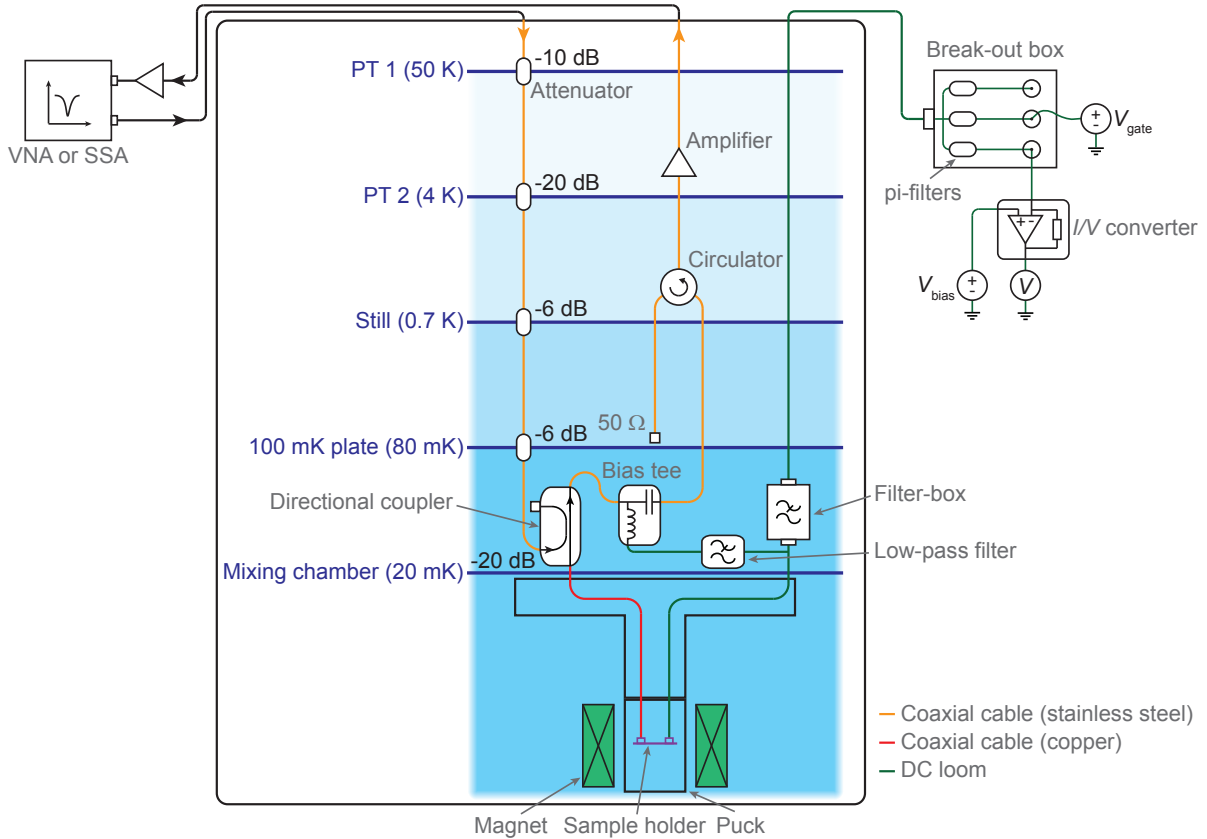


Figure 5.2.: Sketch of the cryogenic measurement setup. For reflection measurements, a vector network analyser (VNA) is used and for noise measurements a signal and spectrum analyser (SSA) with only the RF output line attached.

The puck is placed in the centre of a vector magnet with maximum fields of 6 T in the vertical direction and 1 T in the other two directions. The magnet's hysteresis is determined with a Hall bar sample to be in the range of 3 mT.

Thanks to the bottom loading system, the puck can be exchanged while the system is kept cold with the pre-cooling cycle. This way, a sample exchange can be done within 24 hours until reaching base temperature again.

5.2. RF Wiring

We now follow the RF signal path depicted with arrows in Fig. 5.2. The input line is attenuated at each temperature step to damp radiation leaking from the high-temperature to the low-temperature side. The total attenuation of the input line is ~ 72 dB around 3 GHz. A stainless steel coaxial cable with a low thermal conductivity is used. On the mixing chamber (MC) plate, the signal is fed into a directional coupler. It transmits the signal with 20 dB attenuation to the sample's source contact, where some fraction is reflected. The drain side of the sample is grounded.

The directional coupler guides the reflected signal into a separate output line. The bias tee

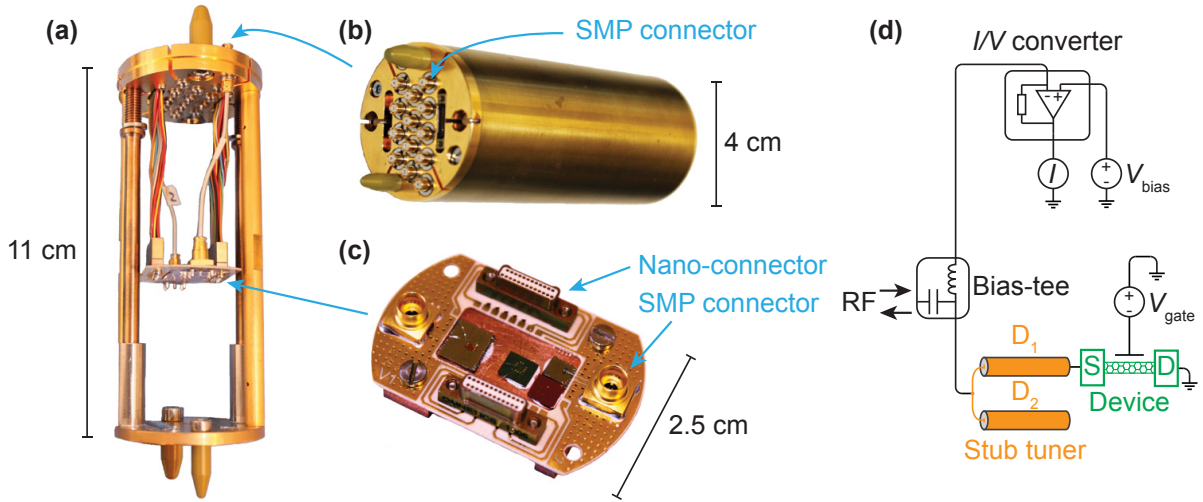


Figure 5.3.: (a) Sample puck with the metal shield removed. DC cables (colored) and two coaxial cables lead to the PCB, which is in the centre. (b) View on the top of the puck. This top plate is plugged into the cryostat’s docking station. The puck is now closed with the metal shield. (c) Sample holder PCB. Samples are glued to the middle area and bonded to the PCB pads around. Close to the PCB edge, there are two high-frequency SMP connectors and two tiny nano-connectors for DC cables from Omnetics. (d) Measurement schematic concentrating on the DC part. The bias voltage is applied to the source (S), while the drain (D) lead is grounded. The DC current is measured on the source side, as well.

enables to apply from this side a DC voltage to the RF port of the sample. A circulator prevents radiation going the way back to the sample, in particular noise generated by the amplifier. A low-temperature amplifier with a gain of about 35 dB is placed on plate 2, followed by one (or for noise measurements even two) room temperature amplifiers, each with a gain ~ 35 dB. In an amplifier chain, the noise added by the first amplifier is magnified the most or in other words the dominant noise source is the first amplifier if its amplification is high enough compared to the amplification of the following one. Therefore it is crucial to use a low-noise cryogenic amplifier.

For reflectometry, the input and output lines are connected to a vector network analyser (VNA). It combines a signal generation unit used for the input signal and a homodyne detection unit to quantify the signal on the output line. The impedances of both ports are $Z_0 = 50 \Omega$. In contrast, noise measurements do not need any RF input signal and a signal. We use a spectrum analyser (SSA) to detect the power on the output line. Also with the SSA, the power dissipated over a resistance of 50Ω is measured.

5.3. DC Wiring

To apply DC voltages to the sample, there are two looms going up the cryostat, each containing 24 constantan wires. Outside the cryostat, the looms are split in a break-out box to access them independently.

What follows is a short description of the way we bias the sample and measure source-drain

current. The corresponding sketch is in Fig. 5.3(d). The sample's source (S) is connected to the RF line and the drain (D) is grounded. For DC measurements, one wire of the loom is merged with the RF line on the MC plate with the help of a bias tee. We measure the DC current I from source to ground with an I/V -converter, where an offset voltage on the I/V -converter establishes the source-drain bias voltage V_{bias} .

RF grounding of the drain contact immediately after the sample is necessary for RF measurements. But with respect to DC measurements, there are two disadvantages if one can only access the source side. The loom bridges the large temperature difference from room temperature to milli-Kelvin temperatures. Since the loom material connecting the sample's source and the cryostat ground material on the drain have different Seebeck coefficients, we encounter a thermal voltage of 6.9 mV between source and drain. If the wires leading to source and drain were of the same material, thermal voltages on both lines would cancel each other. Another issue is that applying a low-frequency excitation to the I/V -converter offset and recording the resulting voltage with a lock-in amplifier gives extremely noisy results. We therefore measure the DC voltage with a multimeter. To circumvent these two issues, we started to place a second bias tee on the drain side. In this way, the RF part is still grounded via a capacitor, whereas the DC part is fed into a loom. The RF grounding has to happen as close to the sample as possible, preferably on-chip.

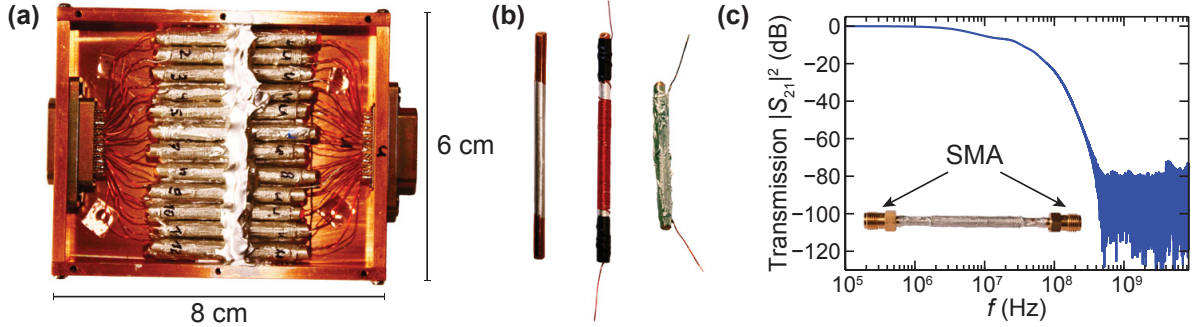


Figure 5.4.: (a) Open filter box with 25 silver-epoxy filters on two layers and Cinch connectors on both sides. The epoxy wall in the middle is a radiation shield between the left and the right side. (b) Pictures of three filter fabrication steps in fabrication order from left to right. (c) Transmission of one filter at room temperature. For that, SMA connectors are attached to both filter ends as shown in the inset.

Like for the coaxial cables, an effective filtering of high-temperature radiation is crucial for the DC cables, too. I constructed a filter box using the design of Scheller *et al.* [68], which is installed on the MC plate. A filter box with a removed cover is shown in Fig. 5.4(a). It contains one silver-epoxy filter rod for each wire. A wall in the middle made out of silver epoxy closes the radiation leak from the left to the right half. How one of these filters looks like is clarified in Fig. 5.4(b). It shows the result after three fabrication steps in fabrication order from left to right. The core is a copper rod of 3 mm diameter. It is covered with some layers of silver paint (from Plano GmbH, article number G302), which results in a soft surface. Next, a 1 m long isolated copper wire (diameter 0.25 mm) is wound around the rod. The last step is to cover the coil with silver epoxy (article number E4110 8OZ, weight ratio between part A and B is 10:1).

The inductance of the coil plus the capacitance to the nearby grounded rod and silver

epoxy layer of $C \approx 2$ pF lead to an LC -filtering effect. But interestingly, it is found that filtering due to the skin-effect is equally important in these filters [68]. The small skin depth at high frequencies reduces the current cross-section to a small annulus. The excellent filtering properties (with a 3 dB point at 6 MHz) are visible in the room temperature transmission measurements of Fig. 5.4(c). These boxes additionally guarantee a decent thermalisation of the electrons in the DC lines to the phonon temperature of the MC plate. This is confirmed with a commercial Coulomb blockade thermometer (CBT) from Aivon, which is fixed on the sample puck and connected to a DC cable. The CBT thermometer holds 33 tunnel junctions in series. The electron temperature can be deduced from the bias width of the conductance dip in Coulomb blockade [69]. We obtain an electron temperature of the DC wires of 32 mK at a base temperature of 20 mK.

5.4. Possible Improvements of RF Wiring

Reflection and noise measurements presented in the following two chapters 6 and 7 confirm that our setup is suited for RF measurements. In the meantime, we gained a good understanding of the circuit's RF properties and found a way for an accurate calibration, as explained in section 7.3.2. Nonetheless, there is room for improvements of the RF wiring.

When the Coulomb blockade thermometer (CBT) was connected to a DC wire, we measured a decent temperature of 32 mK. But the electron temperature of the RF wires seems to be considerably higher. Thermal noise measurements conducted on a metallic wire suggest that its electron temperature is around 100 mK [see Fig. 7.9(d)]. To get a more accurate value, one could once connect the CBT to the RF line. So it might be beneficial to work on the thermalisation. While the coaxial cable's outer conductor is thermally anchored at each plate, the centre conductor is only thermalised through the dielectric between outer and centre conductor. To enhance the centre conductor thermalisation, the coaxial cable can be interrupted on the MC plate by a piece of stripline on a sapphire substrate [70]. Sapphire is a dielectric with a good heat conductivity. In addition, we suspect that the 50Ω terminators on the circulator and the directional coupler deviate at low temperatures from their nominal resistance and thus, they do not absorb all radiation. Therefore, we are going to replace them with cryogenic ones. Likewise, we suspect the characteristic impedance of the coaxial cables to deviate at milli-Kelvin temperatures. An increased dielectric constant results in a higher capacitance and therefore in lower characteristic impedance [see Eq. (2.17)].

In principle, the stub tuner in front of our devices is a good filter for microwave radiation since it reflects all signals, whose frequencies are away from resonance (see Fig. 3.5). Yet, the stub tuner has higher resonant modes and its transmission properties for very high-frequency signals is not clear. There is evidence that quasiparticle generation by infrared light is a mechanism for loss in superconducting resonators [71]. This suggests that attenuating high-frequency signals might be beneficial. Filters made out of Eccosorb material are a good candidate for this purpose [72]. Eccosorb CR-110 is a material that absorbs microwaves above 18 GHz and the attenuation continues at least up to optical frequencies. Eccosorb filters consist of a section of stripline inside a copper box that is filled with Eccosorb.

5.5. RF Dipstick

For the test experiments with $\lambda/4$ -resonators (section 2.4.4) and open stub tuners (section 3.1.5) we built a simple dipstick setup. It is very useful for quick measurements at 4.2 K by dipping into a helium dewar. Two pictures of the dipstick are found in Fig. 5.5. It consists of a tube with two stainless steel coaxial cables and DC wires inside. The overall attenuation of the coaxial cables from top to the sample is approximately 14 dB at 3 GHz. They are attached on the right cold side to the sample copper box with two SMA connectors. Inside the box, the sample is glued in the centre of a PCB, which makes the link between the bond pads and the connectors. There is a thermometer mounted next to the sample box.

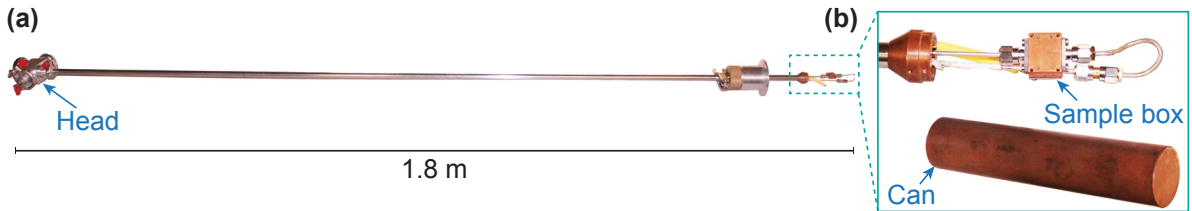


Figure 5.5.: (a) Image of the dipstick for measurements in a helium dewar. The cold part is on the right hand side. Two coaxial cables and DC wires are leading inside a tube to the head, which contains connectors. (b) Close-up view of the cold sample part. There are two SMA connectors at the copper sample box. When cooling down, the copper can is mounted around the sample box.

We directly measure the reflection and transmission coefficients with a vector network analyser without amplification. Because there are no attenuators, circulators or directional couplers, the background standing waves are rather high and a cable calibration is necessary, especially for reflection measurements. For the threefold calibration at room temperature, we replace the sample box by an open, $50\ \Omega$ and a short termination and record the S -parameters for each termination. During the measurements of the actual sample, the network analyser calculates the calibrated coefficients according to the calibration data acquired with the three terminations. It turned out that the setup properties do not change significantly when it is cold. Therefore, using the room temperature calibration data leads to satisfying results.

6 Conductance in the Quantum Dot Regime

Quantum dots (QDs) are small, quasi one dimensional islands for electrons (or holes) with typical sizes from nanometres to a few microns. The strong electron confinement in a QD leads to a discrete energy spectrum and the addition or removal of a single charge becomes observable. The electronic properties of QDs and of atoms show many similarities. Therefore QDs are sometimes called artificial atoms [73]. The experimental control over QDs however is much better than over atoms; with the gate voltage, one can change the electron number on the dot and hence scan through the entire periodic table of such an artificial element. We access the QD via tunnel coupled source and drain contacts and use them to probe the energy spectrum with electronic transport.

Since their first preparation by Endo *et al.* [74], carbon nanotubes (CNTs) have attracted a great deal of attention, not least because of their unique electronic properties. After discovering how to synthesise CNTs consisting of one cylindrical wall [75], the majority of experiments were conducted with single-wall CNTs. If we are talking about CNTs, we therefore mean more specifically single-wall carbon nanotubes. As described in the fabrication sections 4.2.3 to 4.2.5, CNTs can be contacted with various normal and superconducting metals. Given that a natural tunnel barrier forms between metal and CNT, one ends up with a CNT QD by fabricating two contacts on the CNT, which are close to each other.

The purpose of this chapter is twofold. In the beginning, there are two theory sections introducing the electronic structure of CNTs as well as properties of quantum dots in general and when formed in CNTs. The remaining part of the chapter focuses on the low-temperature conductance of CNTs in the QD regime probed with DC and RF reflectometry.

6.1. Electronic Structure of Carbon Materials ¹

A carbon atom has six electrons. Two of them occupy the inner $1s$ shell and are tightly bound to the nucleus. The remaining four electrons, occupying the $2s$ and $2p$ orbitals, are bound weaker. Since the energy difference between the $2s$ and $2p$ states is small compared to the binding energy of chemical bonds, different hybridisations are possible and hence the four valence electrons can make two, three or four bonds to other atoms. Therefore, carbon materials are found in a variety of forms with very distinct properties like three-dimensional diamond and graphite, two-dimensional graphene, one-dimensional CNTs and zero-dimensional fullerene.

6.1.1. Graphene Bandstructure

The starting point to understand the bandstructure of CNTs is graphene, because a CNT can be thought of a rolled-up graphene sheet. Graphene is a flat single layer of carbon atoms. Its

¹This section summarised parts from reference [76]

well-known hexagonal honeycomb lattice with a lattice constant of $a_0 = 1.44 \text{ \AA}$ can be seen in Fig. 6.1 (a). The two lattice vectors \vec{a}_1 and \vec{a}_2 span the marked unit cell, which contains two carbon atoms. Fig. 6.1 (b) shows the graphene lattice in reciprocal space. The reciprocal lattice vectors \vec{b}_1 and \vec{b}_2 , defined via $\vec{a}_i \vec{b}_j = 2\pi \delta_{ij}$, as well as the corresponding first Brillouin zone are indicated. It has six corners, of which the three labelled with K and K' are connected with lattice vectors, what makes them indistinguishable.

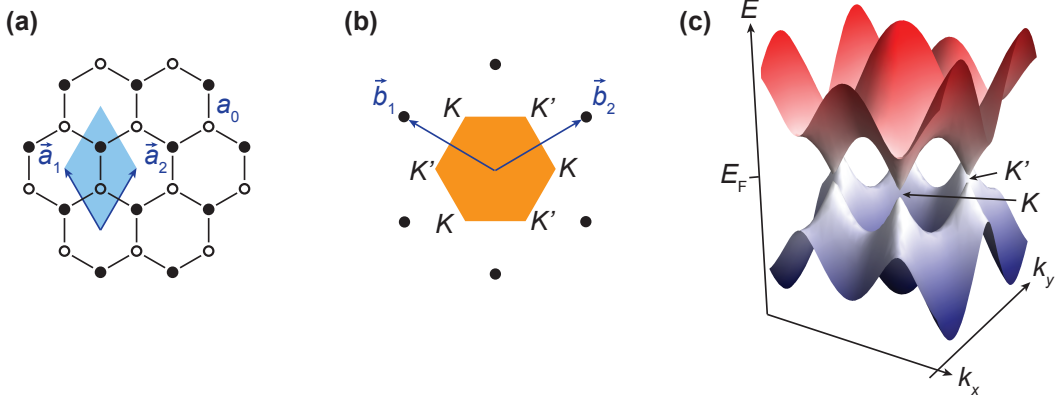


Figure 6.1.: (a) Hexagonal lattice of graphene in real space. Carbon atoms are on each corner. The two lattice vectors \vec{a}_1 and \vec{a}_2 span the unit cell marked with the blue area, containing two atoms. (b) Reciprocal lattice points with the first Brillouin zone in orange. \vec{b}_1 and \vec{b}_2 are the primitive reciprocal lattice vectors. (c) Graphene bandstructure calculated using the tight-binding method (adapted from [77]).

The bandstructure of graphene can be calculated with the tight-binding method, taking into account only nearest neighbour interactions. The result is plotted in Fig. 6.1 (c). There are two bands, which touch at the six corners of the first Brillouin zone. In the case of undoped graphene, the lower band is filled and the upper one is empty. Hence, the Fermi energy E_F is located at the crossing points of the conduction (red) and valence band (blue). For energies close to the Fermi energy - the principal energy range of interest - the bands have the shape of cones and can be approximated by the linear dispersion relation

$$E(\vec{k}) = \pm \hbar v_F |\vec{k}|, \quad (6.1)$$

with the Fermi velocity $v_F = 8.2 \times 10^5 \text{ m/s}$. The energy E is relative to the Fermi energy and the wavenumber \vec{k} is measured with respect to the K or K' points. Because the same dispersion relation also describes massless fermions in the Dirac equation, the points where the bands touch are known as Dirac points, and the nearby bands as Dirac cones. Only one third of each cone is inside the first Brillouin zone and instead, one can consider two full Dirac cones at the positions \vec{K} and \vec{K}' . These two cones give rise to a new degree of freedom, the valley-spin or iso-spin. The two distinct states with wavevectors $\vec{k} + \vec{K}$ and $\vec{k} + \vec{K}'$ are energetically degenerate.

6.1.2. From Graphene to Carbon Nanotubes

A CNT can be thought of a graphene sheet rolled up to a cylinder with a diameter of roughly 1-5 nm. The rolling process is illustrated in Fig. 6.2 (a). There are infinitely many ways how to

select a stripe for rolling up. The CNT structure is specified by the chiral vector \vec{c} . It indicates the direction, in which the graphene sheet is rolled up and goes along the CNT equator. With the help of the real space lattice vectors, the chiral vector is expressed as $\vec{c} = n \cdot \vec{a}_1 + m \cdot \vec{a}_2$, where n and m are integers with $m \leq n$. The special case when $m = 0$ is called a zigzag CNT because a cut of such a tube on the equator has a zigzag edge. Accordingly, the case when $n = m$ is called an armchair CNT. All other cases are named chiral CNTs.

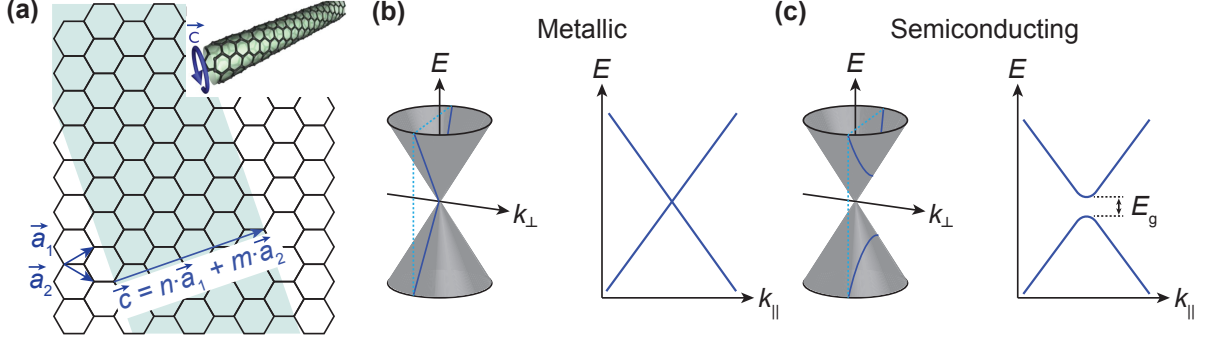


Figure 6.2.: **(a)** Honeycomb lattice of graphene. The green area is rolled up to a CNT with the chiral vector \vec{c} . (adapted from [78]) **(b)** The quantisation of k_{\perp} corresponds to slicing the graphene Dirac cone. If the slice goes through the Dirac point, the CNT is metallic. **(c)** If the slice misses the Dirac point, the bandstructure has a gap E_g and the CNT is semiconducting. (adapted from [63])

With respect to the CNT symmetry, we split the momentum into two components: k_{\parallel} along the CNT and k_{\perp} along the CNT equator. A periodic boundary condition leads to a quantisation of k_{\perp} with spacing

$$\Delta k_{\perp} \cdot \pi d = 2\pi, \quad (6.2)$$

where d is the CNT diameter. Using this condition, one can construct the one-dimensional bandstructure of CNTs out of the two-dimensional bandstructure of graphene. The quantisation of k_{\perp} corresponds to cutting slices out of the graphene Dirac cone, as depicted in Figs. 6.2 (b) and (d). Although the slicing produces many subbands, the CNT diameter in the nanometre range results in a subband separation in the range of electron volts. Hence, already at room temperature, only the lowest subband is populated and talking of one-dimensional transport is completely justified.

In case the cut hits the Dirac point, the CNT bandstructure is not gapped and the CNT turns out to be metallic. In the other case, the bandstructure is gapped. With this argument, approximately one third of the CNTs are metallic and the other two thirds are semiconducting. But experiments revealed that even nominally metallic CNTs have small bandgaps. These gaps were explained either by structural deformations like curvature and strain or by the formation of a Mott insulating state arising in a model, which takes electron-electron interactions into account [79, 80].

6.2. Quantum Dots in Carbon Nanotubes

A CNT naturally confines the electronic wavefunction to one dimension. Tunnel barriers can be introduced in CNTs either with contacts (see end of section 4.2.3) or in semiconducting

CNTs by depleting a short CNT section. If two tunnel barriers in a CNT are close together, the electronic wavefunction in the short CNT segment between is confined in all directions and a QD is formed, as illustrated in Fig. 6.3 (a). When confined to such a small space, Coulomb interactions between electrons (or holes) become important, which makes for instance charging by a single electron observable or in particular gives rise to suppressed shot noise. But as a start, this section gives a brief theoretical description of QDs. In the first part, the energy states arising in QD are explained and in a second part, electronic transport via these states is considered.

6.2.1. Quantum Dot States

The strong charge confinement in a QD gives rise to two kind of energy levels. On the one hand, there is the quantum mechanical confinement energy. Like in the particle-in-a-box problem, the confinement of a single particle leads to a discrete energy spectrum. The level spacing is increasing when the QD size is decreasing. For a QD defined in a CNT, the single-particle level spacing is well approximated by [81]

$$\Delta \approx 1 \text{ meV}/L(\mu\text{m}), \quad (6.3)$$

where L is the QD length in μm . The confinement energy (or single-particle energy) of an electron in state n is denoted by \mathcal{E}_n .

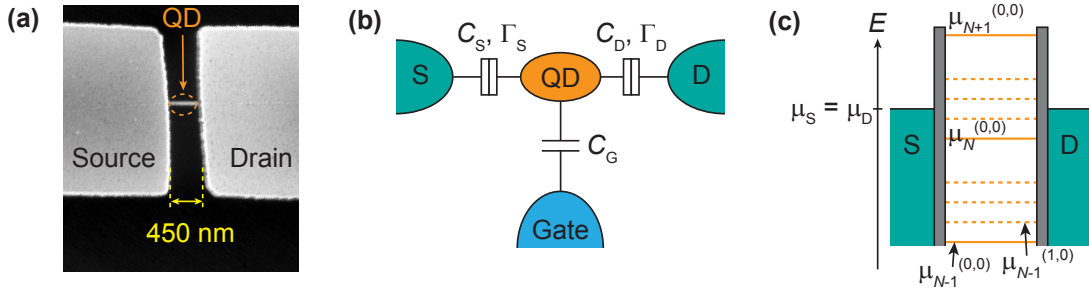


Figure 6.3.: (a) A CNT segment with Ti/Al (4/60 nm-thick) source (S) and drain (D) contacts, forming a quantum dot (QD) between. A large bottom gate is below a silicon nitride layer (not visible). (b) Capacitance model of the QD shown in (a). The tunnel coupling rates to source and drain are Γ_S and Γ_D , respectively. The potential on the QD can be tuned via the gate voltage. (c) Energy level diagram of a QD containing N electrons. The QD is separated with tunnel barriers from source and drain, which are both at the electrochemical potential $\mu = \mu_S = \mu_D$. Ground states are indicated with solid lines and excited states with dashed lines.

Coulomb interaction is not yet considered in this picture, but will prove to play a major role in QDs. It is captured within a capacitance model [82]. As depicted in Fig. 6.3 (b), we consider the QD to be a metallic island with capacitive couplings to source, drain and the gate. The induced charge at the metallic object i is given by

$$Q_i = Q_i^{(0)} + \sum_{j=0}^3 C_{ij} V_j, \quad (6.4)$$

where $Q_i^{(0)}$ is the offset charge when all potentials are at zero as resulting from doping or impurities. Source, drain and gate have indices $i = 1, 2, 3$. The voltages applied to them are known, but Q_i are not. The index $i = 0$ denotes the QD itself. Here, V_0 is unknown but the charge is known to be a multiple of the elementary charge, $Q_0 = -|e|N$. Solving for the potential on the dot leads to

$$V_0 = \frac{Q_0 - Q_0^{(0)}}{C_\Sigma} - \sum_{j=0}^3 \frac{C_{0j}}{C_\Sigma} V_j, \quad (6.5)$$

with $C_\Sigma = C_{00} = -\sum_{i=1}^3 C_{0i}$ being the sum of the capacitances around the QD. The lever arms of the gates $\alpha_i = -C_{0i}/C_\Sigma$ are given by the geometry. Now, the electrostatic energy required to add N electrons on the dot can be determined:

$$E(N) = \int_{Q_0^{(0)}}^{Q_0^{(0)} - |e|N} V_0 dQ_0 = \frac{e^2 N^2}{2C_\Sigma} - |e|N \sum_{j=1}^3 \alpha_j V_j. \quad (6.6)$$

The total energy of a QD, which is populated with N electrons, is the sum of the confinement energy \mathcal{E}_n and the electrostatic energy:

$$E_{\text{tot}}(N) = \sum_{n=1}^N \mathcal{E}_n + \frac{e^2 N^2}{2C_\Sigma} - |e|N \sum_{j=1}^3 \alpha_j V_j. \quad (6.7)$$

In the constant interaction model, it is assumed that the capacitance C_Σ and the confinement energy \mathcal{E}_n are both independent of the QD occupancy N . In this approximation, the electrochemical potential of the QD is

$$\mu_N = E_{\text{tot}}(N) - E_{\text{tot}}(N-1) = \mathcal{E}_N + \frac{e^2}{C_\Sigma} \left(N - \frac{1}{2} \right) - |e| \sum_{j=1}^3 \alpha_j V_j. \quad (6.8)$$

The electrochemical potential is the energy needed to fill the QD with the N -th electron. Due to the constant interaction approximation, the electrochemical potential describes a ladder with equal spacings

$$\mu_N - \mu_{N-1} = \Delta + \frac{e^2}{C_\Sigma}. \quad (6.9)$$

This so-called addition energy expresses how much more energy is required to add the next electron on the QD. The term $E_c = e^2/C_\Sigma$ is called charging energy and originates from classical electrostatics. An expression for the single-particle level spacing in CNT QDs is given in Eq. (6.3). The size of QDs in CNTs is such that usually $E_c > \Delta$. The potential ladder is illustrated in Fig. 6.3(c). The solid lines mark the electrochemical QD potentials. At zero temperature, the leads are filled up to the Fermi level $\mu_S = \mu_D$ and the number of electrons on the QD is fixed to N . The QD is said to be in Coulomb blockade since Coulomb interaction prohibits the addition of more charges. According to Eq. (6.8), the QD levels can be moved linearly with the gate voltage. Only if the lead Fermi levels are at the same height as μ_N , the Coulomb blockade is lifted and the number of electrons fluctuates between N and $N-1$.

So far, we neglected the valley degeneracy discussed in section 6.1.1 and the spin degeneracy. Hence, each quantum mechanical state in CNTs can be filled with four electrons without paying the energy Δ and the ladder spacing of Eq. (6.9) becomes N -dependent. If a new confinement

state is occupied, the full addition energy $\Delta + E_c$ is needed. But filling the three subsequent levels only requires an addition energy of E_c .

Finally, we consider that electrons can be in excited confinement states. To include this, the QD energy of Eq. (6.7) is labelled by $E_{\text{tot}}^{(k)}(N)$ with the integer k , where $k = 0$ denotes the ground state. The labelling of the electrochemical potential is extended to $\mu_N^{(k,l)} = E_{\text{tot}}^{(k)}(N) - E_{\text{tot}}^{(l)}(N-1)$. Again, the ground state $\mu_N^{(0,0)} = \mu_N$. Some excited state levels are indicated in Fig. 6.3 (c) by dashed lines.

6.2.2. Transport through Quantum Dots ²

The previous section was devoted to an equilibrium situation. Now, electronic transport through QDs is considered arising from the tunnel coupling of the QD to source and drain leads and an applied bias voltage. Large tunnel couplings imply on the one hand a well measurable transport signal but on the other hand relax the charge localisation on the QD. The following argument sets a limit to the tunnelling resistances R_t to observe single electron tunnelling. With C_Σ being the QD capacitance and R_t the tunnelling resistance between one lead and the QD, the time to charge the QD via this lead is given by the RC -time constant: $\Delta t = R_t C_\Sigma$. The Heisenberg uncertainty relation states that $\Delta E \Delta t > \hbar$. The requirement to resolve at least the charging energy $\Delta E = E_c = e^2/C_\Sigma$ translates to a lower bound for the tunnelling resistance:

$$R_t > \frac{\hbar}{e^2}. \quad (6.10)$$

In words, the tunnelling resistance must be larger than the resistance quantum $\hbar/e^2 = 25.831 \text{ k}\Omega$.

Taking into account the thermal energy leads to a second criterion for charge quantisation on the dot:

$$k_B T \ll \frac{e^2}{C_\Sigma}. \quad (6.11)$$

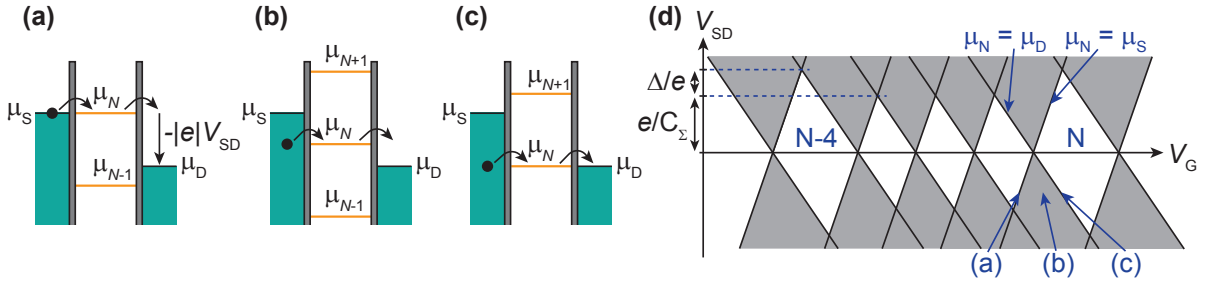


Figure 6.4.: (a)-(c) Three energy level diagrams with an applied bias voltage V_{SD} , not including excited states. Electron tunnelling is sketched with arrows. (d) Schematic Coulomb blockade diamonds in the presence of fourfold degeneracy, not considering excited states. The number of electrons is fixed in the white areas and current can flow in the grey areas. The points which correspond to the level diagrams in (a)-(c) are marked with arrows.

Charge transport in the QD-lead system is determined by the positions of the electrochemical potentials. Three possible configurations are illustrated in the energy level diagrams of

²According to chapter 18 in [82]

Figs. 6.4 (a)-(c). If a bias voltage V_{SD} is applied between source and drain, their electrochemical potentials μ_S and μ_D differ by eV_{SD} . The energy range between these Fermi levels is called bias window. If a QD level is inside the bias window, electrons can tunnel on and off the dot. Because of the finite bias, sequential tunnelling from one to the other lead occurs through the QD.

The tunnelling dependence on the gate and bias voltages leads to the characteristic Coulomb blockade diamonds sketched in Fig. 6.4 (d). In the white diamond-shaped areas, first-order tunnelling is energetically forbidden. Hence, the number of charges on the dot is fixed and the QD is called to be in Coulomb blockade. This Coulomb blockade is lifted in the grey areas, where a finite current is flowing and the charge number on the dot is fluctuating. The Coulomb blockade boundaries can be readily determined with the capacitance model. Along the line with negative slope s^- , the QD level stays aligned with μ_D , as depicted in Fig. 6.4 (c). We assume that the drain side is on ground. The general expression for the QD potential is in Eq. (6.5). A change of the dot potential by V_G has to be fully compensated by the source:

$$\frac{C_G}{C_\Sigma} \Delta V_G = -\frac{C_S}{C_\Sigma} \Delta V_S \quad \Rightarrow \quad s^- = \frac{\Delta V_{SD}}{\Delta V_G} = -\frac{C_G}{C_S}. \quad (6.12)$$

Likewise, the QD level is fixed to μ_S along the line with positive slope s^+ . This situation is sketched in Fig. 6.4 (a). A QD potential change is compensated by the bias voltage, while also taking into account the influence of the source potential on the QD level:

$$\frac{C_G}{C_\Sigma} \Delta V_G = \Delta V_{SD} - \frac{C_S}{C_\Sigma} \Delta V_S \quad \Rightarrow \quad s^+ = \frac{C_G}{C_G + C_D}. \quad (6.13)$$

The addition energy sets the size of the Coulomb blockade diamonds. The pattern arising from a fourfold level degeneracy as it is present in clean CNT QDs is sketched in Fig. 6.4 (d). The charging energies can be read out from the bias needed to close the diamonds, as marked in the figure.

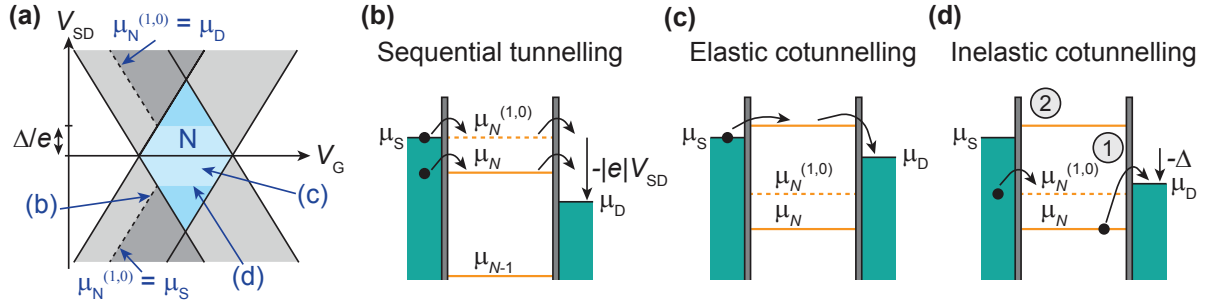


Figure 6.5.: (a) Schematic of one Coulomb blockade diamond, including the presence of one excited state with electrochemical potential $\mu_N^{(1,0)}$. A cotunnelling current appears in the blue Coulomb blockade areas and a sequential tunnelling current in the grey areas. (b)-(d) In these energy diagrams, the corresponding transport processes for three points marked in (a) are sketched.

Apart from transitions involving the QD ground state, there can also be elastic transitions via excited states. Such a sequential tunnelling event is drawn in Fig. 6.5 (b). The conditions are that $\mu_N^{(1,0)}$ and the ground state μ_N are both in the bias window. This additional transition

channel via an excited state enhances the chance of a charge transfer and therefore leads to an increased current in the dark grey area of Fig. 6.5 (a).

While first-order tunnelling processes are not allowed inside the Coulomb blocked region, second-order processes can occur. Heisenberg's uncertainty principle allows to break the law of energy conservation for a short time. Because it has to happen quickly, the tunnelling rates need to be large in order to observe cotunnelling. As illustrated in Fig. 6.5 (c), an electron can tunnel from source to drain via a virtual state on the QD, which is higher in energy than μ_S . The process is elastic (energy-conserving) in the sense that the QD is kept in the same state before and after the charge transfer.

But inelastic cotunnelling events are possible, as well. One of them is drawn in Fig. 6.5 (d), where two electrons tunnel in a correlated fashion. First, an electron leaves the dot by tunnelling to drain, before another electron enters from the source lead. During this process, the QD is brought from the ground state to the excited state. For this, the applied bias has to be at least Δ , the single-particle level spacing.

Both, elastic and inelastic cotunnelling result in a small current in the Coulomb blockade, indicated as blue area in Fig. 6.5 (a). The dark blue area marks the bias regime where inelastic cotunnelling is possible.

6.2.3. Double Quantum Dots

Two QDs in series can be formed in a CNT with the help of more than one bottom gate. The characteristics of double QDs are briefly mentioned here as the last part of the introductory section.

A complete capacitance model of two QDs in series is drawn in Fig. 6.6 (a). An electron transfer from source to drain involves three sequential tunnelling events from source to QD₁, from QD₁ to QD₂ and finally from QD₂ to drain. The dots' electrochemical potentials are dominantly tuned by the voltage on the respective closest gate.

The so-called charge stability diagram is given in Fig. 6.6 (b). The x -axis is the potential on gate 1 and the y -axis the potential on gate 2. Inside the hexagonal regions, the charges on the dots is fixed. A level diagram for the situation when a level of QD₁ is on the same height as the source Fermi level is shown in Fig. 6.6 (c). The corresponding transition line in the charge stability diagram (b) between the charge states $(N - 1, M)$ and (N, M) is not vertical but has a negative slope due to the small capacitive coupling of the second gate to QD₁.

But owing to the interdot coupling, the charge state on one QD influences the electrochemical potential on the other dot. The level positions in QD₂ in the diagram of Fig. 6.6 (c) depend on whether μ_N is occupied or not. This interdot level dependence gives rise to the lines with positive slope in the charge stability diagram. They mark the situation when interdot charge transitions are happening $[(N - 1, M) \leftrightarrow (N, M - 1)]$. The two ends of these lines are called triple points. At these points, the two QD levels and the lead Fermi levels are all aligned. As drawn in the level diagrams of Figs. 6.6 (d) and (e), the two triple points correspond to the situations when the empty and occupied dot levels are aligned with the lead Fermi levels, respectively.

Charge transport from source to drain via sequential tunnelling is only possible at the triple points. At the lines with negative slopes in the charge stability diagram, a current can only flow with the help of cotunnelling processes, whereas no current at all is flowing to the leads along the lines with positive slopes. In summary, the lines with negative slopes are only visible when all tunnel couplings are large and the lines with positive slope are not visible at all.

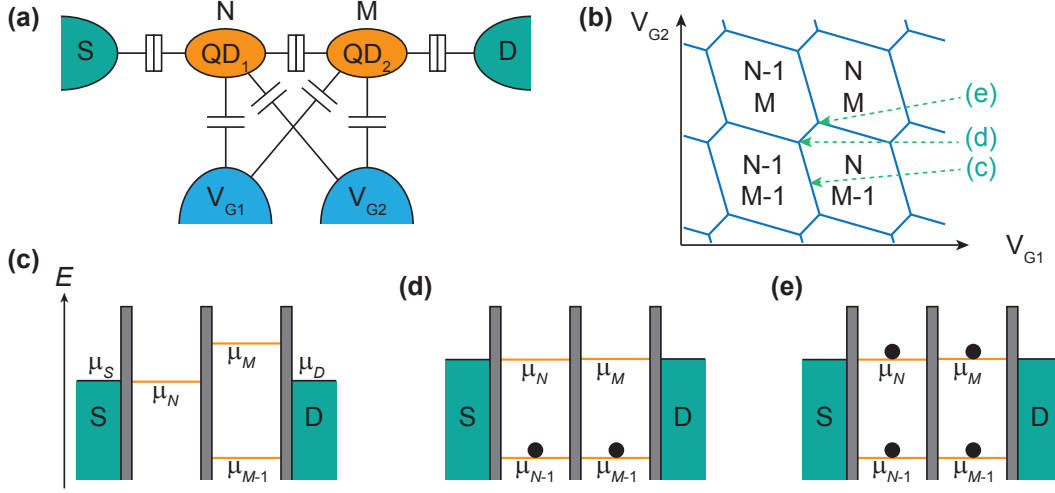


Figure 6.6.: (a) Capacitance model for a double dot system. Source (S), QD₁, QD₂ and drain (D) are tunnel coupled in series. The QD levels are tuned by two gates. (b) Charge stability diagram marking the gate voltage regions with fixed charges. The upper and lower labels denote the charge number on QD₁ and QD₂, respectively. The lines mark the situations when one or both QDs are on resonance with the Fermi level of the adjacent lead. The corresponding positions for the level diagrams in (c)-(e) are marked. (c) Energy level diagram on a transition line of QD₁. (d) Level diagram at the triple point, where both dot levels aligned to the lead Fermi level are empty. (e) These levels are occupied at the other triple point.

The situation is different when the double dot system is coupled to an RF resonator. Interdot charge transitions and transitions between one dot and a lead cause a capacitance change, which is detected as a resonance frequency shift [31, 83, 84] [see section 6.5 and Fig. 3.3 (d)].

6.3. Conductance Measurements of a Quantum Dot

After the theoretical introduction to QDs, this section is devoted to measurements. To start with, the investigated sample is introduced. According to the recipe described in section 4.2 and listed in more detail in appendix C, we fabricated a CNT device with an on-chip stub tuner attached to the source contact. An image of the CNT part is shown in Fig. 6.7 (a) and a schematic cross-section in Fig. 6.7 (b) for clarity. The stamped CNT crosses four parallel bottom gates coloured in yellow; two narrow ones of width 100 nm in the centre and two wider ones of width 300 nm on the sides. These wider gates are partially beneath the leads and meant to adjust the doping of the CNT segments there. The CNT is separated by the gates with a 50 nm-thick silicon nitride layer. Normal metal contacts to the CNT are established with Ti/Au leads of thicknesses 10/40 nm.

After finishing the fabrication of the CNT device, it is protected with a resist mask and the stub tuner is fabricated next to it. An overview picture of the final sample is shown in Fig. 6.7 (c). The CNT device resides in the dark left area. Its source is connected to one end of the stub tuner, whereas its drain is connected to the ground plane. The stub tuner input launcher is on the right. As discussed in section 3.1.5, the two black bond wires next to the

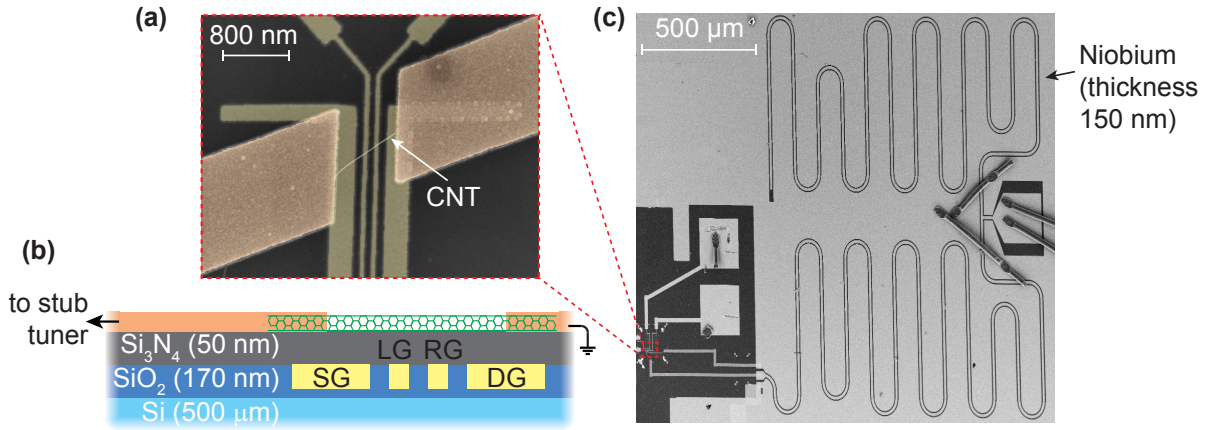


Figure 6.7.: **(a)** False-color image of the CNT connected to Ti/Au leads (orange) and bottom gates underneath (yellow), which are covered with silicon nitride. **(b)** Sketch of the cross section. The gates called source gate (SG), drain gate (DG), left gate (LG), and right gate (RG) are covered with silicon nitride. The CNT is stamped on top and contacted with Ti/Au leads. **(c)** SEM image of the stub impedance-matching circuit made with niobium. The $50\ \Omega$ side is at the launcher on the right, and the CNT device is located at the bottom left. The two bond wires on the right next to the RF launcher are airbridges to connect the ground planes. There are two square bond pads for the gates visible close to the CNT. (Reprinted with permission from [44]. © 2015 by The American Physical Society.)

T-junction, where the CTLs split, are essential to suppress spurious modes. The meander structure of the two CTL arms is used to squeeze the stub tuner into the e-beam writefield of $2 \times 2\ \text{mm}^2$. The ground plane is well connected to the sample holder ground via densely spaced bond wires all around the chip edge (not seen in the figure). The bottom gates are connected to large bond pads; two of them are visible in the figure close to the CNT.

The measurement setup within the Triton cryostat is explained in detail in chapter 5. Basically, the stub tuner is connected to an RF input and output line for reflectometry experiments. Furthermore, a DC cable coupled to the RF line via a bias tee enables to apply a DC bias and to record the DC current simultaneously with RF measurements. We reach a base temperature of 20 mK, but the electronic temperature on the source side is rather in the range of 100 mK, as discussed in section 7.3.2.

An overview of the CNT device characteristics is gained with Fig. 6.8 (a). It shows the DC current dependence on the gate voltages on the left and right narrow gates (V_{LG} and V_{RG}). The two gates below the contacts, called source gate (SG) and drain gate (DG), are both kept at a potential of $-3\ \text{V}$ to have p -doped CNT segments next to the leads. This scan over large gate voltage ranges can be divided into four main regions, (I)-(IV). They are separated by stripes of zero current, where the bias window is inside the band gap in a CNT segment above one of the gates.

The sketches in Fig. 6.8 (b) show roughly the valence and conduction band edges along the CNT for the four regions. In region (I), the two central gates define one large QD. In the enlarged current map of Fig. 6.8 (c), parallel resonance lines with slope -1 are visible. Hence the QD levels can be equally tuned with both the left or the right gate.

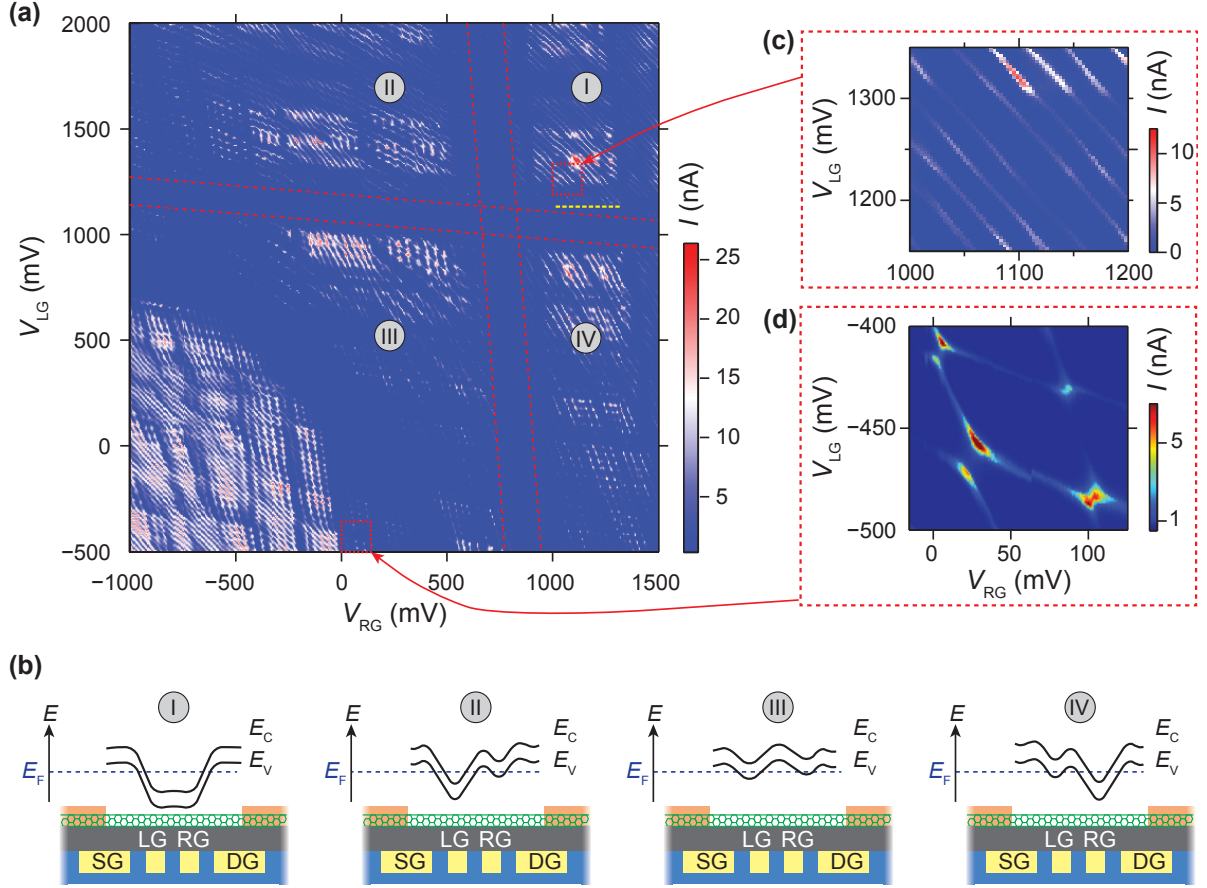


Figure 6.8.: (a) DC current as a function of the voltages on the left gate (LG) and right gate (RG) over a huge range at a base temperature of 20 mK. The source-drain bias is at 1 mV and the source gate (SG) as well as the drain gate (DG) are kept at -3 V to have p -doped leads. The current is suppressed between the red dashed lines, where the Fermi level lies inside the bandgap for a long CNT segment. These bandgap transitions separate regions (I)-(IV). The yellow horizontal dashed line in region (I) marks the gate voltage range used for all following measurements in the single QD regime. The left gate is fixed to $V_{LG} = 1076$ mV. (b) Rough sketches of the valence (E_V) and conduction (E_C) band edges with respect to the Fermi level (E_F) for the four regions of the current map. (c) Enlarged current map in the single QD regime of region (I) and (d) in the double QD regime of region (III). (Reprinted with permission from [44]. © 2015 by The American Physical Society.)

The situation is less clear in regions (II)-(IV). In some areas, clear double dot features appear, like in the enlarged current map of Fig. 6.8 (d). In other areas, the features are hardly visible due to a strongly suppressed current or they are washed out due to large tunnel couplings. Furthermore, there are areas where lines with a third slope hint at the presence of a triple dot (not shown in a separate figure). There are several possible reasons for the various features observed in zones (II)-(IV). For instance, impurities in the substrate below the CNT can locally

change the potential or disorder in the CNT can introduce an additional barrier.

In any case, we stay in the single QD regime of region (I) for all following experiments. More precisely, we fix the left gate to $V_{LG} = 1076$ mV and sweep V_{RG} along the yellow dashed line in Fig. 6.8(a) to change the QD level. In this way, we are able to form a clean single QD.

6.3.1. Stub Tuner Characterisation

Now, we turn our attention to the other part of the sample, the stub impedance-matching circuit. The resonance frequency of the fundamental mode is close to the planned value of 3 GHz and is well inside the setup bandwidth. We consider first the stub tuner response when the QD is in the Coulomb blockade. The measured reflection amplitude spectrum around the resonance frequency is plotted as blue triangles in Fig. 6.9(a). This spectrum in the blockade serves as a reference for extracting the stub tuner parameters. Like already demonstrated with the open stub tuner in section 3.1.5, one can extract the circuit parameters from the reflection spectrum. A detailed description of the fitting procedure is given in appendix B.1.1. A fit to Eq. (3.14) assuming $G = 0$ leads to the set of parameters given in the figure caption. The stub tuner lengths are close to the design values. The damping $\alpha = 0.046$ m⁻¹ corresponds to an internal quality factor of about 1600. The frequency-dependent background reflection is taken into account by a linear curve, represented with a black solid line in the figure. The values for the two CTL parameters, the characteristic impedance $Z_0^* = 44.8$ Ω and the effective dielectric constant $\epsilon_{\text{eff}} = 6$, are obtained by simulations with the software Sonnet.

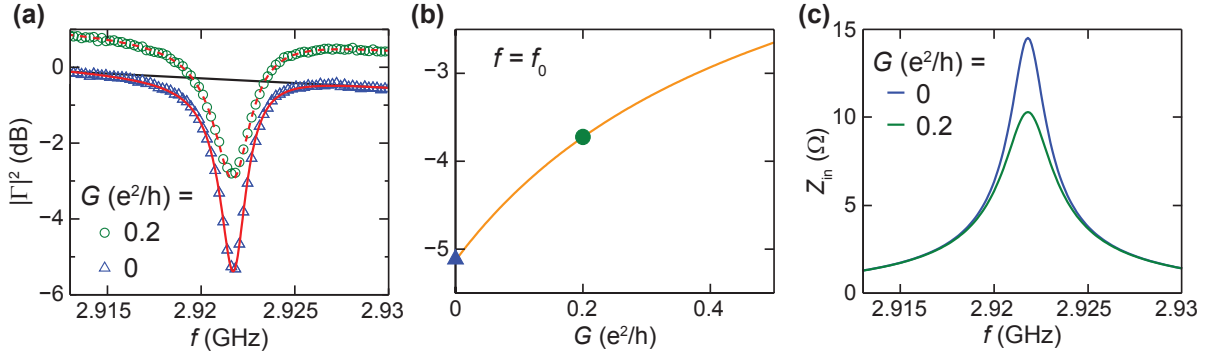


Figure 6.9.: Stub tuner properties at a base temperature of 20 mK. **(a)** Amplitude squared of the reflection coefficient Γ around the resonance frequency. Symbols are measured and lines fitted or calculated. The stub tuner loss $\alpha = 0.046$ m⁻¹ as well as the two CTL lengths $D_1 = 10.355$ mm and $D_2 = 10.589$ mm are extracted by fitting (solid red line) to the spectrum in the Coulomb blockade regime of the QD (blue triangles), where $G = 0$ is assumed. The black solid line represents the linearised background reflection. The upper spectrum for a finite DC conductance of $G = 0.2$ e^2/h is plotted with a shift of 1 dB for clarity (green circles). It matches well the calculated reflection coefficient (dashed red line) using the previous fit parameters. **(b)** This plot shows the calculated conductance dependence of the reflectance amplitude at the resonance frequency using the previous fit parameters. The two values corresponding to the spectra in (a) are marked. **(c)** Calculated stub tuner input impedance for two conductances of the attached load. (Reprinted with permission from [44]. © 2015 by The American Physical Society.)

The second spectrum in Fig. 6.9 (a), shown with green circles, is measured at a point where the DC differential conductance is $G = 0.2 e^2/h$. There is a good agreement to the calculated reflection spectrum for this conductance when inserting the stub tuner parameters extracted in the blockade to Eq. (3.14), as shown by the red dashed line. This example indicates that all relevant parameters to characterise the stub tuner are gained by fitting to the reflection spectrum in the Coulomb blockade and we are going to use these parameters for all following calculations concerning this sample.

Even though the curves are shifted vertically, it is already visible that the resonance for $G = 0.2 e^2/h$ is shallower. Knowing the stub tuner parameters, one can calculate the full load conductance dependence of the resonance. The reflection amplitude dip at the resonance frequency f_0 is shown in Fig. 6.9 (b) as a function of conductance. The resonance is deepest when $G = 0$, meaning the circuit is best matched to low conductances. The monotonic increase with conductance suggests that the differential conductance can be derived from the resonance amplitude. This possibility is further investigated in the next section.

The stub tuner input impedance Z_{in} of Eq. (3.10) is the impedance experienced at the input launcher towards the direction of the device. Fig. 6.9 (c) shows its calculated frequency dependence for this sample around f_0 for two conductances. As already mentioned in section 3.1.2, the stub tuner looks at the input as an almost zero-impedance circuit for gigahertz frequencies. Only close to the resonance frequency, the impedance rises. The peak impedance of this stub tuner at best matching, when $G = 0$, is still well below the full matching case of $Z_{\text{in}} = 50 \Omega$, meaning that perfect matching is never achieved with this sample. In agreement with Fig. 6.9 (b), a load of $G = 0.2 e^2/h$ is more away from matching and hence the impedance peak is lower.

6.3.2. DC and RF Conductance

For the following experiments, we keep the CNT device in the single QD regime. The left gate is fixed to $V_{\text{LG}} = 1076 \text{ mV}$ and the right gate is used as a plunger gate. The used gate voltages are indicated in the gate-gate map of Fig. 6.8 with the yellow dashed line.

Fig. 6.10 shows two differential conductance maps for the same gate and source-drain voltage (V_{SD}) ranges. For panel (a), the DC current I is recorded and its derivative dI/dV_{SD} is plotted. The Coulomb diamond contours are marked. The first and the fifth diamonds is larger than the rest. This is the same pattern as sketched in Fig. 6.4 (d) for fourfold spin and valley degenerate QD states in CNTs. The observation of the fourfold degeneracy is a sign for a low-disorder CNT segment forming the QD island. A charging energy $E_c = 12 \text{ meV}$ can be directly read out from the height of the small diamonds. The single-particle level spacing Δ is equal to the spacing of the excited states, which amounts to about 8 meV . With the relation between Δ and the QD length in CNTs stated in Eq. (6.3), one obtains a QD length $L \approx 130 \text{ nm}$. This leads to the conclusion that the QD is located mainly between the two central gates, which are separated by 100 nm .

The conductance shown in Fig. 6.10 (b) is derived from reflectometry. For that, the reflection amplitude at the stub tuner resonance frequency f_0 is detected. Then, the amplitude dip dependence on conductance, as plotted in Fig. 6.9 (b), is exploited. Since the function $|\Gamma(G)|^2$ of Eq. (3.14) can not be inverted by hand, we are looking for an easily invertible approximate function. We found that $|\Gamma(G)|^2$ can be well approximated by

$$|\Gamma(G)|^2 \approx a \cdot \left(\frac{1}{G} - b\right)^c + d \quad \Rightarrow \quad G(|\Gamma|) \approx \left[\left(\frac{|\Gamma| - d}{a}\right) + b\right]^{-1}, \quad (6.14)$$

with the parameters for this stub tuner being $a = 2560 \text{ 1}/\Omega$, $b = -21.1 \cdot 10^3 \Omega$, $c = -0.85$ and $d = 0.55$. This function is purely empirical and has no further physical meaning. $G(|\Gamma|)$ directly converts the measured reflection amplitude at resonance to the device conductance. Before the conversion, the background reflection has to be taken into account. This is done by subtracting (in decibel scale) the background value (black line in 6.9 (a)) at f_0 from $|\Gamma|$.

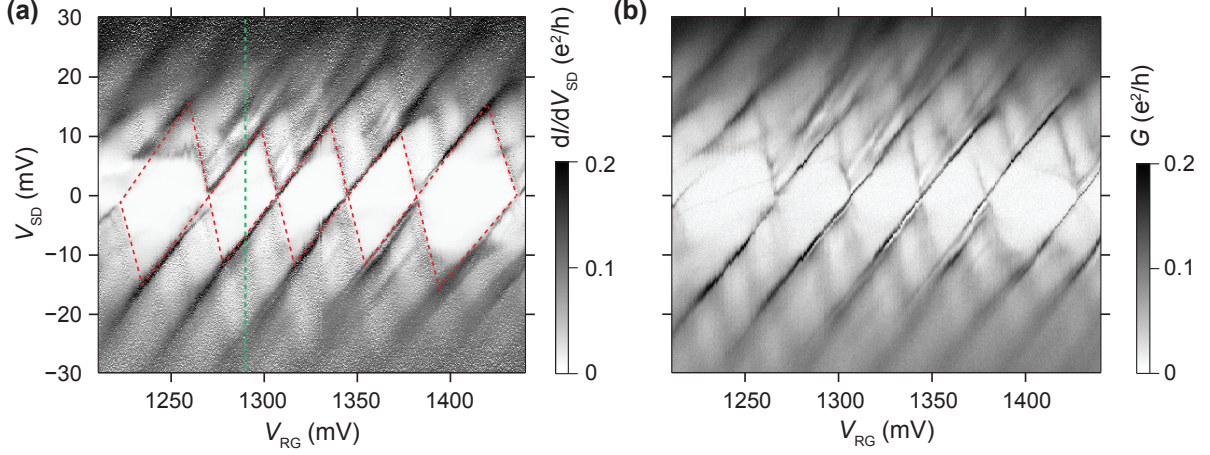


Figure 6.10.: Measurements in the single QD regime along the yellow dashed line in Fig. 6.8. ($V_{LG} = 1076 \text{ mV}$, $V_{SG} = V_{DG} = -3 \text{ V}$) at a base temperature of 20 mK. **(a)** Derivative of the DC current (dI/dV_{SD}) as a function of the voltage on the right gate and of the source-drain bias. The contour of the CB diamonds is highlighted by the dashed line. **(b)** Differential conductance deduced from the reflection amplitude. The procedure is explained in the text. (Reprinted with permission from [44]. © 2015 by The American Physical Society.)

One can see a good agreement between the RF and DC conductance maps in Fig. 6.10, at least qualitatively. The same features are visible in both plots. To confirm the quantitative agreement, a cut at $V_{RG} = 1296 \text{ mV}$ along the green dashed line in Fig. 6.10 (a) is shown in Fig. 6.11 (a). In spite of the DC conductance being noisier (it is the numerical derivative), the two conductance curves overlap quite well.

Spectra at the same gate voltage as a function of V_{SD} are shown in Fig. 6.11 (b). The resonance dip is deepest (black) inside the Coulomb blockade. The diamond boundaries are marked with arrows. There, the conductance spikes lead to a clearly visible dip increase. This colourmap points out that there is only little conductance dependent resonance frequency shift. The same spectrum maps are recorded in the entire gate voltage range of Fig. 6.10. The observed frequency shifts relative to the resonance frequency in the blockade $f_0 = 2.9218 \text{ GHz}$ [see Fig. 6.9 (a)] are plotted in Fig. 6.11 (c). The Coulomb blockade diamonds are slightly recognisable. The frequency shifts inside the blockade downwards by about 120 kHz. This converts to a quantum capacitance change of about 120 aF [see Fig. 3.3 (d)], which is on the same order than literature values [85]. Compared to the stub resonance bandwidth of about 3 MHz, the frequency shift is less than one twentieth. Thus the mistake is small when converting the reflection amplitude at the fixed frequency f_0 to conductance.

The speed limit of conventional direct conductance measurements is set by the RC time constant. The cutoff frequency for measuring a resistance R with a wiring of capacitance C is

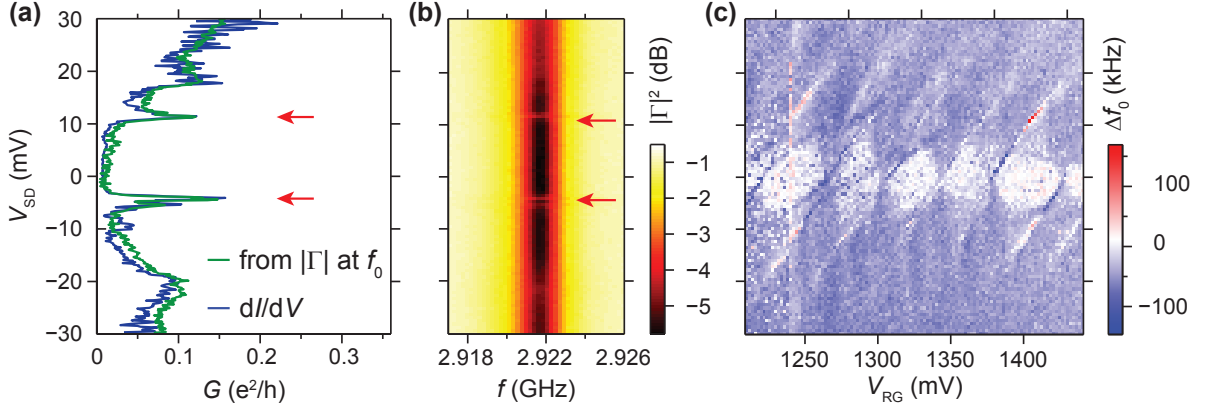


Figure 6.11.: (a) Differential conductance G along the green dashed line in Fig. 6.10 (a), where $V_{\text{RG}} = 1296$ mV. The blue curve is the numerical differential conductance dI/dV_{SD} obtained from the DC current, whereas the green curve is extracted from the reflection amplitude at the resonance frequency f_0 . (b) Reflection amplitude spectra around the resonance frequency as a function of bias voltage at the same gate voltage as in (a). The red arrows mark the Coulomb blockade boundaries. (c) A reflection spectrum is recorded at each point in the bias and gate range of Fig. 6.10. The colour plot shows the resonance frequency shift Δf_0 relative to $f_0 = 2.9218$ GHz in the blockade [see blue spectrum in Fig. 6.9 (a)], when comparing the frequencies at the reflection amplitude minima.

given by

$$f_c = \frac{1}{2\pi RC} \approx 1.6 \text{ kHz}, \quad (6.15)$$

assuming a device of 100 k Ω and a typical capacitance of the cryostat wiring of 1 nF resulting from the coaxial cables and filters. With the help of impedance transformation, one can circumvent this RC -time limitation. The group of Jason Petta has pushed the speed of conductance read-out to the limit by coupling a double QD to a gigahertz resonant circuit and by the use of a Josephson parametric amplifier. They succeeded to obtain a charge stability diagram of a double QD device within 20 ms [86]. So far, we have not exploited the potential of fast measurements yet. First of all, one needs the suitable equipment, for instance a fast analog-to-digital converter. Secondly, we are also recording the DC current simultaneously, which makes the read-out slow. Especially in the beginning, it is important to double-check G extracted from reflectometry with the DC value. Moreover, differences between RF and DC conductance might even reveal interesting physical effects [87, 88].

6.4. Quantum Dot with One Niobium Lead

The CNT device with one normal Pd and one superconducting Nb contact is already introduced in the fabrication section 4.2.4. A picture of the CNT part of the sample can be seen in Fig. 4.5 (a). The Pd drain lead is grounded and the Ti/Nb source lead is connected to a stub tuner. There is a wide bottom gate below a silicon nitride layer. Fig. 4.5 (b) and (c) show the suppressed conductance of this device when the bias window lies inside the superconducting gap and the closing of the gap with magnetic field, respectively. In this section, we are discussing

some more data from this sample, especially focusing on states inside the superconducting gap. The attached stub tuner was not matched well enough to the high resistances in the gap. Therefore, we only present DC measurements, meant as a brief outlook.

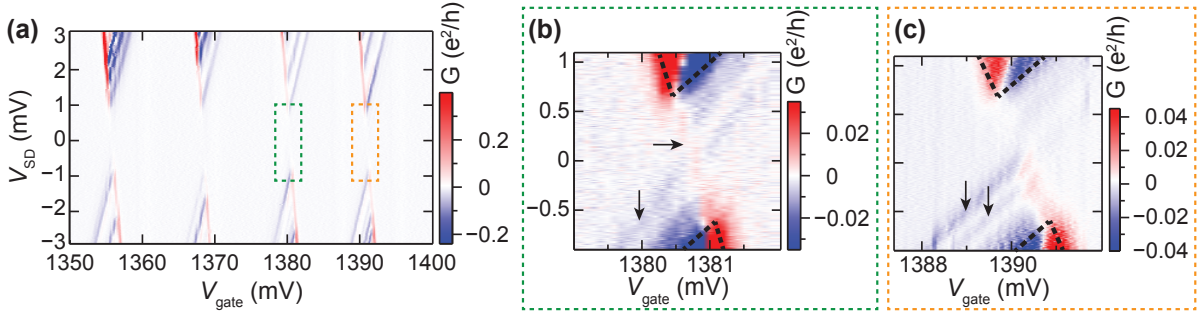


Figure 6.12.: DC measurements of the device shown in Fig. 4.5 (a) at a base temperature of 20 mK. The CNT has one superconducting niobium contact and one normal lead. A single QD is formed and tuned by the wide gate beneath. (a) Differential conductance as a function of gate voltage (V_{gate}) and of source-drain voltage (V_{SD}). (b) and (c) Close-up views of the conductance inside the superconducting gap for two neighbouring resonances marked with rectangles in (a). The Coulomb blockade diamond edges are indicated with black dashes lines.

The overview map of Fig. 6.12 (a) shows clear Coulomb blockade diamonds. The conductance triangles are not touching as an effect of the gapped density of states (DOS) of the superconducting source. It is known that the superconducting lead with its peaked DOS enhances the resolution of spectroscopic features [89, 90]. Indeed, Figs. 4.5 (b) and (c) prove that the clearly visible excited state lines fade away when the superconductivity is suppressed with a magnetic field.

Note that all blue lines in Fig. 6.12 (a) correspond to a negative differential conductance. This is another manifestation of the peaked DOS in the superconducting lead. According to Fermi's golden rule, the tunnel current is proportional the DOS and is peaked whenever a QD level is resonant with the superconducting lead [91]. This translates into a peak-dip structure of the differential conductance.

Figs. 6.12 (b) and (c) show two enlarged conductance maps for low bias voltages. Surprisingly, resonance lines are visible in the gap parallel to the diamond boundary lines. Their conductance is one order of magnitude lower than the conductance on the lines outside the gap. Especially in Fig. 6.12 (b), one line with a negative slope connecting the two triangle corners is visible (marked with the horizontal arrow). The existence of this line is a hint for quasiparticles in the gap, possibly due to imperfections in the RF setup, as explained in section 5.4. In contrast, the lines with a positive slope (marked with vertical arrows) indicate the presence of distinct subgap states. Their energy spacing of about $300 \mu\text{eV}$ is smaller than the spacing between the excited states of approximately $500 \mu\text{eV}$. A plausible origin of these subgap lines are resonant and inelastic Andreev tunnelling events, which are recently observed in our group with similar devices [38].

Unfortunately, the matching of the stub tuner for the low conductances inside the gap was too poor to get enough signal for noise detection. It would be interesting to investigate in future experiments the noise emitted on these subgap lines. Shot noise could confirm the

Cooper-pair nature of the charge carriers involved in the Andreev tunnelling processes inside the gap. Cooper-pairs have twice the charge of a single electron and hence the shot noise of Cooper-pair tunnelling events is doubled, too (see section 7.1.2).

6.5. Reflectometry on a Carbon Nanotube Double Dot

With the help of bottom gates, two QDs in series can be defined along a semiconducting CNT, as shown in Fig. 6.8(d). Detailed reflection experiments on such a double dot system with a stub tuner attached to one lead were carried out in our group by Vishal Ranjan [31]. The studied sample is very similar to the one shown in Fig. 6.7(a). The main difference is that the CNT is suspended between the leads, which is achieved by fork stamping of a CNT on a pre-fabricated lead and bottom gate structure. In the following, some results from this double dot sample are briefly discussed. The sample fabrication and the measurements are done by Vishal Ranjan. The author of this thesis built parts of the measurements setup and contributed to the development of the stub tuner fabrication recipe.

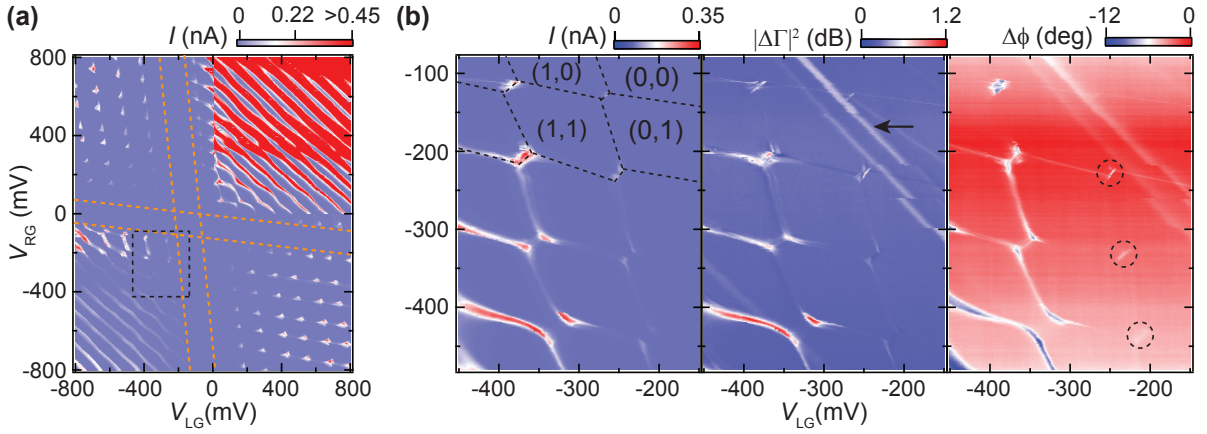


Figure 6.13.: (a) Charge stability diagram over a large voltage range of the left gate (V_{LG}) and right gate (V_{RG}). This colourmap shows the DC current measured at a bias of 10 mV. (b) Simultaneous measurements of the DC current as well as the reflection amplitude and phase at resonance probed with an RF power of -110 dBm. The corresponding gate range is marked by the rectangle in (a). The arrow points at spurious gate-tunable lines. Circles mark inter-dot tunnelling lines visible by a phase shift. (Reprinted with permission from [31]. © 2015 by Nature Publishing Group.)

For the start, we look at the charge stability diagram in Fig. 6.13(a). It shows the DC current at a bias voltage of 10 mV. The cross-like region of zero current (marked by orange dashed lines) arises because the bias window is in the bandgap of this semiconducting CNT in a segment above one of the gates. The high currents in the upper right region suggest that the leads are n -doped.

Fig. 6.13(b) concentrates on the p - p double dot regime inside the dashed rectangle in panel (a). While the left panel shows the DC current, the remaining panels show the amplitude (middle) and phase (right) of the reflected signal at the resonance frequency of the stub tuner, which is close to 3 GHz. The characteristic honeycomb structure of a double dot, which is

introduced in section 6.2.3 [see Fig. 6.6 (b)], is visible in all measurements. The lines with negative slopes are well visible in all plots and arise when one dot is resonant with its lead, while charge transfer through the other dot happens via cotunnelling. But the interesting part is best visible in the phase plot on the very right. The encircled short lines mark the positions where inter-dot tunnelling events happen. As stated at the end of section 6.2.3, these transitions do not lead to a current from one the the other lead, but they cause a change of the susceptance, to which RF measurements are sensitive.

In the RF plots, some additional gate-tunable spurious lines appear, which are marked by an arrow. Most probably, they stem from charging and discharging of a lead state, which does not contribute to a net current, but changes the susceptance.

7 Noise Measurements with Stub Impedance Matching

In this last chapter, we come to the key experimental results of the thesis. Shot noise emitted by a quantum dot (QD) is measured with the help of a stub tuner. But the chapter starts with an introduction to noise and different sources of electronic noise. The second part focuses on noise measurement techniques; the general overview is followed by a more detailed discussion of our method using a stub tuner. In the end, results in the single QD regime are presented and analysed.

7.1. Noise Characteristics

Noise in general is the random fluctuation of an observable in time. In the context of electronics, noise usually denotes stochastic current or voltage fluctuations [82].

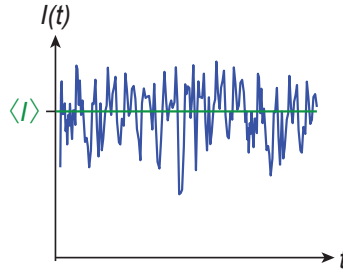


Figure 7.1.: Example of a current fluctuating in time around its mean $\langle I \rangle$.

A typical current signal measured over time is plotted in Fig. 7.1. When talking about current, one usually means more specifically the mean current $\langle I \rangle$. The temporal current fluctuations around its average value are denoted by

$$\Delta I(t) = I(t) - \langle I \rangle. \quad (7.1)$$

To characterise noise, the current-current correlator or autocorrelation function is defined as

$$C(\tau) = \langle \Delta I(t) \Delta I(t + \tau) \rangle, \quad (7.2)$$

where $\langle \cdot \rangle$ denotes an average over time t . The properties of this function are as follows: At time delay $\tau = 0$, it is identical to the mean current fluctuation amplitude squared,

$$C(0) = \langle \Delta I^2(t) \rangle > 0. \quad (7.3)$$

In the other limit of large time delay, the correlation function diverges to zero:

$$\lim_{\tau \rightarrow \pm\infty} C(\tau) = 0. \quad (7.4)$$

That describes the fact that current fluctuations at a certain instant are totally uncorrelated to fluctuations far back in the past (or far in the future).

The Fourier transform of the correlation function is

$$\tilde{S}_I(\omega) = \int_{-\infty}^{\infty} C(\tau) e^{-i\omega\tau} d\tau. \quad (7.5)$$

According to the definition of the Fourier transform, the frequency ω goes from $-\infty$ to ∞ . But experimentally, it is not clear at first sight what a negative frequency means and in most cases, one cannot distinguish positive from negative frequencies. More on this is found in section 7.1.5. Moreover, in the low-frequency classical limit ($\hbar\omega < k_B T$, eV), one finds that $\tilde{S}_I(-\omega) = \tilde{S}_I(\omega)$. Therefore, the current noise spectral density is usually defined as

$$S_I(\omega) = \tilde{S}_I(\omega) + \tilde{S}_I(-\omega) = 2 \cdot \int_{-\infty}^{\infty} C(\tau) e^{-i\omega\tau} d\tau. \quad (7.6)$$

The unit of the current noise (spectral density) is $[\text{A}^2/\text{Hz}]$.

Often, the decay of the correlation function is approximately exponential and described by

$$C(\tau) = C(0) \cdot e^{-\tau/\tau_c}, \quad (7.7)$$

with τ_c being the characteristic decay constant. In this case, the spectral density is

$$S_I(\omega) = 2 \cdot \int_{-\infty}^{\infty} C(0) e^{-\tau/\tau_c} e^{-i\omega\tau} d\tau = \frac{4\tau_c \langle \Delta I^2(t) \rangle}{1 + (\omega\tau_c)^2}, \quad (7.8)$$

according to Eqs. (7.3) and (7.6). Hence, the spectral density at low frequencies ($\omega \ll 1/\tau_c$) is constant. Noise with a frequency-independent spectral density is also called white noise.

There are several physical processes which lead to electronic noise. The two most important noise sources for our experiments and their characteristics are briefly introduced in the following.

7.1.1. Thermal Noise

One contribution to noise is caused by the thermal motion of charge carriers. It is called thermal noise or Johnson-Nyquist noise. The sketch in Fig. 7.2 (a) shows a conductor of conductance G at a finite temperature T . The electron's thermal motion leads to a current I^- to the left and I^+ to the right side. On average, the currents in both directions are equal and there is no net current. But at some instances, there can be more electrons moving in one direction than in the other. The resulting current fluctuations are an equilibrium phenomenon also appearing when no bias is applied. Thermal noise is inherent to every conductor and arises as soon as both ends of a conductor are connected.

The formula for the thermal noise current spectral density reads [92]

$$S_I(\omega) = 4G\hbar\omega \cdot \left(\frac{1}{e^{\hbar\omega/k_B T} - 1} + \frac{1}{2} \right) = \begin{cases} 4k_B T G & \text{if } k_B T \gg \hbar\omega \\ 2\hbar\omega G & \text{if } k_B T \ll \hbar\omega \end{cases}. \quad (7.9)$$

In the low-frequency limit, it describes a white noise spectrum. The contribution in the high-frequency limit stems from zero-point fluctuations, as further described in section 7.1.5.

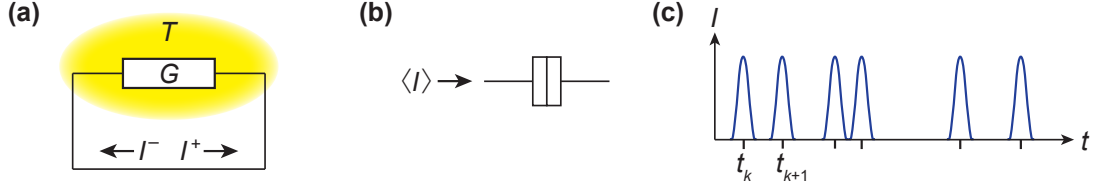


Figure 7.2.: (a) Graphics showing a conductor of conductance G in thermal equilibrium with its environment of temperature T . The two ends are connected by an ideal conductor. The electron's thermal motion causes currents I^+ and I^- moving in the two directions. (b) Schematic of a tunnel junction, through which an average current $\langle I \rangle$ is flowing. (c) The current through such a junction consists of a series of random charge pulses.

7.1.2. Shot Noise

Shot noise arises from the quantised nature of charge carriers, which are moving in an uncorrelated, random manner. In contrast to thermal noise, shot noise only appears when the system is driven out of equilibrium. Shot noise is a phenomenon observed only in mesoscopic conductors, not in macroscopic ones, which can be thought of consisting of many independently fluctuating domains. If the number of these noisy domains is large, the net shot noise cancels to zero.

As an example, we consider a tunnel junction with an average tunnelling current $\langle I \rangle$, as depicted in Fig. 7.2 (b). In the case of high tunnel barriers, one can assume completely uncorrelated tunnelling events. Hence, the time-resolved current consists of random pulses, as represented in the schematic of Fig. 7.2 (c). Each pulse carries the charge e . This is described by

$$I(t) = \sum_k e \delta(t - t_k). \quad (7.10)$$

With the use of Eqs. (7.1) and (7.2), one finds for the autocorrelation function

$$C(\tau) = e \langle I \rangle \delta(\tau), \quad (7.11)$$

assuming charge pulses at completely random times t_k . Applying Eq. (7.6), the resulting current noise spectral density reads

$$S_I = 2e |\langle I \rangle|, \quad (7.12)$$

which is the formula first obtained by Schottky for current fluctuations in vacuum tubes [4]. The reason for the factor 2 is the summation of the contributions from negative and positive frequencies. In this classical case, Schottky noise has a white spectrum.

The statistics of charge tunnelling is Poissonian and therefore Schottky noise is also called Poissonian noise. The Schottky value of a tunnel junction is conventionally used as a reference for any shot noise S_I . To this end, the Fano factor F is introduced as the ratio

$$F = \frac{S_I}{2e |I|}, \quad (7.13)$$

where $|I|$ is the average current and e the elementary charge. Shot noise with $F > 1$ is called super-Poissonian and with $F < 1$ sub-Poissonian.

The scattering theory of Landauer and Büttiker can be applied to determine the shot noise in a coherent conductor. We assume N modes connecting the source and drain leads with transmission probabilities T_k ($k = 1, 2, \dots, N$). When a source-drain bias V is applied, the shot-noise current spectral density is expressed by [93]

$$S_I = 2e|V| \frac{e^2}{h} \sum_{k=1}^N T_k(1 - T_k). \quad (7.14)$$

Thus, for a ballistic conductor, for which all $T_k = 1$, shot noise is suppressed. This is reasonable because of the absence of randomness in the charge transfer. Every charge arriving at the source is certainly transmitted to the drain and consequently a ballistic conductor does not add any fluctuations. In the other limit when all $T_k = 0$, the shot noise also vanishes, since there is no current at all. The maximum shot noise is coming from a channel with $T_k = 1/2$. This dependence on transmission is confirmed with shot-noise experiments of quantum point contacts [94, 95]. In the limit of one low-transmissive channel with transmission probability $T \ll 1$, the Schottky formula of Eq. (7.12) is recovered by using that the current $|I| = e^2/h \cdot T \cdot |V|$.

The generalised formula for the noise of a tunnel junction at a finite temperature T takes into account thermal and shot noise and reads [96]

$$S_I = 2e|I| \coth\left(\frac{eV}{2k_B T}\right). \quad (7.15)$$

In the limit $eV \ll k_B T$, one can use the approximation $\coth(x) \approx 1/x$ for $x \ll 1$. What follows is the thermal noise formula in the low-frequency case as stated in Eq. (7.9). As soon as $eV \gg k_B T$, the *coth*-term approaches one and the Schottky formula of Eq. (7.12) is valid. In summary, thermal noise dominates when $eV < k_B T$ and shot noise dominates in the other case when $eV > k_B T$. This crossover can be seen in Figs. 7.9 (b)-(d).

There are several mechanisms which may lead to enhanced or suppressed shot noise. On the one hand, shot noise is proportional to the effective charge of one charge carrier. For example, super-Poissonian noise has been reported when Cooper pairs are involved [5, 97, 98] and sub-Poissonian noise has been observed for Laughlin quasiparticles in the fractional quantum Hall regime [6, 7, 99]. On the other hand, interactions between the charge carriers, such as the Coulomb interaction or the Pauli exclusion principle, lead to reduced shot noise, since correlations reduce the randomness in the charge transfer [1]. In summary, current fluctuations due to shot noise depend on the kind of charge carriers and the interactions they experience in the studied system. This points out that shot-noise studies can deliver information beyond what is accessible by the average current [2].

7.1.3. Shot Noise in Different Wire Regimes

The Fano factor of a wire is a matter of its length relative to the characteristic length scales of electron motion. As drawn in Fig. 7.3 (a), there are four regimes [100]. When the wire length L is shorter than the mean free path, it is in the ballistic regime. This case has already been discussed in connection with Eq. (7.14) derived by the Landauer-Büttiker formalism. Due to the absence of randomness in charge transport, there is no shot noise.

In the phase-coherent regime, the wire is longer than the mean free path but still shorter than the inelastic electron-electron scattering length ($l_e < L < l_{e-e}$). A phase-coherent wire exhibits

a Fano factor $F = 1/3$, as predicted theoretically [101–103] and confirmed experimentally [104]. For a derivation with the Landauer-Büttiker formula of Eq. (7.14), the phase-coherent wire can be described as consisting of many parallel channels, whose transmission coefficients are binomially distributed [101].

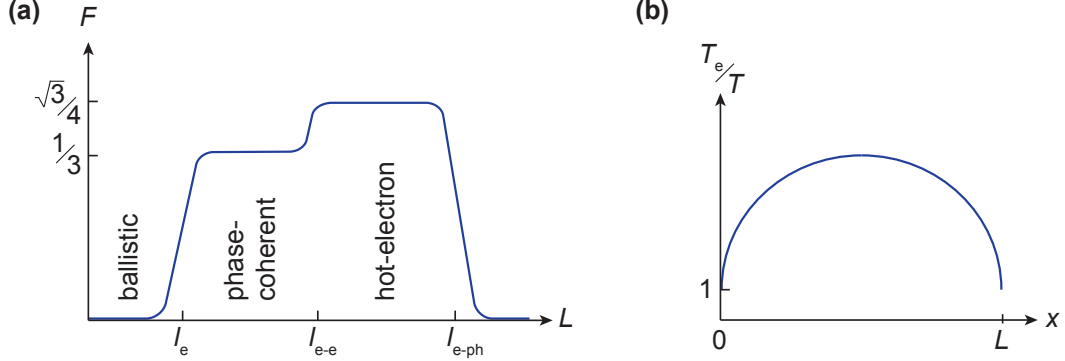


Figure 7.3.: (a) Fano factors for different wire lengths L . The characteristic length scales of the conduction electrons are the mean free path l_e , the electron-electron scattering length l_{e-e} and the electron-phonon scattering length l_{e-ph} . (b) Sketch of the electron temperature T_e along the wire axis x for a wire in the hot-electron regime. T_e is plotted relative to the reservoir temperature T .

The hot-electron regime appears when the wire length is between the electron-electron scattering length l_{e-e} and the electron-phonon scattering length l_{e-ph} . When a bias is applied to the wire, the electrons accelerated through the wire lose part of their kinetic energy via electron-electron scattering, which leads to an increased electron temperature T_e compared to the temperature T of the two reservoirs. Cooling of the wire occurs by diffusion of hot electrons to the reservoirs. The electron temperature profile along the wire axis x as derived in reference [105] is sketched in Fig. 7.3 (b). The temperature of these heated electrons increases with bias and so thus their thermal noise. The resulting Fano factor is $F = \sqrt{3}/4$ in the limit $eV_{\text{bias}} \gg k_B T$ [105–107].

In wires which are longer than the electron-phonon scattering length l_{e-ph} , hot electrons are cooled via phonons and hence the shot noise is reduced until it vanishes in the macroscopic limit. In this limit, the wire can be considered to consist of many individually fluctuating domains. When summing up all the shot-noise contributions, it averages to zero due to the uncorrelated nature of the fluctuations.

7.1.4. Other Noise Sources

Apart from shot noise and thermal noise discussed before, there are two other noise sources in mesoscopic systems, both appearing in a nonequilibrium situation. The characteristic of random telegraph noise is a random current switching between discrete states. The origin of these switches is commonly attributed to charging and discharging of charge traps near the current path.

Flicker or $1/f$ noise is present in almost all electronic devices. As the name suggests, its power spectral density is $1/f$ -dependent. Typically, this noise source dominates at frequencies below about 10 kHz. There are several studies proposing different mechanisms for $1/f$ noise

and the origin is still on debate [108]. Due to the great variability of systems in which these fluctuations occur, no universal mechanism is found.

7.1.5. Quantum Noise

So far, we have dealt with noise in the classical regime. Only in the context of thermal noise [Eq. (7.9)], the high-frequency regime was mentioned. In this section, we are going to take a closer look at the so-called quantum regime, when $hf \gg eV, k_B T$. In a quantum-mechanical treatment, the current in Eq. (7.1) is replaced by the current operator and the square bracket in Eq. (7.2) becomes the quantum statistical average. Since operators do not commute at different times, the autocorrelation function is now a complex value. Consequently, the noise spectral density of Eq. (7.5) is different for negative and positive frequencies: $\tilde{S}_I(-\omega) \neq \tilde{S}_I(\omega)$ [109].

A physical interpretation for the asymmetry of $\tilde{S}_I(\omega)$ in the quantum regime is given in the review [110] and measurements showing this asymmetry are found in [111]. The negative part $\tilde{S}_I(-\omega)$ is a measure of the noisy system's ability to emit photons to the environment. At zero temperature, the system is in the ground state and does not emit any photons and thus $\tilde{S}_I(-\omega) = 0$. The positive part $\tilde{S}_I(\omega)$ is a measure of the system's ability to absorb photons from the environment. This spectral part does not vanish even at zero temperature. Because of zero-point fluctuations in the environment, there is always the chance for absorption.

Often, exciting phenomenon are observed when being in the quantum regime. This is for once not true for noise measurements. Quantum noise is dominated by zero-point fluctuations [112] and does not yield more informations than conductance. Therefore, we do not want to work at too high frequencies.

7.2. Noise Detection Techniques

This section gives an overview of the existing measurement schemes used to detect noise. It will help to put our approach using a stub impedance-matching circuit into a wider context.

7.2.1. Low-Frequency Cross-Correlation

A straightforward, simple way of measuring noise is sketched in Fig. 7.4(a). Noise generated by the device with resistance R can be modelled as a voltage source ΔV_R in series. These voltage fluctuations are amplified and frequency-resolved measurements of the average squared fluctuations $\langle \Delta V^2 \rangle$ can be done using a spectrum analyser. A disadvantage of this method is that it also measures noise added by the amplifier. This noise is modelled as a voltage noise source $\langle \Delta V_A^2 \rangle$ and a current noise source $\langle \Delta I_A^2 \rangle$ referred to the input of an ideal noise-free amplifier, as drawn in the figure. Taking these amplifier noise sources into account, the total voltage fluctuations measured by the spectrum analyser are

$$\langle \Delta V^2 \rangle = g \left(\langle \Delta V_R^2 \rangle + \langle \Delta V_A^2 \rangle + R^2 \langle \Delta I_A^2 \rangle \right), \quad (7.16)$$

where g is the amplifier's power gain. Today's commercial cryogenic HEMT amplifiers have an equivalent noise temperature of at least 4 K or more. This amplifier contribution is often much larger than the noise signal one is actually interested in. Recently developed parametric amplifiers [20, 21] reach a much lower noise level of about 300 mK at $f = 7$ GHz, which is comparable to the vacuum noise level $hf/2k_B$.

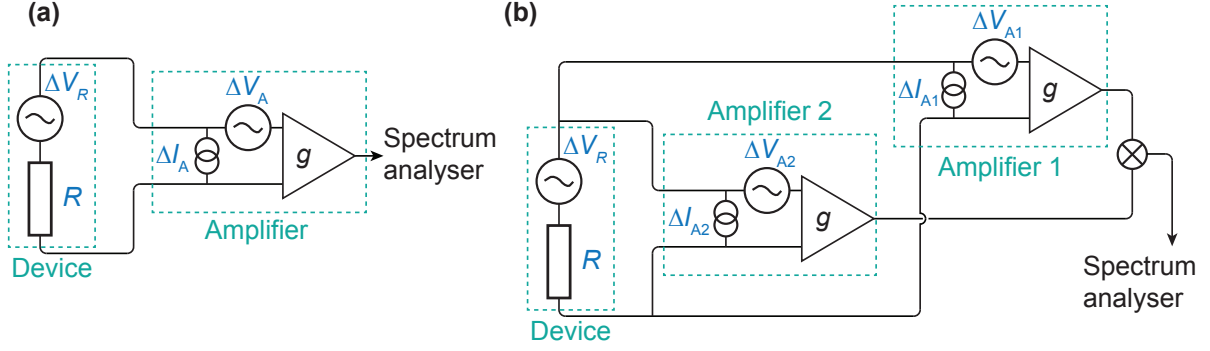


Figure 7.4.: (a) Simple noise measurement setup. Voltage fluctuations from the device (ΔV_R) are amplified and recorded with a spectrum analyser, which itself adds some voltage noise ΔV_A and current noise ΔI_A . (b) Cross-correlation scheme with two independent amplifiers. The amplifier voltage noise contributions are eliminated in the mixed signal, which is fed into a spectrum analyser.

A smart method to get rid of the amplifier noise is the cross-correlation scheme [113], of which a schematic is shown in Fig. 7.4 (b) and which looks similar to a four-terminal measurements scheme for conductance. It uses two independent amplifiers, adding uncorrelated noise contributions. The two amplified noise signals are multiplied with a mixer and then fed into the spectrum analyser. After mixing, the remaining averaged signal is

$$\langle \Delta V_1 \Delta V_2 \rangle = g \left(\langle \Delta V_R^2 \rangle + R^2 \langle \Delta I_{A1}^2 \rangle + R^2 \langle \Delta I_{A2}^2 \rangle \right), \quad (7.17)$$

with ΔV_1 and ΔV_2 denoting the voltage fluctuations at the output of the two amplifiers. The uncorrelated amplifier voltage fluctuations drop out and only the correlated device noise remains plus a contribution from the amplifier current noise, which goes through both amplifiers and is therefore correlated.

The combination of the device resistance R with the wire and filter capacitance C produces an RC low-pass filter in this kind of circuits. When dealing with high-resistance samples with resistances in the range of 100 k Ω , the RC -time limit sets an upper frequency bound of some kilohertz [see Eq. (6.15)]. However, the amplifier noise power has a $1/f$ behaviour, as explained in section 7.1.4. Therefore, it would be desirable to measure at higher frequencies.

7.2.2. Resonant Circuit for Intermediate Frequencies

One way to push up the measurement frequency is to use a resonant circuit [7, 114], to which impedance-matching circuits belong, too. Fig. 7.5 shows a schematic of such a noise measurement scheme including an impedance-matching part between the device and the amplifier. The matching circuit acts as a bandpass filter and provides a window of high noise transmission around the resonance frequency. Impedance matching and the cross-correlation technique are combined in reference [115].

Noise detection with impedance matching is also our approach. The stub tuner as a gigahertz resonant circuit and its transmission properties are introduced in section 3.1.7. An alternative with an LC matching circuit is mentioned in section 3.2. The narrowness of these resonant circuit's high transmission windows might seem to be a disadvantage at first sight. But the

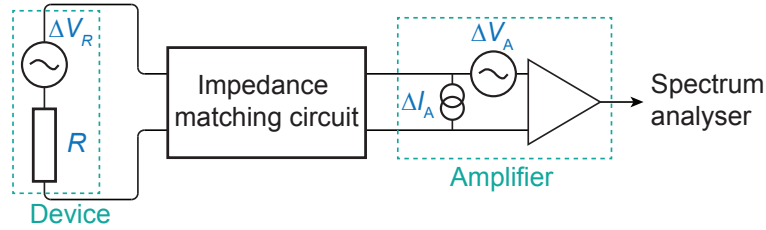


Figure 7.5.: Noise measurements with the help of a resonant impedance-matching circuit. Voltages fluctuations from the device (ΔV_R) are fed into the resonant circuit, amplified and then detected with a spectrum analyser. The amplifier adds input-referred voltage noise ΔV_A and current noise ΔI_A .

analysis in section 3.1.8 proves the opposite. The introduced figure of merit compares the desired noise signal with the unwanted background noise. In this regard, a resonant circuit is very beneficial, since the picked-up background noise remains small when integrating over a narrow frequency band, whereas the transmitted noise signal is large.

7.2.3. High-Frequency Schemes Using Rectifying Elements

There are several techniques suited for high-frequency noise detection. Their common feature is a rectifying element to convert high-frequency radiation to a DC signal.

One possibility is the use of a diode [94], as sketched in Fig. 7.6 (a). For low noise powers, the diode is a square-law detector, meaning that the DC voltage measured after the diode is proportional to the square of the voltage fluctuations: $V_D \propto \langle \Delta V^2 \rangle$. In order to reduce the amount of detected amplifier noise, one can apply a lock-in technique. The device bias is modulated at a low frequency and the rectified voltage is fed into a lock-in amplifier.

A superconductor-insulator-superconductor (SIS) junction can be used for radiation detection, as well [111, 116, 117]. The quasiparticle density of states of the two superconducting junction parts are sketched in Fig. 7.6 (b). The noise source is capacitively coupled to the SIS junction. Radiation on the junction with frequencies $f > (2\Delta - eV_{\text{SIS}})/h$ induce photon-assisted tunnelling events, which are recorded as a DC current. Here, Δ is the superconducting gap and V_{SIS} is the junction bias. The SIS detector is only sensitive to the noise emission spectrum of the source device $[\tilde{S}(-\omega)]$ in the sketched situation when $eV_{\text{SIS}} < 2\Delta$. At a larger bias, the junction is not noiseless any more, which in turn provides photons to be absorbed by the source device. These absorption events lead to a reduced tunnelling current across the junction. In principle, the SIS junction can be used in this configuration as a detector for the absorption spectrum $\tilde{S}(\omega)$. But since the current reduction occurs on top of a large tunnelling current, it is difficult to measure [109].

Also a single quantum dot (QD) can be utilised as a noise detector, when it is capacitively coupled to a nearby noise source [118]. The detection principle can be understood with the help of Fig. 7.6 (c). The configuration in this energy level diagram is such that the charge on the dot is fixed in the absence of radiation. But an impinging photon with a frequency above a certain threshold can excite the electron from the QD ground state to a lead. If an excited state is in the bias window, this photo-ionisation event takes the QD out of Coulomb blockade and a transient sequential tunnelling current is flowing as long as the ground state is not occupied again. This noise detection scheme is only sensitive to the emission spectrum of

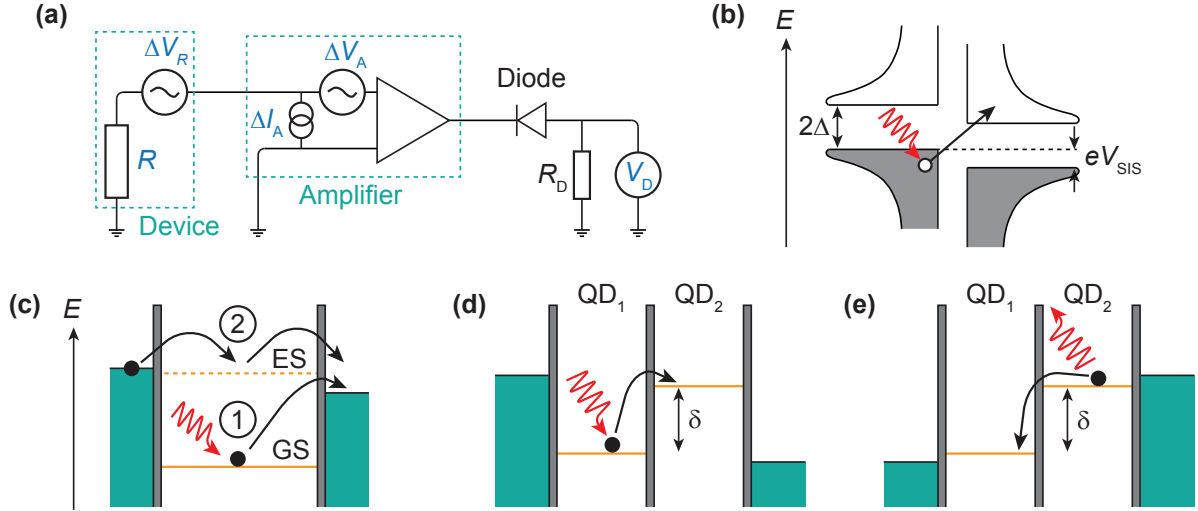


Figure 7.6.: (a) Detection scheme with a diode. The voltage fluctuations of the device ΔV_R and the amplifier fluctuations ΔV_A and ΔI_A are fed into a diode. The rectified voltage V_D is proportional to the noise power. (b) Superconductor-insulator-superconductor (SIS) junction as a radiation detector. The quasiparticle density of states (horizontal axis) of both superconductors is sketched. Electromagnetic radiation generates a photon-assisted quasiparticle tunnelling current for bias voltages $V_{\text{SIS}} < 2\Delta/e$. (c) Radiation detection with a single quantum dot (QD). The energy level diagram illustrates the radiation-induced excitation of an electron from the QD ground state (GS) to the drain lead. This event gives rise to a transient sequential tunnelling current via an excited state (ES), which is in the bias window. (d) Double QD scheme for radiation detection. The energy level diagram shows an electron excited from QD₁ to QD₂ by the absorption of a photon. The electron may leave to the drain, followed by the loading of QD₁ by a source electron. The adjustable detuning δ enables a frequency-selective detection. (e) Double QD configuration with a reversed bias compared to (d), which is sensitive to the emission spectrum of a noise source.

the noise source, denoted by $\tilde{S}(-\omega)$.

On the contrary, a double QD represents a complete quantum spectrum analyser, meaning that it is able to measure separately the absorption and the emission parts of the noise spectrum [119, 120]. As depicted in Fig. 7.6 (d), the double dot is tuned to a stable charge configuration. But the irradiation of photons can induce inelastic tunnelling events: The excited electron on QD₂ may leave to the drain lead and a new electron enters to QD₁ from the source. The frequency of absorbed photons is fixed to $f = \delta/h$ since there are two discrete QD energy levels involved. Here, δ denotes the electrochemical potential difference between the two QD levels. The tunability of δ enables a frequency-selective detection. For a bias as drawn in Fig. 7.6 (d), the double-dot system is sensitive to the emission spectrum $\tilde{S}(-\omega)$ of the source noise. If the bias is reversed, as sketched in Fig. 7.6 (e), the detector is made sensitive to the absorption spectrum $\tilde{S}(\omega)$ since the QD sends out noise that can be absorbed by the studied system.

7.2.4. Full Counting Statistics

An interesting, different approach to obtain noise information starts in the time domain. In reference [121], a QD is capacitively coupled to a nearby quantum point contact (QPC). The QD is the studied noise source and the QPC serves as a charge detector. A change in the number of electrons on the QD modifies the current through the QPC. An example time trace in a regime with fluctuating charge occupation is shown in Fig. 7.7 (a). The QPC current exhibits random telegraph noise - random switching between two or more states due to charging and discharging of the QD. A measurement bandwidth up to 30 – 40 kHz was achieved, which corresponds to a time resolution in the order of 30 μ s.

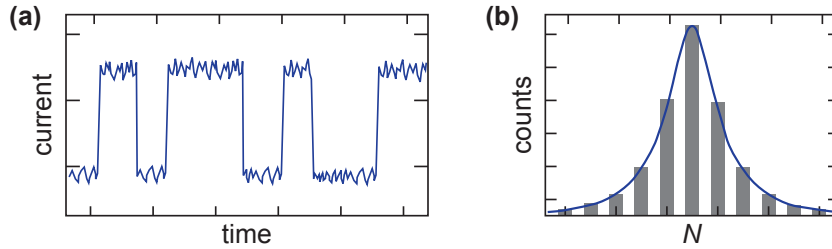


Figure 7.7.: Drawings to explain the principle of full counting statistics (not real measurements). (a) Time trace of the current through a charge detector, which is coupled to a noise source. (b) Histogram for full counting statistics. The time trace is divided in small segments with equal spacings and the number of events happening in each segment is counted.

The acquired time traces can be analysed by means of full counting statistics. For this, the time traces are divided into segments with equal lengths ΔT . The number of switching event in each segment is plotted in a histogram, which may look similar to Fig. 7.7 (b) and contains interesting information [121, 122]. The mean value of the histogram $\langle N \rangle$ is called in statistics the first central moment. It describes the average current through the QD $\langle I \rangle = e\langle N \rangle / \Delta T$. The histogram width is the second central moment or variance $\langle (N - \langle N \rangle)^2 \rangle$, which is related to the current fluctuations via $\langle \Delta I^2 \rangle = e^2 \langle (N - \langle N \rangle)^2 \rangle / \Delta T$. Playing this game further, one can derive even higher central moments from these histograms.

7.3. Noise Detection with a Stub Tuner

The general idea of measuring noise with the help of a resonant circuit is discussed in section 7.2.2 and it is mentioned that the resonant circuit we utilise is the stub tuner. In this section, the properties of such a detection scheme are explained. In particular, it is discussed how to calibrate the circuit.

7.3.1. Setup Analysis

Our entire high-frequency setup is described in chapter 5. The illustration in Fig. 7.8 focuses on the noise measurement chain. We plan the stub tuner's fundamental mode to be around 3 GHz, because it is the centre frequency of the circuit components' bandwidths in our setup (circulator, directional coupler and amplifier). At this frequency, the $1/f$ -noise contribution

is small (see section 7.1.4). At very high frequencies, when $hf \gg eV_{\text{bias}}, k_B T$, one enters the regime of quantum noise (see section 7.1.5). As mentioned earlier, we want to stay in the classical shot-noise regime. Regarding the bias voltage, this is fulfilled as soon as $V_{\text{bias}} > 15 \mu\text{V}$. Assuming a temperature of about 100 mK, 3 GHz is already close to the quantum regime. In summary, we assume the QD sample to emit classical white noise under our measurement conditions.

This white noise signal first passes through the stub tuner. It has a bandpass behaviour with a centre frequency around the matched value and a conductance-dependent bandwidth a few megahertz. The stub tuner parameters are known from reflectometry, as explained in section 6.3.1.

Subsequently, the noise signal is amplified by a low-temperature amplifier and two room-temperature amplifiers with a total gain g . Section 7.3.2 deals about the calibration of g with the help of a reference sample with well-known noise characteristics. The first room-temperature amplifier is matched to the low-temperature amplifier in the sense that its noise is much smaller than the noise of the low-temperature amplifier times the gain. Hence the background noise is effectively stemming from the low-temperature amplifier.

The spectrum analyser detects the noise power dissipated over 50Ω . We record the integrated power spectral density over a certain bandwidth, in which the stub tuner has a high transmission. As found towards the end of section 3.1.8, the optimal bandwidth for the best signal-to-noise ratio is about the full width at half maximum (FWHM) of the transmission function [see Eq. (3.29)].

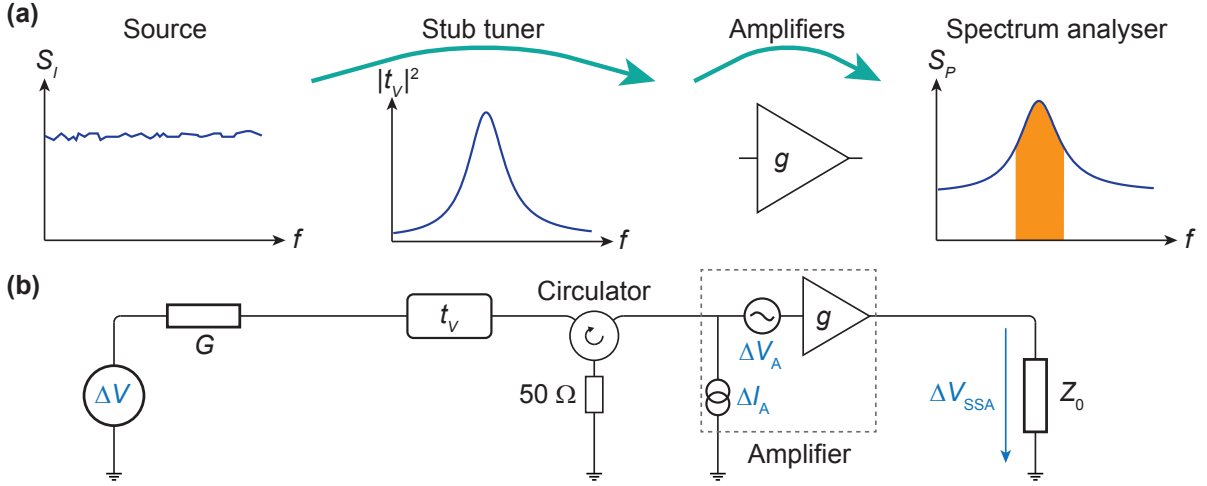


Figure 7.8.: (a) Illustration of the noise detection chain using a stub tuner. The source's white noise passes through the stub tuner with a characteristic voltage transmission function $|t_V|^2$. Then, the signal is amplified with low-temperature and room-temperature amplifiers. In the end, the spectrum analyser measures the power spectral density integrated over a certain bandwidth of high transmission, indicated here in orange. (b) Schematic of this measurement scheme.

After measuring the noise power arriving at the spectrum analyser, the challenge is to extract the part emitted by the device of interest. In order to derive a calibration formula, we look at the measurement chain of Fig. 7.8 in the reversed direction. The integrated noise power measured with the spectrum analyser is denoted by $\langle \Delta P_{\text{SSA}} \rangle$. As a first step, the background

noise $\langle \Delta P_{\text{bg}} \rangle$ added after the stub tuner is subtracted:

$$\langle \Delta P_0 \rangle = \langle \Delta P_{\text{SSA}} \rangle - \langle \Delta P_{\text{bg}} \rangle. \quad (7.18)$$

As discussed later in this section, we take the noise at zero bias as the background value with the assumption that the background noise is independent of the device conductance. This assumption holds for the amplifier voltage noise ΔV_A . But the conversion of the amplifier's current noise ΔI_A to an equivalent voltage noise depends on the impedance seen at the input looking towards the attached circuit in front of the amplifier. In our setup, the circulator between the stub tuner and the amplifier ensures that this impedance is the terminator value of 50Ω , independent of G .

Next, the noise power dissipated on $Z_0 = 50 \Omega$ at the network analyser is converted to voltage fluctuations via

$$\langle \Delta V_0^2 \rangle = Z_0 \cdot \langle \Delta P_0 \rangle. \quad (7.19)$$

Dividing by the amplifier power gain g and the integrated stub transmission function leads to the voltage noise on the device

$$S_V = \frac{\langle \Delta V_0^2 \rangle}{g \cdot \int_{\text{BW}} |t_V|^2 df}, \quad (7.20)$$

where BW is the integration bandwidth. Finally, the conversion from voltage to current noise is done by

$$S_I = S_V \cdot G^2, \quad (7.21)$$

with G being the device differential conductance. Combining Eqs. (7.18) - (7.21) results in the expression

$$S_I = G^2 Z_0 \cdot \frac{\langle \Delta P_{\text{SSA}} \rangle - \langle \Delta P_0 \rangle}{g \cdot \int_{\text{BW}} |t_V|^2 df}, \quad (7.22)$$

which converts the integrated noise power on the spectrum analyser to the current noise spectral density of the device.

7.3.2. Setup Gain Calibration

For the calibration of noise data via Eq. (7.22), it is crucial to know precisely the power gain g of the setup, which is the sum of the three amplifier gains and the cable losses. To this end, the QD sample with the stub tuner is replaced by a metal wire resistor in the hot-electron regime with the well-established Fano factor $F = \sqrt{3}/4 \approx 0.43$ (see section 7.1.3). In this section, it is explained how we infer from the noise data of such a wire the setup gain.

A picture of the studied metal wire is in Fig. 7.9 (a). It is a gold wire of length $L = 50 \mu\text{m}$ on a silicon substrate. Its width $w = 680 \text{ nm}$ and thickness of 30 nm lead to a residual resistance $R = 39 \Omega$ at 4.2 K . This is determined after the noise experiment in a four-terminal measurement. Since we do not observe a resistance decrease between 10 and 4.2 K any more, we assume that 39Ω is the wire resistance at milli-Kelvin temperature, too. It results in a sheet resistance $R_s = R \cdot w/L \approx 0.5 \Omega$. The wire is attached to two rather big copper pads of size $300 \times 300 \mu\text{m}^2$ and thickness 500 nm , acting as heat sinks.

An estimate of the electron-electron scattering length is obtained by Altshuler's formula for a quasi one-dimensional wire [100, 123]:

$$l_{e-e} = \left[\frac{\sqrt{2}}{k_B} \cdot \left(\frac{\hbar}{e} \right)^2 \cdot \frac{Dw}{TR_s} \right]^{1/3}. \quad (7.23)$$

A typical value for the diffusion coefficient D of a gold wire is $120 \text{ cm}^2/\text{s}$ [100]. One ends up with an electron-electron scattering length l_{e-e} of about $20 \text{ }\mu\text{m}$ at 0.1 K .

The electron-phonon scattering length is estimated via

$$l_{e-ph} = \frac{1.31}{\sqrt{T^3\Gamma}}, \quad (7.24)$$

where the electron-phonon coupling parameter Γ is found to be about $5 \cdot 10^9 \text{ m}^{-2}\text{K}^{-3}$ for gold wires [124]. Hence, we expect an electron-phonon scattering length $l_{e-ph} \sim 600 \text{ }\mu\text{m}$. In conclusion, our gold wire is definitely in the hot-electron regime, where $l_{e-e} < L < l_{e-ph}$ [see Fig. 7.3 (a)].

The measurement scheme to detect noise of the gold wire is drawn in Fig. 7.9 (a). A current I is applied to the DC side of the bias tee, whereas noise is measured via the RF side of the bias tee. The wire resistance of $39 \text{ }\Omega$ is close to $Z_0 = 50 \text{ }\Omega$, such that there is a high RF power transmission to the amplifier without impedance matching. A signal and spectrum analyser (SSA) detects the noise power spectral density dissipated over Z_0 and integrates over a bandwidth BW.

But how to extract the noise generated by the wire from the noise power of the SSA? According to Eq. (3.21), the mismatch between the wire resistance and Z_0 is taken into account via the transmission coefficient $t_V = Z_0/(Z_0 + R)$. Assuming no frequency dependence of the gain within the measurement bandwidth, the formula to convert from the integrated noise power at the SSA ($\langle \Delta P_{\text{SSA}} \rangle$) to the shot-noise current density of the wire (S_I) is readily derived from Eq. (7.22) to be

$$S_I = \frac{(Z_0 + R)^2}{Z_0 R^2} \cdot \frac{1}{g} \cdot \frac{\langle \Delta P_{\text{SSA}} \rangle - \langle \Delta P_0 \rangle}{\text{BW}}. \quad (7.25)$$

For the background noise $\langle \Delta P_0 \rangle$, the value at zero current is used, where only thermal noise and amplifier noise is present, but no shot noise.

In order to calibrate the gain which is present for the quantum dot measurements of section 7.4, we measure the noise power at the same centre frequency $f_0 = 2.9218 \text{ GHz}$ and with the same bandwidth of 10 MHz (see section 7.4.2). Since the gain g in Eq. (7.25) is still unknown, the quantity $S_I \cdot g$ is plotted in Fig. 7.9 (b) as a function of the full Schottky noise $2eI$. The flat part close to zero current corresponds to the regime where thermal noise is dominant. At intermediate currents, the shot noise is increasing linearly with current, as indicated with the red lines. A noise reduction is visible for the highest currents, where electrons start to get cooled by phonons. In the linear regime, the shot noise of this wire with hot electrons is expected to exhibit a Fano factor of $\sqrt{3}/4$. Consequently, the slopes a of the two red lines must be $\pm g \cdot \sqrt{3}/4$. Or in other words, one can deduce the gain from the slopes via $g[\text{dB}] = 10 \cdot \log_{10}(|a| \cdot 4/\sqrt{3})$. From the data in the figure, we infer a power gain of 97.9 dB . This is the average from the left and the right side, which both lead to very similar gains. It is a reasonable value considering a gain of about 35 dB from each of the three amplifiers and subtracting a few dB loss from the coaxial cables. Another cross-check is that by using this gain to calibrate the quantum dot data, reasonable Fano factor values are extracted, as explained in connection with Fig. 7.11.

The measurements in Fig. 7.9 (b) are done at the base temperature of 18 mK . The noise evolution with increasing temperatures is shown in Fig. 7.9 (c). It shows the SSA's raw data of integrated noise power. This time, the bandwidth is 500 MHz and the centre frequency 3 GHz .

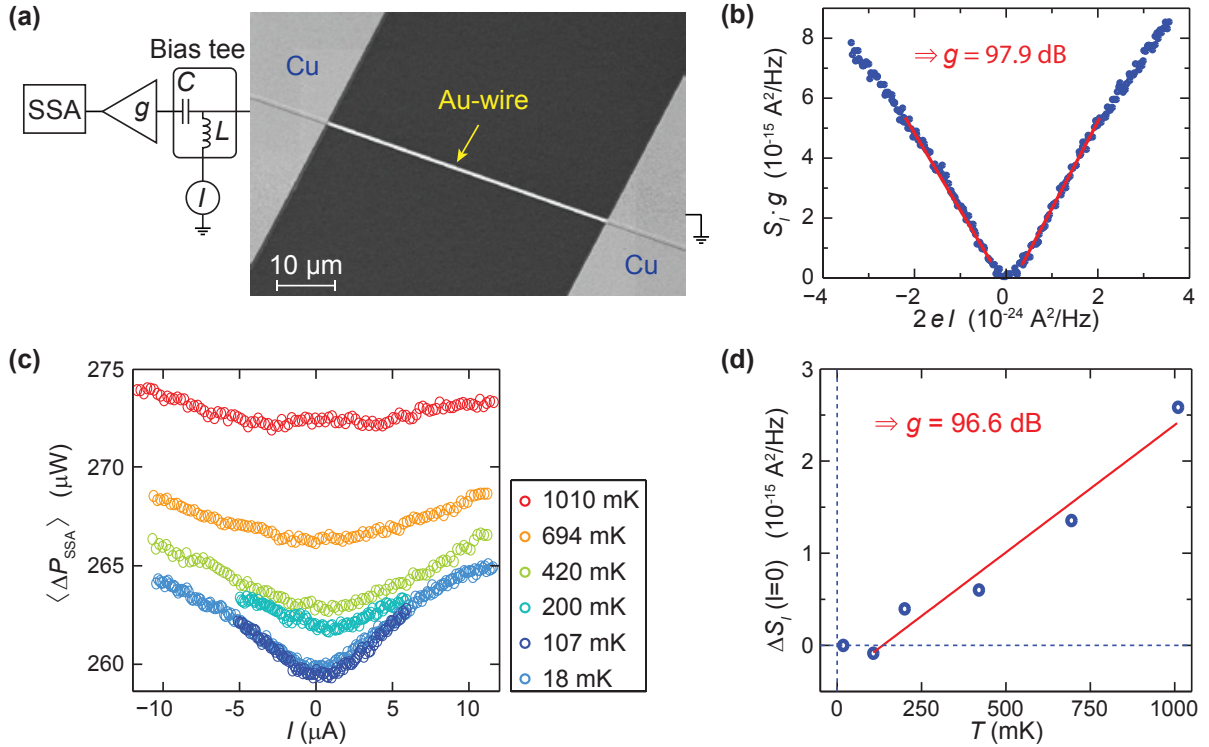


Figure 7.9.: **(a)** Measurement scheme to calibrate the amplifier gain g . The noise source is a $50 \mu\text{m}$ -long gold wire, which is attached to two large copper pads. The noise power is measured at the RF side of the bias tee. The signal is amplified and fed into a signal and spectrum analyser (SSA). At the DC side of the bias tee, a current I is applied. **(b)** Noise data of the wire shown in (a) at the base temperature of 18 mK. The spectrum analyser recorded the integrated noise power over a bandwidth of 10 MHz around the centre frequency of 2.9218 GHz. The plot shows $S_I \cdot g$ as a function of the full Schottky noise $2eI$. From the slopes in the linear regime (marked with red lines), a power gain $g = 97.9 \text{ dB}$ can be extracted. Details on the analysis are in the text. **(c)** Noise power raw data for different temperatures. The integration bandwidth is 500 MHz and the centre frequency 3 GHz. **(d)** Thermal noise increase with temperature, compared to the base temperature value at 18 mK. The current noise density differences are extracted from the minima in panel (c). The thermal noise increase in the linear regime (red line) corresponds to a setup gain $g = 96.6 \text{ dB}$. (Reprinted with permission from [44]. © 2015 by The American Physical Society.)

The effect of an increasing thermal noise for higher temperatures gets apparent in two ways. On the one hand, the flattening around zero current becomes broader and on the other hand the background increases.

To analyse the thermal background in more detail, we can look at Fig. 7.9 (d). It considers the minima at $I = 0$ in panel (c), where there is no shot noise. With the help of Eq. (7.25), $S_I \cdot g$ is calculated without subtracting any background yet ($\langle \Delta P_0 \rangle = 0$). Then, the current noise differences relative to the base temperature value at 18 mK, $\Delta S_I \cdot g$, are plotted as a function

of temperature. The thermal background is only increasing above 100 mK. We conclude that the electron temperature on the RF line is around 100 mK. As discussed in section 5.4, we are currently working on setup improvements to reduce the electron temperature.

At higher temperatures, the thermal noise seems to increase roughly in a linear manner. A linear fit is shown with red lines. Comparing the slope a of the fit with the thermal noise formula $S_I = 4k_B T/R$ [see Eq. (7.9)] yields another way to obtain the setup gain. We deduce a gain $g = aR/(4k_B) \approx 96.6$ dB. It is in the same range than the 97.9 dB extracted before from the shot noise. However, there are not many data points for this linear fit and therefore the gain extracted from thermal noise is not very precise. Furthermore, the bandwidths of the two measurements are very different. In summary, the gain deduced from thermal noise serves as a check if the temperature increase is in a reasonable range, but the gain obtained from shot noise is the accurate value.

7.4. Noise Measurements in the Single Dot Regime

Now, we turn our attention to noise measurements of a single quantum dot (QD) formed in a carbon nanotube (CNT). Owing to the strong electron confinement in QDs, interactions play an important role for charge transport through QDs and one can for instance expect to observe sub-Poissonian shot noise under some circumstances (see section 7.1.2). Thus, QDs are an interesting playground for noise studies. The sample used here is already introduced in chapter, namely in section 6.3. Pictures of the CNT device with an attached stub tuner are shown in Fig. 6.7 and conductance plots in the single QD regime are presented in Fig. 6.10. The noise measurements are done in the exact same gate voltage range than for the conductance plots.

7.4.1. Stub Tuner Transmission

Section 6.3.1 deals with the reflection characteristics of the stub tuner on this sample. Here, the stub tuner parameters from reflection are used to find the transmission properties of this circuit. The general voltage transmission function of a stub tuner is discussed in general in section 3.1.7 and thoroughly derived in appendix B.2.1. Using the parameters obtained from the reflection spectrum in the Coulomb blockade [Fig. 6.9 (a)], Fig. 7.10 (c) shows the calculated transmission functions for three device conductances. They can be compared with the optimal curves in Fig. 3.9 (a) for a lossless circuit at full matching. The conductance $G = 0.26 e^2/h$ corresponds to a resistance of 100 k Ω . While the transmission maximum for this conductance reaches $|t_V|^2 = 1.2 \cdot 10^{-4}$ in the optimal case, our stub tuner has a five times lower maximum of $|t_V|^2 = 2.2 \cdot 10^{-5}$ for the same conductance.

The signal-to-noise ratio (SNR) is a measure of the detection sensitivity. Regarding noise measurements, the SNR is the ratio of desired noise signal to the background noise. In section 3.1.8, the figure of merit g_{SNR} was introduced to quantify the benefit of an impedance-matching circuit for noise detection. It is defined as the ratio of SNRs with and without matching. The maximum figure of merit achieved with a lossless stub tuner at full matching is given by Eq. (3.32) and amounts to $g_{\text{SNR}}^{\text{max}} \approx 400$ for a resistance of 100 k Ω . With the parameters of our actual stub tuner and a detection bandwidth of 10 MHz, Eq. (3.31) yields a ten times lower figure of merit $g_{\text{SNR}} \approx 35$ for $R = 100$ k Ω . Eq. (3.29) suggests a bandwidth slightly larger than the FWHM for a maximal figure of merit. Considering the transmission functions of Fig. 7.10 (a), it gets evident that the chosen bandwidth of 10 MHz is too large. This has two

reasons. Firstly, we were not aware at the time of the measurements that the optimal bandwidth is only the FWHM and secondly, we wanted to make sure that the bandwidth covers the high-transmission windows for all occurring resistances. If we had wisely chosen the bandwidth to be the FWHM, we could have increased the figure of merit for measurements with this stub tuner to $g_{\text{SNR}} \approx 80$ when $R = 100 \text{ k}\Omega$. However, since the FWHM is resistance-dependent and the resistance of typical QD devices changes over more than an order of magnitude, one has always to make a compromise when using a fixed bandwidth.

7.4.2. Noise Calibration

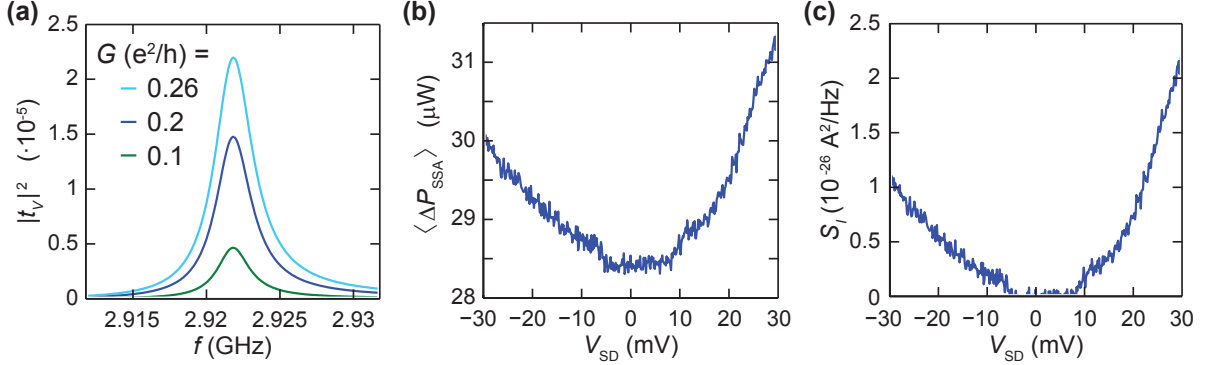


Figure 7.10.: (a) Conductance-dependent voltage transmission function of the stub tuner used for the experiments (using the stub tuner characteristic impedance $Z_0^* = 44.8 \Omega$). The parameters are gained from reflectometry, as explained in Fig. 6.9 (a). (b) Noise power raw data as measured with the spectrum analyser. The integration bandwidth is 10 MHz. The device is a quantum dot and the x -axis is its bias voltage V_{SD} . (c) Eq. (7.22) applied to the data in (a) leads to the current noise spectral density of the quantum dot. The plot corresponds to a vertical cut in Fig. 7.11 (a) at $V_{\text{RG}} = 1330 \text{ mV}$. (Reprinted with permission from [44]. © 2015 by The American Physical Society.)

Section 7.4.3 discusses the complete shot-noise results gained from the QD. But before, the detection settings and the noise calibration method are exemplified here on the basis of data measured at a randomly fixed gate voltage of $V_{\text{RG}} = 1330 \text{ mV}$.

Fig. 7.10 (b) shows the bias dependence of the noise power raw data $\langle \Delta P_{\text{SSA}} \rangle$ obtained from the spectrum analyser when integrating within a window of 10 MHz around the stub tuner resonance. In this frequency window, 1001 points are measured with a bandwidth of 100 kHz, which takes 6 ms to obtain the integrated power. This is repeated for 30 times to calculate an average value. The background noise visible in the flat Coulomb blockade region around zero bias of $\langle \Delta P_0 \rangle \approx 28.5 \mu\text{W}$ is attributed to amplifier noise. The contribution of thermal noise from the QD is negligibly small because the stub tuner transmission is poor at the low conductance inside the blockade.

It is derived in section 7.3.1 how to extract the current noise from the measured noise power. Applying Eq. (7.22) with an amplifier gain of $g = 97.9 \text{ dB}$ (see section 7.3.2) and with the differential conductance values G taken from a preceding reflection measurement (not plotted), results in the current noise spectral density plotted in Fig. 7.10 (c). The resemblance of the

curves in panels (a) and (b) is striking considering the seemingly conductance-dependent transformation formula in Eq. (7.22). This weak conductance dependence can be easily understood in the case of a perfectly matched and lossless stub tuner. For this circuit, the transmission function integral is evaluated in Eq. (3.23) to be $\int_{\text{BW}} |t_V|^2 df \propto G^2$ and hence the G dependence in Eq. (7.22) cancels out.

7.4.3. Shot-Noise Results

After demonstrating how to deduce current noise originating from the QD with the example above, let us now look at the full gate map. Fig. 7.11 (a) shows the calibrated current noise spectral density S_I as a function of gate and bias voltage. For each bias scan, the corresponding noise at zero bias (averaged with four neighbouring values) is used as background noise $\langle \Delta P_0 \rangle$. This way, long-time drifts can be compensated. Because the applied bias voltages are large compared to the thermal energy ($eV_{\text{bias}} \gg k_B T$), the data in this plot is shot noise.

Eq. (7.13) predicts a linear relation between the average current and the shot noise if the Fano factor stays constant. Indeed, the full Schottky noise $2e|I|$ [see Eq. (7.12)] plotted in Fig. 7.11 (b) looks similar to S_I at first sight. The DC current I is measured simultaneously with the noise data. The typical quantity to compare shot noise and mean current is the Fano factor. However, in the context of quantum dots, the Fano factor error bars are diverging inside the Coulomb blockade because one divides by a tiny current. Hence, it is more useful to plot the so-called excess Poissonian noise, as done in Fig. 7.11 (c). $S_I^{\text{EP}} = S_I - 2e|I|$ is the difference between the shot noise and the full Schottky noise. One can distinguish between super-Poissonian noise, where S_I^{EP} is positive (red), and sub-Poissonian noise, where it is negative (blue). The effects on shot noise by three distinct processes are visible and discussed below.

Inside the Coulomb blockade (CB), namely at the corners of the two large diamonds, there are some small areas where the noise is super-Poissonian. We relate this shot-noise enhancement to inelastic cotunnelling events. The argument goes as follows: In the configuration drawn in Fig. 7.12 (a), the current is initially blocked. But an inelastic cotunnelling process leaves the QD in a state, in which sequential tunnelling is possible as long as the ground state is not occupied again, as drawn in Fig. 7.12 (b). In summary, each switching to a conducting state by an inelastic tunnelling event is followed by a bunch of transferred electrons and thus the current consists of pulses with an average charge larger than e . This situation is analogous to what one observes on the street. A red traffic light interrupts the car flow with a slow rate compared to their speed when the light is green. Since shot noise depends linearly on the charge unit, it is enhanced in the inelastic cotunnelling regime [125, 126]. Super-Poissonian noise in this QD regime has already been observed in references [117, 127–129].

Outside the CB, an oscillating shot noise is apparent in Fig. 7.11 (c). More insight is gained in Fig. 7.11 (d), where the Fano factor along the diagonal dotted line in Fig. 7.11 (c) is plotted together with the absolute value of the current. The shot-noise suppression is correlated with steps in the Coulomb staircase. Fano factors $F \approx 1$ are reached at the end of each plateau, as indicated by vertical dashed lines. But after the onset of a new plateau, when the number of electrons on the dot increases by one, the Fano factor is seen to be reduced.

In section 7.1.2, it is shown that a single tunnel junction yields $F = 1$. Transport through a QD happens via two tunnel junctions in series. The corresponding Fano factor depends on the ratio between the two tunnelling rates. In the case of equal rates for entering via the source and leaving to drain, the Fano factor is reduced to $F = 1/2$. This can be understood with the

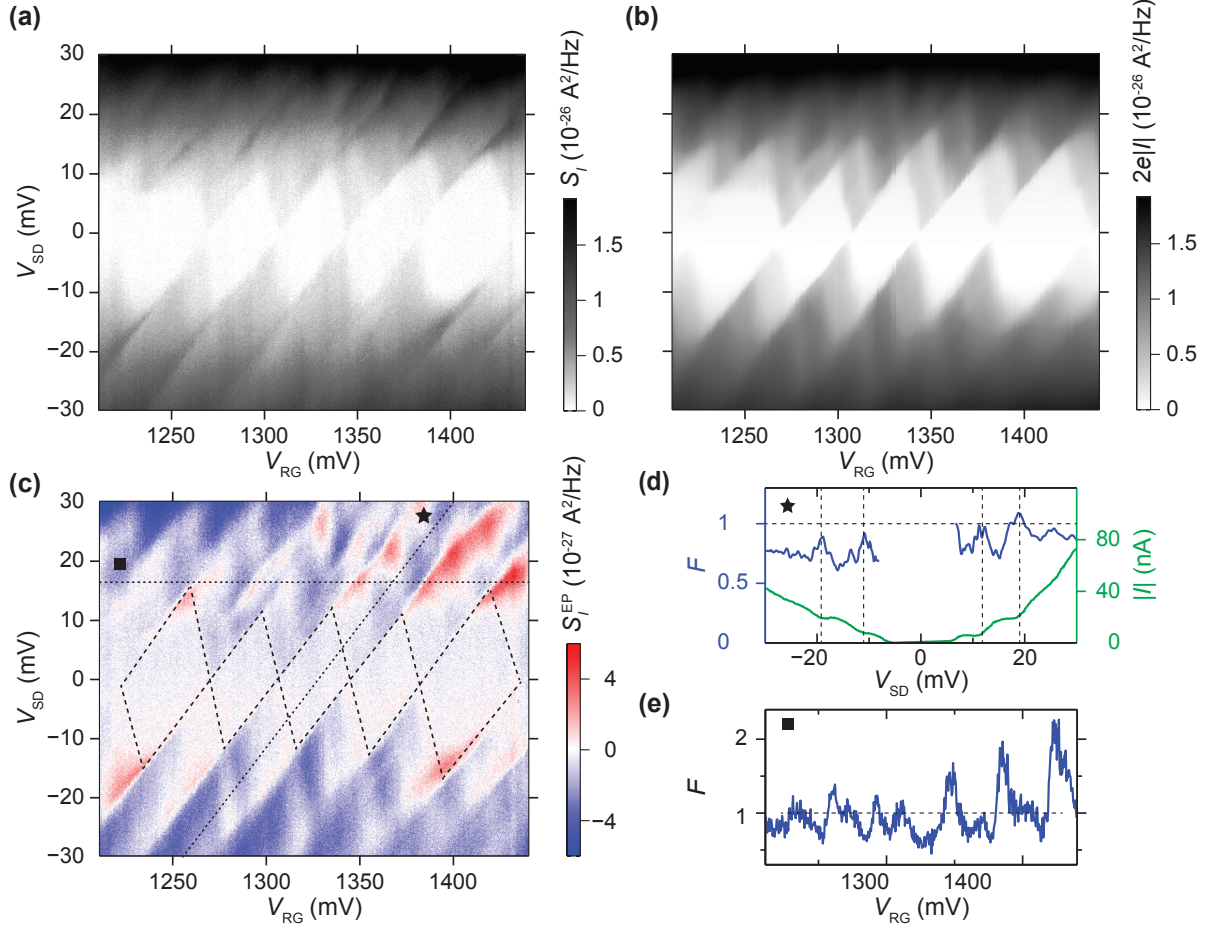


Figure 7.11.: (a) Calibrated shot-noise current spectral density S_I of a quantum dot as a function of voltage on the right gate (V_{RG}) and of source-drain voltage (V_{SD}). (b) Schottky noise $2e|I|$ and (c) excess Poissonian noise $S_I^{EP} = S_I - 2e|I|$, where I is the measured averaged current. The Coulomb blockade diamond contours (dashed lines) are copied from the conductance plot of Fig. 6.10 (a). (d) Fano factors averaged over a range of 1.2 mV in V_{SD} (left scale) and absolute value of current (right scale) along the dotted line in (c) marked with a star. Fano factor peaks correspond to the onset of current transitions from one to the next plateau. (e) Fano factors along the horizontal line in panel (c), which is marked with a square. (Reprinted with permission from [44]. © 2015 by The American Physical Society.)

following argument. Tunnelling of an electron with charge $-e$ into the dot invokes screening at the source and drain side. Because of equal tunnelling rates, the screening charge on source is $+e/2$ and on drain $-e/2$ and therefore the charge flow experienced by the outer circuit due to the tunnelling-in event is $-e/2$. The same is true when an electron tunnels out to drain. The observed current consists of charge pulses of charge $-e/2$ and thus the Fano factor is $F = 0.5$. The situation changes if the tunnelling rates are very different. Then, tunnelling through the weakly coupled junction is immediately followed by tunnelling through the strongly coupled

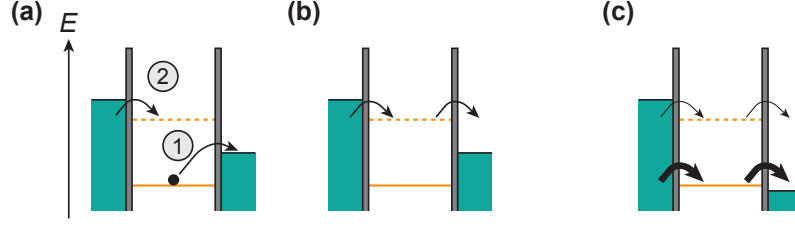


Figure 7.12.: **(a)** Energy level diagram showing an inelastic cotunnelling event. The solid line represents the ground state and the dashed line an excited state. **(b)** After the process in (a), sequential tunnelling is allowed and leads to a transient current. **(c)** Level diagram in the conducting regime with a ground and an excited state inside the bias window. The tunnelling rates for the ground (excited) state are large (small), as represented with thick (thin) arrows. The weakly coupled excited state is blocking transport from time to time, which leads to a shot-noise enhancement.

junction. Thus, the junction with the low rate creates charge pulses of e , which cause a Fano factor of one like for a single junction.

Transport through a QD system can be treated by the so-called orthodox theory. Starting with Fermi's golden rule, one can calculate the tunnelling rates. In the next step, the current is obtained from a rate equation. Reference [130] explains that the observation of a Coulomb staircase with flat plateaus like in Fig. 7.11 (d) is a sign that the tunnelling resistances R_t of the two junctions are quite different. As explained before, a large difference between the tunnelling rates leads to $F = 1$. This is what we observe at the ends of each plateau.

But in between these maxima, the Fano factor is suppressed despite the difference in the tunnelling resistances. According to the orthodox theory, the tunnelling rates Γ are not simply proportional to the tunnelling resistances R_t , but depend on the energy, too. For a complete description of the system with a QD and the attached bias voltage source, one has to consider the Gibb's free energy. It is the QD electrostatic energy minus the work done by the voltage source. The tunnelling rate derived from Fermi's golden rule is [130]

$$\Gamma^\pm(\Delta G^\pm) = \frac{1}{e^2 R_t^\pm} \cdot \frac{\Delta G^\pm}{1 - e^{-\Delta G^\pm/k_B T}}, \quad (7.26)$$

where $+/-$ refers to tunnelling on and off the QD and ΔG^\pm denote the corresponding gains in free energy. At zero temperature, the rates reduce to

$$\Gamma^\pm(\Delta G^\pm) = \begin{cases} 0 & \text{if } \Delta G^\pm \leq 0 \\ \frac{\Delta G^\pm}{e^2 R_t^\pm} & \text{if } \Delta G^\pm > 0 \end{cases}. \quad (7.27)$$

One can see that a difference between R_t^+ and R_t^- , as present in our device, can be compensated by an asymmetry in the energy gain and the tunnelling rates can become equal despite of asymmetric tunnelling resistances. Hence, in this case the whole device behaves as if it is composed of two identical junctions in series with $F = 0.5$ in the ideal case. This behaviour of Γ explains the periodic noise suppression seen in Fig. 7.11 (d) and also reported in references [96, 131, 132]. The above model assumes transport through only one QD state. However, at

finite temperature and/or for larger bias voltages, more than one state is involved, yielding $F > 0.5$. The noise suppression therefore tends to decay away at large bias voltages and approaches $F = 1$ for $eV_{\text{bias}} \gg Ec$. This is exactly what we see in the data.

It is visible in Fig. 7.11 (d) and more pronouncedly in Fig. 7.11 (e) that the Fano factor peak values can exceed one. This finding can only be explained with multi-level models [133–135]. The requirement for super-Poissonian noise is that there are two levels within the bias window with very different tunnelling rates to the leads. Such a situation is sketched in Fig. 7.12 (c), where the tunnelling rates to and from the ground state is much larger than the rates for the excited state. Hence, most of the current goes via the ground state, but once in a while the excited state gets populated and the current is stopped until the excited state is emptied again since the charging energy prevents both states to be occupied at the same time. The result of such a blocking state is bunched charge transport and consequently enhanced shot noise. This is very similar to the process leading to shot-noise enhancement in the inelastic cotunnelling regime as described before, which may explain why the regions of super-Poissonian noise inside and outside the CB are connected [see Fig. 7.11 (c)].

Overall, the observed shot-noise features in the single QD regime agree well with previous experimental studies. We conclude that the presented noise measurement scheme with stub impedance matching and the applied calibration procedure are well suited for noise detection of high-resistance devices.

8 Summary and Outlook

The goal of this thesis was to develop a gigahertz-frequency conductance and noise measurement scheme for high-resistance devices. Owing to the large impedance mismatch between the device with typical resistances up to a megaohm and the standard characteristic impedance $Z_0 = 50 \Omega$ of the measurement line, an impedance-matching circuit is necessary. With such a circuit, one achieves a high RF signal transmission from the 50Ω side to the device and at the same time in the reverse direction from the device towards the 50Ω detection side. The circuit we use here for impedance matching is a so-called stub tuner. Its simple planar structure, consisting of coplanar transmission lines, makes it easy to fabricate and to model. As discussed in section 3.1, its behaviour at gigahertz frequencies can be reliably predicted with a standard circuit model.

Details of the developed fabrication procedure are presented in chapter 4. For minimised losses in the transmission line we use niobium, which is superconducting at our measurement temperatures. Another fabrication aspect to consider is that the impedance transformation should happen as close to the device as possible to reduce signal loss and parasitic effects between the device and the stub tuner. The mesoscopic device investigated in this thesis is a quantum dot formed in a carbon nanotube. We developed a method to fabricate carbon nanotube based devices and a stub tuner on the same chip. In particular, we found a way to stamp carbon nanotubes from the growth substrate to the target substrate in a reliable manner.

The stub tuners we use at the moment have no tunable parameter. The stub tuner formulas in section 3.1 allow to plan the matched resistance and frequency beforehand. But as shown with the resonator measurements in section 2.4.4, the transmission line loss scatters considerably and unpredictably. A tunability could be introduced by attaching a variable impedance to the open stub tuner end, as for example a varactor diode (variable capacitor) [29] or a SQUID, whose inductance can be changed by varying the magnetic flux. With such a variable element, one could tune to perfect impedance matching and adapt to different resistance regimes during the experiment.

In the course of this thesis, we built up an RF measurement setup in a dilution refrigerator, as described in chapter 5. Although there is room for setup improvements (on which we are currently working), we could successfully conduct RF measurements on a quantum dot defined in a carbon nanotube, which is connected to a stub tuner. On the basis of this sample, we demonstrated the application of stub impedance matching for two kinds of RF measurements: reflectometry and noise detection.

Chapter 6 deals with the RF reflection properties of the sample. We show that all relevant stub tuner parameters can be extracted from the reflectance spectrum around the resonance frequency when the quantum dot is in Coulomb blockade. Knowing the stub tuner parameters, the reflection amplitude at the resonance frequency can be converted to the quantum dot's differential conductance. Since the reflection spectrum depends on the complex device

impedance, it is also possible to obtain information about capacitance and inductance changes in the device [31].

While the stub tuner parameters are obtained from reflectance, the gain of the amplification chain needs to be deduced in another way. We replaced the sample with a metal wire in the hot-electron regime, where it generates shot noise with a well-established Fano factor. Section 7.3.2 demonstrates how to deduce the setup gain from the detected shot noise of such a wire.

The main results are the shot-noise measurements in the quantum dot regime, which are presented in section 7.4. With the help of stub impedance matching, we obtained clean noise data in a fast way. The results compare well with earlier studies. In order to quantify the benefit of impedance matching for noise measurements, we introduced the figure of merit g_{SNR} , which is the ratio of the SNR with and without impedance matching. With the stub tuner of the presented sample, a figure of merit $g_{\text{SNR}} \approx 80$ is attainable for a resistance of 100 k Ω , despite a rather lossy circuit and being quite far from full matching. The upper bound for a lossless stub tuner at matching would be as high as $g_{\text{SNR}} \approx 400$ for this resistance.

Recently, we started to work on an alternative impedance-matching circuit based on a planar inductive coil, as briefly mentioned in section 3.2. Its advantage is a much larger bandwidth compared to a stub tuner. Whereas this provides more signal and hence allows for faster measurements, there is no effect on the figure of merit because a larger bandwidth also means picking up more background noise.

The presented measurements can be viewed as proof-of-principle experiments, demonstrating the potential of stub impedance matching for noise detection of high-resistance devices. We gained a profound knowledge of the setup and its calibration. It paves the way for noise studies of unexplored high resistance systems. One example is the quantum dot with one superconducting lead of section 6.4, which showed distinct subgap features. Shot-noise studies in this regime could lead to more insight into the transport mechanisms.

Bibliography

- [1] Y. Blanter and M. Büttiker, *Physics Reports* **336**, 1 (2000).
- [2] C. Beenakker and C. Schönberger, *Physics Today* **56**, 37 (2003).
- [3] A. Einstein, *Phys. Z.* **10**, 185 (1909).
- [4] W. Schottky, *Annalen der Physik* **362**, 541 (1918).
- [5] F. Lefloch, C. Hoffmann, M. Sanquer, and D. Quirion, *Phys. Rev. Lett.* **90**, 067002 (2003).
- [6] L. Saminadayar, D. C. Glattli, Y. Jin, and B. Etienne, *Phys. Rev. Lett.* **79**, 2526 (1997).
- [7] R. de Picciotto, M. Reznikov, M. Heiblum, V. Umansky, G. Bunin, and D. Mahalu, *Nature* **389**, 162 (1997).
- [8] J. B. Johnson, *Phys. Rev.* **32**, 97 (1928).
- [9] H. Nyquist, *Phys. Rev.* **32**, 110 (1928).
- [10] D. Pozar, *Microwave Engineering*, 3rd ed. (John Wiley & Sons Inc., Hoboken, 2005).
- [11] R. Simons, *Coplanar Waveguide Circuits, Components, and Systems* (John Wiley & Sons Inc., New York, 2001).
- [12] G. Ghione and C. Naldi, *Electronics Letters* **20**, 179 (1984).
- [13] S. Gevorgian, *Electronics Letters* **30**, 1236 (1994).
- [14] G. Ghione and C. Naldi, *Electronics Letters* **19**, 734 (1983).
- [15] K. Watanabe, K. Yoshida, T. Aoki, and S. Kohjiro, *Japanese Journal of Applied Physics* **33**, 5708 (1994).
- [16] M. Tinkham, *Introduction to Superconductivity*, 2nd ed., Dover Books on Physics (Dover Publications, 2004).
- [17] P. K. Day, H. G. LeDuc, B. A. Mazin, A. Vayonakis, and J. Zmuidzinas, *Nature* **425**, 817 (2003).
- [18] M. Göppl, A. Fragner, M. Baur, R. Bianchetti, S. Filipp, J. M. Fink, P. J. Leek, G. Puebla, L. Steffen, and A. Wallraff, *Journal of Applied Physics* **104**, 113904 (2008).
- [19] B. A. Mazin, *Microwave Kinetic Inductance Detectors*, Ph.D. thesis, California Institute of Technology (2004).

- [20] M. A. Castellanos-Beltran and K. W. Lehnert, *Applied Physics Letters* **91**, 083509 (2007).
- [21] E. A. Tholén, A. Ergül, E. M. Doherty, F. M. Weber, F. Grégis, and D. B. Haviland, *Applied Physics Letters* **90**, 253509 (2007).
- [22] A. Wallraff, D. I. Schuster, A. Blais, L. Frunzio, R.-S. Huang, J. Majer, S. Kumar, S. M. Girvin, and R. J. Schoelkopf, *Nature* **431**, 162 (2004).
- [23] V. Singh, B. H. Schneider, S. J. Bosman, E. P. J. Merckx, and G. A. Steele, *Applied Physics Letters* **105**, 222601 (2014).
- [24] A. D. O’Connell, M. Ansmann, R. C. Bialczak, M. Hofheinz, N. Katz, E. Lucero, C. McKenney, M. Neeley, H. Wang, E. M. Weig, A. N. Cleland, and J. M. Martinis, *Applied Physics Letters* **92**, 112903 (2008).
- [25] J. Goetz, F. Deppe, M. Haerberlein, F. Wulschner, C. W. Zollitsch, S. Meier, M. Fischer, P. Eder, E. Xie, K. G. Fedorov, E. P. Menzel, A. Marx, and R. Gross, *Journal of Applied Physics* **119**, 015304 (2016).
- [26] A. Bruno, G. de Lange, S. Asaad, K. L. van der Enden, N. K. Langford, and L. DiCarlo, *Applied Physics Letters* **106**, 182601 (2015).
- [27] A. I. Gubin, K. S. Il’in, S. A. Vitusevich, M. Siegel, and N. Klein, *Phys. Rev. B* **72**, 064503 (2005).
- [28] C. Altimiras, O. Parlavecchio, P. Joyez, D. Vion, P. Roche, D. Esteve, and F. Portier, *Applied Physics Letters* **103**, 212601 (2013).
- [29] S. Hellmüller, M. Pikulski, T. Müller, B. Küng, G. Puebla-Hellmann, A. Wallraff, M. Beck, K. Ensslin, and T. Ihn, *Applied Physics Letters* **101**, 042112 (2012).
- [30] G. Puebla-Hellmann and A. Wallraff, *Applied Physics Letters* **101**, 053108 (2012).
- [31] V. Ranjan, G. Puebla-Hellmann, M. Jung, T. Hasler, A. Nunnenkamp, M. Muoth, C. Hierold, A. Wallraff, and C. Schönenberger, *Nat. Commun.* **6**, 7165 (2015).
- [32] J. Wenner, M. Neeley, R. C. Bialczak, M. Lenander, E. Lucero, A. D. O’Connell, D. Sank, H. Wang, M. Weides, A. N. Cleland, and J. M. Martinis, *Superconductor Science and Technology* **24**, 065001 (2011).
- [33] W. W. Xue, B. Davis, F. Pan, J. Stettenheim, T. J. Gilheart, A. J. Rimberg, and Z. Ji, *Applied Physics Letters* **91**, 093511 (2007).
- [34] K. C. Fong and K. C. Schwab, *Phys. Rev. X* **2**, 031006 (2012).
- [35] J. Schindele, A. Baumgartner, and C. Schönenberger, *Phys. Rev. Lett.* **109**, 157002 (2012).
- [36] A. Eichler, R. Deblock, M. Weiss, C. Karrasch, V. Meden, C. Schönenberger, and H. Bouchiat, *Phys. Rev. B* **79**, 161407 (2009).
- [37] A. Eichler, M. Weiss, S. Oberholzer, C. Schönenberger, A. Levy Yeyati, J. C. Cuevas, and A. Martín-Rodero, *Phys. Rev. Lett.* **99**, 126602 (2007).

- [38] J. Gramich, A. Baumgartner, and C. Schönenberger, *Phys. Rev. Lett.* **115**, 216801 (2015).
- [39] B. Babić, J. Furer, M. Iqbal, and C. Schönenberger, *AIP Conference Proceedings* **723**, 574 (2004).
- [40] J. Furer, *Growth of Single-Wall Carbon Nanotubes by Chemical Vapor Deposition for Electrical Devices*, Ph.D. thesis, University of Basel (2006).
- [41] W. Carter and E. Cukauskas, *Magnetics, IEEE Transactions on* **23**, 847 (1987).
- [42] R. A. Gardner, *Journal of Solid State Chemistry* **9**, 336 (1974).
- [43] J. J. Viennot, J. Palomo, and T. Kontos, *Applied Physics Letters* **104**, 113108 (2014).
- [44] T. Hasler, M. Jung, V. Ranjan, G. Puebla-Hellmann, A. Wallraff, and C. Schönenberger, *Phys. Rev. Applied* **4**, 054002 (2015).
- [45] M. Muoth and C. Hierold, *2012 IEEE 26th International Conference on Micro Electro Mechanical Systems (MEMS)*, 1352 (2012).
- [46] J. Waissman, M. Honig, S. Pecker, A. Benyamini, A. Hamo, and S. Ilani, *Nat. Nanotechnol.* **8**, 569 (2013).
- [47] M. Jung, J. Schindele, S. Nau, M. Weiss, A. Baumgartner, and C. Schönenberger, *Nano Letters* **13**, 4522 (2013).
- [48] A. Baumgartner, G. Abulizi, K. Watanabe, T. Taniguchi, J. Gramich, and C. Schönenberger, *Applied Physics Letters* **105**, 023111 (2014).
- [49] J. Samm, J. Gramich, A. Baumgartner, M. Weiss, and C. Schönenberger, *Journal of Applied Physics* **115**, 174309 (2014).
- [50] J. Svensson and E. E. B. Campbell, *Journal of Applied Physics* **110**, 111101 (2011).
- [51] J. O. Schindele, *Observation of Cooper Pair Splitting and Andreev Bound States in Carbon Nanotubes*, Ph.D. thesis, University of Basel (2014).
- [52] W. Mönch, *Reports on Progress in Physics* **53**, 221 (1990).
- [53] F. Léonard and J. Tersoff, *Physical Review Letters* **84**, 4693 (2000).
- [54] W. Zhu and E. Kaxiras, *Applied Physics Letters* **89**, 243107 (2006), 10.1063/1.2405393.
- [55] W. Zhu and E. Kaxiras, *Nano Letters* **6**, 1415 (2006).
- [56] T. Meng, C.-Y. Wang, and S.-Y. Wang, *Journal of Applied Physics* **102**, 013709 (2007).
- [57] J. J. Palacios, P. Tarakeshwar, and D. M. Kim, *Phys. Rev. B* **77**, 113403 (2008).
- [58] V. Vitale, A. Curioni, and W. Andreoni, *Journal of the American Chemical Society* **130**, 5848 (2008).
- [59] A. Javey, J. Guo, Q. Wang, M. Lundstrom, and H. Dai, *Nature* **424**, 654 (2003).

- [60] C. Lu, L. An, Q. Fu, J. Liu, H. Zhang, and J. Murduck, *Applied Physics Letters* **88**, 133501 (2006).
- [61] C. W. J. Beenakker, *Phys. Rev. B* **46**, 12841 (1992).
- [62] A. Braggio, M. Governale, M. G. Pala, and J. König, *Solid State Communications* **151**, 155 (2011).
- [63] J. Schindele, A. Baumgartner, R. Maurand, M. Weiss, and C. Schönenberger, *Phys. Rev. B* **89**, 045422 (2014).
- [64] V. Novotny and P. P. M. Meincke, *Journal of Low Temperature Physics* **18**, 147 (1975).
- [65] J. Gramich, *Andreev and spin transport in carbon nanotube quantum dot hybrid devices*, Ph.D. thesis, University of Basel (2016).
- [66] G. I. Lykken, A. L. Geiger, K. S. Dy, and E. N. Mitchell, *Phys. Rev. B* **4**, 1523 (1971).
- [67] J. Gramich, A. Baumgartner, and C. Schönenberger, *Applied Physics Letters* **108**, 172604 (2016).
- [68] C. P. Scheller, S. Heizmann, K. Bedner, D. Giss, M. Meschke, D. M. Zumbühl, J. D. Zimmerman, and A. C. Gossard, *Applied Physics Letters* **104**, 211106 (2014).
- [69] J. P. Pekola, K. P. Hirvi, J. P. Kauppinen, and M. A. Paalanen, *Phys. Rev. Lett.* **73**, 2903 (1994).
- [70] D. J. Reilly, C. M. Marcus, M. P. Hanson, and A. C. Gossard, *Applied Physics Letters* **91**, 162101 (2007).
- [71] R. Barends, J. Wenner, M. Lenander, Y. Chen, R. C. Bialczak, J. Kelly, E. Lucero, P. O'Malley, M. Mariantoni, D. Sank, H. Wang, T. C. White, Y. Yin, J. Zhao, A. N. Cleland, J. M. Martinis, and J. J. A. Baselmans, *Applied Physics Letters* **99**, 113507 (2011).
- [72] D. F. Santavicca and D. E. Prober, *Measurement Science and Technology* **19**, 087001 (2008).
- [73] L. P. Kouwenhoven, D. G. Austing, and T. S., *Reports on Progress in Physics* **64**, 701 (2001).
- [74] A. Oberlin, M. Endo, and T. Koyama, *Journal of Crystal Growth* **32**, 335 (1976).
- [75] A. Thess, R. Lee, P. Nikolaev, H. Dai, P. Petit, J. Robert, C. Xu, Y. H. Lee, S. G. Kim, A. G. Rinzler, D. T. Colbert, G. E. Scuseria, D. Tománek, J. E. Fischer, and R. E. Smalley, *Science* **273**, 483 (1996).
- [76] R. Saito, G. Dresselhaus, and M. S. Dresselhaus, *Physical Properties of Carbon Nanotubes* (Imperial College Press, 1998).
- [77] A. H. Castro Neto, F. Guinea, N. M. R. Peres, K. S. Novoselov, and A. K. Geim, *Rev. Mod. Phys.* **81**, 109 (2009).

- [78] E. A. Laird, F. Kuemmeth, G. A. Steele, K. Grove-Rasmussen, J. Nygård, K. Flensberg, and L. P. Kouwenhoven, *Rev. Mod. Phys.* **87**, 703 (2014).
- [79] C. Zhou, J. Kong, and H. Dai, *Phys. Rev. Lett.* **84**, 5604 (2000).
- [80] V. V. Deshpande, B. Chandra, R. Caldwell, D. S. Novikov, J. Hone, and M. Bockrath, *Science* **323**, 106 (2009).
- [81] J. Nygard, D. Cobden, M. Bockrath, P. McEuen, and P. Lindelof, *Applied Physics A* **69**, 297 (1999).
- [82] T. Ihn, *Semiconductor Nanostructures* (Oxford University Press Inc., New York, 2010).
- [83] S. J. Chorley, J. Wabnig, Z. V. Penfold-Fitch, K. D. Petersson, J. Frake, C. G. Smith, and M. R. Buitelaar, *Phys. Rev. Lett.* **108**, 036802 (2012).
- [84] T. Frey, P. J. Leek, M. Beck, A. Blais, T. Ihn, K. Ensslin, and A. Wallraff, *Phys. Rev. Lett.* **108**, 046807 (2012).
- [85] S. Ilani, L. A. K. Donev, M. Kindermann, and P. L. McEuen, *Nat. Phys.* **2**, 687 (2006).
- [86] J. Stehlik, Y.-Y. Liu, C. M. Quintana, C. Eichler, T. R. Hartke, and J. R. Petta, *Phys. Rev. Applied* **4**, 014018 (2015).
- [87] J. Gabelli, G. Fève, J.-M. Berroir, B. Plaçais, A. Cavanna, B. Etienne, Y. Jin, and D. C. Glattli, *Nano Letters* **313**, 499 (2006).
- [88] T. Frey, P. J. Leek, M. Beck, J. Faist, A. Wallraff, K. Ensslin, T. Ihn, and M. Büttiker, *Phys. Rev. B* **86**, 115303 (2012).
- [89] K. Grove-Rasmussen, H. I. Jørgensen, B. M. Andersen, J. Paaske, T. S. Jespersen, J. Nygård, K. Flensberg, and P. E. Lindelof, *Phys. Rev. B* **79**, 134518 (2009).
- [90] T. Dirks, Y.-F. Chen, N. O. Birge, and N. Mason, *Applied Physics Letters* **95**, 192103 (2009).
- [91] D. C. Ralph, C. T. Black, and M. Tinkham, *Phys. Rev. Lett.* **74**, 3241 (1995).
- [92] H. B. Callen and T. A. Welton, *Phys. Rev.* **83**, 34 (1951).
- [93] M. Büttiker, *Phys. Rev. Lett.* **65**, 2901 (1990).
- [94] M. Reznikov, M. Heiblum, H. Shtrikman, and D. Mahalu, *Phys. Rev. Lett.* **75**, 3340 (1995).
- [95] A. Kumar, L. Saminadayar, D. C. Glattli, Y. Jin, and B. Etienne, *Phys. Rev. Lett.* **76**, 2778 (1996).
- [96] H. Birk, M. J. M. de Jong, and C. Schönenberger, *Phys. Rev. Lett.* **75**, 1610 (1995).
- [97] X. Jehl, P. Payet-Burin, C. Baraduc, R. Calemczuk, and M. Sanquer, *Phys. Rev. Lett.* **83**, 1660 (1999).

- [98] T. Hoss, C. Strunk, T. Nussbaumer, R. Huber, U. Staufer, and C. Schönenberger, *Phys. Rev. B* **62**, 4079 (2000).
- [99] M. Reznikov, R. d. Picciotto, T. G. Griffiths, M. Heiblum, and V. Umansky, *Nature* **399**, 238 (1999).
- [100] M. Henny, *Shot Noise in Nanoconductors*, Ph.D. thesis, University of Basel (1998).
- [101] C. W. J. Beenakker and M. Büttiker, *Phys. Rev. B* **46**, 1889 (1992).
- [102] K. E. Nagaev, *Physics Letters A* **169**, 103 (1992).
- [103] E. V. Sukhorukov and D. Loss, *Phys. Rev. Lett.* **80**, 4959 (1998).
- [104] M. Henny, S. Oberholzer, C. Strunk, and C. Schönenberger, *Phys. Rev. B* **59**, 2871 (1999).
- [105] K. E. Nagaev, *Phys. Rev. B* **52**, 4740 (1995).
- [106] A. H. Steinbach, J. M. Martinis, and M. H. Devoret, *Phys. Rev. Lett.* **76**, 3806 (1996).
- [107] N. Bergeal, F. Schackert, L. Frunzio, D. E. Prober, and M. H. Devoret, *Applied Physics Letters* **100**, 203507 (2012).
- [108] F. N. Hooge, *IEEE Transactions on Electron Devices* **41**, 1926 (1994).
- [109] G. E. Onac, *High frequency noise detection in mesoscopic devices*, Ph.D. thesis, Technische Universiteit Delft (2005).
- [110] A. A. Clerk, M. H. Devoret, S. M. Girvin, F. Marquardt, and R. J. Schoelkopf, *Rev. Mod. Phys.* **82**, 1155 (2010).
- [111] J. Basset, H. Bouchiat, and R. Deblock, *Phys. Rev. Lett.* **105**, 166801 (2010).
- [112] R. J. Schoelkopf, P. J. Burke, A. A. Kozhevnikov, D. E. Prober, and M. J. Rooks, *Phys. Rev. Lett.* **78**, 3370 (1997).
- [113] D. C. Glatthli, P. Jacques, A. Kumar, P. Pari, and L. Saminadayar, *Journal of Applied Physics* **81**, 7350 (1997).
- [114] C. Altimiras, O. Parlavecchio, P. Joyez, D. Vion, P. Roche, D. Esteve, and F. Portier, *Phys. Rev. Lett.* **112**, 236803 (2014).
- [115] F. D. Parmentier, A. Mahé, A. Denis, J.-M. Berroir, D. C. Glatthli, B. Plaçais, and G. Fève, *Review of Scientific Instruments* **82**, 013904 (2011).
- [116] R. Deblock, E. Onac, L. Gurevich, and L. P. Kouwenhoven, *Science* **301**, 203 (2003).
- [117] E. Onac, F. Balestro, B. Trauzettel, C. F. J. Lodewijk, and L. P. Kouwenhoven, *Phys. Rev. Lett.* **96**, 026803 (2006).
- [118] E. Onac, F. Balestro, L. H. W. van Beveren, U. Hartmann, Y. V. Nazarov, and L. P. Kouwenhoven, *Phys. Rev. Lett.* **96**, 176601 (2006).

- [119] R. Aguado and L. P. Kouwenhoven, *Phys. Rev. Lett.* **84**, 1986 (2000).
- [120] S. Gustavsson, M. Studer, R. Leturcq, T. Ihn, K. Ensslin, D. C. Driscoll, and A. C. Gossard, *Phys. Rev. Lett.* **99**, 206804 (2007).
- [121] S. Gustavsson, R. Leturcq, B. Simovič, R. Schleser, T. Ihn, P. Studerus, K. Ensslin, D. C. Driscoll, and A. C. Gossard, *Phys. Rev. Lett.* **96**, 076605 (2006).
- [122] D. A. Bagrets and Y. V. Nazarov, *Phys. Rev. B* **67**, 085316 (2003).
- [123] B. L. Altshuler, A. G. Aronov, and D. E. Khmelnitsky, *Journal of Physics C: Solid State Physics* **15**, 7367 (1982).
- [124] M. Henny, H. Birk, R. Huber, C. Strunk, A. Bachtold, M. Krüger, and C. Schönenberger, *Applied Physics Letters* **71**, 773 (1997).
- [125] E. V. Sukhorukov, G. Burkard, and D. Loss, *Phys. Rev. B* **63**, 125315 (2001).
- [126] A. Cottet, W. Belzig, and C. Bruder, *Phys. Rev. B* **70**, 115315 (2004).
- [127] Y. Zhang, L. DiCarlo, D. T. McClure, M. Yamamoto, S. Tarucha, C. M. Marcus, M. P. Hanson, and A. C. Gossard, *Phys. Rev. Lett.* **99**, 036603 (2007).
- [128] S. Gustavsson, M. Studer, R. Leturcq, T. Ihn, K. Ensslin, D. C. Driscoll, and A. C. Gossard, *Phys. Rev. B* **78**, 155309 (2008).
- [129] Y. Okazaki, S. Sasaki, and K. Muraki, *Phys. Rev. B* **87**, 041302 (2013).
- [130] A. E. Hanna and M. Tinkham, *Phys. Rev. B* **44**, 5919 (1991).
- [131] S. Hershfield, J. H. Davies, P. Hyldgaard, C. J. Stanton, and J. W. Wilkins, *Phys. Rev. B* **47**, 1967 (1993).
- [132] A. Nauen, I. Hapke-Wurst, F. Hohls, U. Zeitler, R. J. Haug, and K. Pierz, *Phys. Rev. B* **66**, 161303 (2002).
- [133] A. Carmi and Y. Oreg, *Phys. Rev. B* **85**, 045325 (2012).
- [134] K. Kaasbjerg and W. Belzig, *Phys. Rev. B* **91**, 235413 (2015).
- [135] S. Gustavsson, R. Leturcq, B. Simovič, R. Schleser, P. Studerus, T. Ihn, K. Ensslin, D. C. Driscoll, and A. C. Gossard, *Phys. Rev. B* **74**, 195305 (2006).
- [136] R. Barends, *Photon-detecting superconducting resonators*, *Ph.D. thesis*, Technische Universiteit Delft (2009).
- [137] M. S. Khalil, M. J. A. Stoutimore, F. C. Wellstood, and K. D. Osborn, *Journal of Applied Physics* **111**, 054510 (2012).

A Derivations of $\lambda/4$ -Resonator Formulas

This section contains the derivations of the formulas for $\lambda/4$ -resonators stated in section 2.4.2. Step by step, the quality factors given in Eqs. (2.40) and (2.41), the input impedance of a resonator, the resonance frequency f_0 given in Eq. (2.44) and the transmission coefficient S_{21} given in Eq. (2.37) are derived. The basis for these derivations are the PhD theses of Barends [136] and Mazin [19].

A.1. Quality Factors

The quality factor is defined as

$$Q = \omega \cdot \frac{\text{energy stored in resonator}}{\text{power dissipated}} = \omega \frac{E}{P_{\text{diss}}}. \quad (\text{A.1})$$

The energy stored in a CTL has a capacitive and an inductive part. The energy in a capacitor with capacitance \tilde{C} is $E_{\tilde{C}} = 1/2\tilde{C}V^2$. The voltage in the resonator is of the waveform $V(z) = V_0 \cos(\beta z)$, as discussed in section 2.1.2 and illustrated in Fig. A.1 (b). V_0 is the maximum voltage arising at the open end. Integrating over the CTL length results in the capacitive energy stored

$$E_C = \int_0^{\lambda/4} \frac{1}{2}C \left(\frac{1}{\sqrt{2}}V_0 \cos(\beta z) \right)^2 dz = \frac{1}{8} \cdot \frac{\lambda}{4} \cdot CV_0^2, \quad (\text{A.2})$$

with the conversion from the wavenumber β to the wavelength λ given in Eq. (2.14). Note that C is the CTL capacitance per unit length and the root mean square value $1/\sqrt{2}V_0$ takes into account the oscillations in time. Likewise, the energy stored in an inductor with inductance \tilde{L} is $E_{\tilde{L}} = 1/2\tilde{L}I^2$. Again, this energy is integrated over the CTL length. Using the low-loss approximation of the characteristic impedance given in Eq. (2.17), the inductively stored energy reads

$$\begin{aligned} E_L &= \int_0^{\lambda/4} \frac{1}{2}L \left(\frac{V(z)}{Z_0} \right)^2 dz = \int_0^{\lambda/4} \frac{1}{2}C (V(z))^2 dz \\ &= E_C. \end{aligned} \quad (\text{A.3})$$

Also here, L is the CTL inductance per unit length. The CPW capacitance can be reformulated in the low-loss approximation (section 2.1.3) as follows:

$$C = \frac{\sqrt{LC}}{\sqrt{L/C}} \approx \frac{\beta}{\omega Z_0} = \frac{2\pi}{\lambda} \cdot \frac{1}{\omega Z_0}. \quad (\text{A.4})$$

Combining the results of Eqs. (A.2), (A.3) and (A.4) leads to the total energy stored in the resonator

$$E = E_C + E_L = 1/4 \cdot \lambda/4 \cdot CV_0^2 = \frac{\pi}{8} \cdot \frac{V_0^2}{\omega Z_0}. \quad (\text{A.5})$$

In the absence of any capacitive coupling of the resonator to the environment, the only loss channel is the damping α , which gives rise to the internal quality factor Q_i . According to Eq. (2.24), the power in a lossy CTL has the form $P(z) = P_0 e^{-2\alpha z}$ and accordingly, the power loss per unit length is

$$-\frac{dP}{dz} = 2\alpha P_0 e^{-2\alpha z} = 2\alpha P. \quad (\text{A.6})$$

The power $P(z)$ is related to the voltage via $P(z) = V^2(z)/Z_0$. The total dissipated power is the integral of the above expression along the resonator length:

$$\begin{aligned} P_{\text{diss}} &= \int_0^{\lambda/4} 2\alpha \frac{V^2(z)}{Z_0} dz = \frac{2\alpha}{Z_0} \int_0^{\lambda/4} \left(\frac{1}{\sqrt{2}} V_0 \cos(\beta z) \right)^2 dz \\ &= \frac{\pi}{4} \cdot \frac{\alpha V_0^2}{\beta Z_0}. \end{aligned} \quad (\text{A.7})$$

The results of Eqs. (A.5) and (A.7) allow to calculate the internal quality factor as defined in Eq. (A.1) to be

$$Q_{\text{int}} = \frac{\beta}{2\alpha}. \quad (\text{A.8})$$

A coupling with capacitance C_c at the open end to a feedline, as illustrated in Fig. A.1 (a), opens a second loss channel and gives rise to another quality factor, Q_c . The leakage current through the capacitor is $I = V_0/Z_c = V_0 \cdot i\omega C_c$. Using the root mean square current, the dissipated power is

$$P_{\text{diss}} = \left| \frac{1}{\sqrt{2}} I \right|^2 Z_0 = \frac{1}{2} Z_0 (\omega C_c V_0)^2, \quad (\text{A.9})$$

and one finds with the help of Eqs. (A.1) and (A.9) a coupling quality factor

$$Q_c = \frac{1}{8\pi (Z_0 f C_c)^2}. \quad (\text{A.10})$$

According to the definition in Eq. (A.1), quality factors are added up like resistors in parallel. The total, loaded quality factor is

$$\frac{1}{Q_l} = \frac{1}{Q_i} + \frac{1}{Q_c}. \quad (\text{A.11})$$

A.2. Input Impedance

The configuration with a feedline and a capacitively coupled $\lambda/4$ -resonators is sketched in Fig. A.1 (a). Eq. (2.23) provides an expression for the input impedance of the resonator before the capacitor:

$$Z_{\text{in}} = Z_0 \tanh(\gamma z). \quad (\text{A.12})$$

Because γ is complex, we use the relation

$$\tanh(x + i \cdot y) = \frac{1 - i \cdot \tanh(x) \cot(y)}{\tanh(x) - i \cdot \cot(y)}. \quad (\text{A.13})$$

Thus, the input impedance can be written as

$$Z_{\text{in}} = Z_0 \cdot \frac{1 - i \cdot \tanh(\alpha z) \cot(\beta z)}{\tanh(\alpha z) - i \cdot \cot(\beta z)}. \quad (\text{A.14})$$

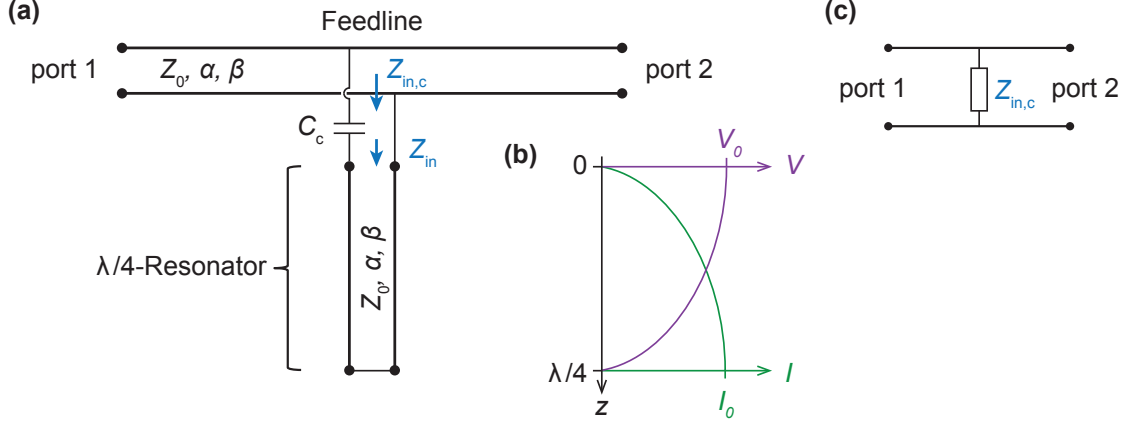


Figure A.1.: **(a)** Schematic of the feedline and the capacitively coupled $\lambda/4$ -resonator with a shorted end. In an experiment, the feedline transmission from port 1 to 2, S_{21} , is detected. **(b)** Voltage and current distributions along the resonator. **(c)** Equivalent circuit to (a) to determine Z -parameters.

Close to f_r , the resonance frequency of the first mode, Z_{in} can be approximated. With Eq. (2.14) and by introducing the relative frequency $\Delta f = f - f_r$, the argument of the \cot -term becomes

$$\beta z = 2\pi z \frac{f}{v_p} = 2\pi z \frac{\Delta f + f_r}{v_p}. \quad (\text{A.15})$$

The resonator length is known to be $z = \lambda_0/4 = v_p/(4f_r)$ [see Eq. (2.14)], and therefore

$$\begin{aligned} \beta z &= \frac{\pi}{2} \left(1 + \frac{\Delta f}{f_r} \right) \\ \cot(\beta z) &= \cot \left(\frac{\pi}{2} + \frac{\pi}{2} \cdot \frac{\Delta f}{f_r} \right). \end{aligned} \quad (\text{A.16})$$

Finally, we use that $\cot(\pi/2 + x) = -\tan(x)$ and expand $\tan(x) \approx x$ for $x \ll 1$ since we are interested in frequencies where $\Delta f/f_r \ll 1$, and get an approximate expression for the \cot -term:

$$\cot(\beta z) = -\tan \left(\frac{\pi}{2} \cdot \frac{\Delta f}{f_r} \right) \approx -\frac{\pi}{2} \cdot \frac{\Delta f}{f_r}. \quad (\text{A.17})$$

In terms of the internal quality factor $Q_i = \beta/(2\alpha)$ and with the wavenumber β as above in Eq. (A.16), the approximation for the \tanh -term is found to be

$$\begin{aligned} \alpha z &= \frac{\beta z}{2Q_i} = \frac{\pi}{4Q_i} \left(1 + \frac{\Delta f}{f_r} \right) \\ \tanh(\alpha z) &= \tanh \left[\frac{\pi}{4Q_i} \left(1 + \frac{\Delta f}{f_r} \right) \right] \approx \frac{\pi}{4Q_i} \left(1 + \frac{\Delta f}{f_r} \right). \end{aligned} \quad (\text{A.18})$$

The expansion $\tanh(x) \approx x$ used above is valid when $\alpha \ll 1$, meaning that $1/Q_i \ll 1$.

With the help of these two approximations, the resonator input impedance of Eq. (A.14) reads

$$Z_{in} \approx Z_0 \cdot \frac{\frac{4Q_i}{\pi} - i \cdot \frac{8Q_i^2}{\pi} \cdot \frac{\Delta f}{f_r}}{1 + 4Q_i^2 \left(\frac{\Delta f}{f_r} \right)^2}, \quad (\text{A.19})$$

where the second order terms in the limit $\Delta f/f_r \ll 1$ and $Q_i \gg 1$ are neglected.

Finally, by adding the series capacitor impedance, the input impedance after the resonator is

$$Z_{\text{in,c}} = \frac{1}{i \cdot 2\pi f C} + Z_{\text{in}} = Z_0 \cdot \frac{\frac{4Q_i}{\pi} - i \cdot \frac{8Q_i^2}{\pi} \cdot \frac{\Delta f}{f_r} - i \cdot \sqrt{\frac{2Q_c}{\pi}} \cdot \left[1 + 4Q_i^2 \left(\frac{\Delta f}{f_r}\right)^2\right]}{1 + 4Q_i^2 \left(\frac{\Delta f}{f_r}\right)^2}. \quad (\text{A.20})$$

A.3. Resonance Frequency

The bare resonator frequency in the absence of any coupling to the environment was defined as f_r . Now, we are going to discuss the influence of a capacitive coupling on the resonance frequency observed from outside. The requirement that the imaginary part of the impedance $Z_{\text{in,c}}$ [Eq. (A.20)] vanishes at resonance results in a quadratic equation for the relative frequency with the two solutions

$$\frac{\Delta f_{0,1}}{f_r} = -\frac{1}{\sqrt{2\pi Q_c}} \pm \sqrt{\frac{1}{2\pi Q_c} - \frac{1}{4Q_i^2}}. \quad (\text{A.21})$$

When neglecting the second term with Q_i^2 in the denominator, the two possible solutions become

$$\frac{\Delta f_0}{f_r} \approx -\sqrt{\frac{2}{\pi Q_c}} \quad \text{or} \quad \frac{\Delta f_1}{f_r} \approx 0. \quad (\text{A.22})$$

The real parts of $Z_{\text{in,c}}$ at those two frequencies are

$$\text{Re}[Z_{\text{in,c}}(\Delta f_0)] = \frac{4Z_0 Q_i}{\pi} \cdot \frac{1}{1 + \frac{8Q_i^2}{\pi Q_c}} \ll \text{Re}[Z_{\text{in,c}}(\Delta f_1)] = \frac{4Z_0 Q_i}{\pi}. \quad (\text{A.23})$$

The second requirement for a resonance is that the real part of the impedance has a minimum. Thus, the solution Δf_0 is the actually measured resonance frequency. In other words, the coupling causes the observed resonance frequency to be reduced compared to the bare resonator frequency f_r :

$$f_0 = f_r \cdot \left(1 - \sqrt{\frac{2}{Q_c \pi}}\right). \quad (\text{A.24})$$

A.4. Transmission Coefficient

In consideration of the resonance frequency shift caused by coupling discussed in the last section, the relative frequency Δf is redefined to $\Delta f = f - f_0$. Using this definition, we replace the frequency ratio $\Delta f/f_r \approx \Delta f/f_0 - \sqrt{2/(\pi Q_c)}$ in the expression for the input impedance of Eq. (A.20) and obtain

$$Z_{\text{in,c}} = Z_0 \cdot \sqrt{\frac{2Q_c}{\pi}} \cdot \frac{2Q_i \cdot \frac{\Delta f}{f_0} - i}{1 + i \cdot 2Q_i \cdot \frac{\Delta f}{f_0} - i \cdot 2Q_i \sqrt{\frac{2}{\pi Q_c}}}. \quad (\text{A.25})$$

One way to connect voltages and currents at different ports are impedance parameters or short Z -parameters. The relation of a driving current I_j at port j to the voltage at port i is

given by the parameter Z_{ij} , given that all other ports are open. Formally,

$$Z_{ij} = \left. \frac{V_i}{I_j} \right|_{I_k=0 \text{ for } k \neq j}. \quad (\text{A.26})$$

Fig. A.1 (c) shows the equivalent circuit for the resonator transmission measurements, which is used to determine the Z -parameters. With Ohm's law and since $V_1 = V_2$ in any case, one finds that

$$Z_{11} = \left. \frac{V_1}{I_1} \right|_{I_2=0} = Z_{\text{in,c}} \quad \text{and} \quad Z_{12} = \left. \frac{V_2}{I_1} \right|_{I_2=0} = Z_{\text{in,c}}. \quad (\text{A.27})$$

Due to the symmetry of the circuit, $Z_{22} = Z_{11}$ and $Z_{21} = Z_{12}$.

The transformation for the easy to calculate Z -parameters to the experimentally accessible scattering parameter goes like [10]

$$S_{21} = \frac{2Z_{21}Z_0}{(Z_{11} + Z_0)(Z_{22} + Z_0) - Z_{12}Z_{21}} = \frac{2}{2 + \frac{Z_0}{Z_{\text{in,c}}}}. \quad (\text{A.28})$$

Combining this with Eq. (A.25), one finds the transmission coefficient minimum

$$S_{21}^{\text{min}}(f = f_0) \approx \frac{Q_c}{Q_c + Q_i} \quad (\text{A.29})$$

and the general transmission coefficient

$$S_{21}(\Delta f) \approx \frac{S_{21}^{\text{min}} + i \cdot 2Q_1 \frac{\Delta f}{f_0}}{1 + i \cdot 2Q_1 \frac{\Delta f}{f_0}}. \quad (\text{A.30})$$

Spurious modes in the setup, also if their resonance frequency is quite far away from the frequency of the actual resonator, make the resonance lineshape asymmetric. This is called a Fano resonance and is taken into account by introducing the phase factor $e^{i\phi}$ into the transmission coefficient [137]:

$$S_{21}(\Delta f) = \frac{S_{21}^{\text{min}} + 2e^{i\phi} \cdot \frac{\Delta f}{f_0} + i \cdot 2Q_1 \frac{\Delta f}{f_0}}{1 + 2e^{i\phi} \cdot \frac{\Delta f}{f_0} + i \cdot 2Q_1 \frac{\Delta f}{f_0}}. \quad (\text{A.31})$$

For resonances with a bandwidth of a few MHz, it is a good assumption to approximate the (slightly frequency dependent) background attenuation and gain with a straight line in the frequency range of interest. Altogether, the amplitude of a resonator spectrum in dezibel is fitted with the function

$$|S_{21}(\Delta f)|^2[\text{dB}] = b + s \cdot \Delta f + 20 \log_{10} \left| \frac{S_{21}^{\text{min}} + 2e^{i\phi} \cdot \frac{\Delta f}{f_0} + i \cdot 2Q_1 \frac{\Delta f}{f_0}}{1 + 2e^{i\phi} \cdot \frac{\Delta f}{f_0} + i \cdot 2Q_1 \frac{\Delta f}{f_0}} \right|, \quad (\text{A.32})$$

where b is the baseline value and s its slope. In the end, there are five fit parameters used; two for the resonator (S_{21}^{min} and Q_1) and three for the setup (b , s and ϕ).

B Derivations of Stub Tuner Formulas

The stub tuner as a key circuit of this thesis is introduced in section 3.1. In this appendix, one finds derivations for the formulas, which appear in the main text. The first part of the appendix concentrates on the reflection at the low-impedance side. It is explained how a measured reflection spectrum is fitted and the expression for the bandwidth stated in Eq. (3.12) is derived. The second part concentrates on the voltage transmission from the load to the 50 Ω measurement side, which is the topic of section 3.1.7. First, the general transmission function t_V is derived and then, an approximate expression is calculated.

B.1. Reflection

B.1.1. General Expression

The stub tuner circuit is illustrated in Fig. B.1. According to the formula for a terminated transmission line in Eq. (2.22), the load impedance is transformed by the CTL of length D_1 to

$$Z_{D1} = Z_0^* \cdot \frac{Z_L + Z_0^* \tanh(\gamma D_1)}{Z_0^* + Z_L \tanh(\gamma D_1)}, \quad (\text{B.1})$$

with the propagation constant $\gamma = \alpha + i \cdot \beta$ and the wavenumber $\beta = 2\pi f \sqrt{\epsilon_{\text{eff}}}/c$. Furthermore, the open-ended CTL of length D_2 induces an impedance at the T-junction of

$$Z_{D2} = Z_0^* \coth(\gamma D_2). \quad (\text{B.2})$$

Adding these two parallel impedances leads to the input impedance of the stub tuner seen from the low-impedance side:

$$Z_{\text{in}} = e^{i\phi} \cdot \frac{Z_{D1} Z_{D2}}{Z_{D1} + Z_{D2}}. \quad (\text{B.3})$$

In the same way as for $\lambda/4$ -resonators (see section A.4), the phase factor $e^{i\phi}$ accounts for spurious setup modes, which cause an asymmetric resonance lineshape [137]. We usually design the CTLs such that their characteristic impedances are similar to the characteristic impedance of the measurement line, meaning that $Z_0^* = Z_0$.

Now, the complex reflection coefficient can be readily calculated via Eq. (2.20),

$$\Gamma = \frac{Z_{\text{in}} - Z_0}{Z_{\text{in}} + Z_0}. \quad (\text{B.4})$$

In the case of impedance matching, Z_{in} is equal to Z_0 and therefore the reflection coefficient vanishes. Minimising Γ to find the matching parameters can be done analytically for a lossless stub tuner (see section 3.1.1), but has to be done numerically in case of a finite loss α . For instance, one can use the `NMinimize` function of Mathematica.

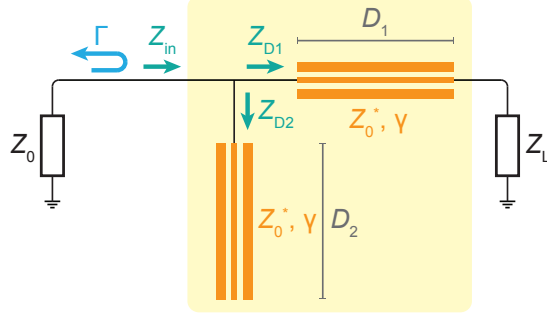


Figure B.1.: Schematic of the stub tuner (on a yellow background) with the line impedance Z_0 and the load impedance Z_L attached. Coplanar transmission lines are represented by the orange parts.

Similar to the $\lambda/4$ -resonator spectrum of section A.4, the reflection amplitude spectrum can be fitted with the function

$$|\Gamma(f)|^2[dB] = b + s \cdot (f - f_0) + 20 \log_{10} |\Gamma|, \quad (\text{B.5})$$

when measured in decibel. The setup properties are taken into account by a linear background reflection described by $b + s \cdot (f - f_0)$, with b being the background attenuation and s its slope. The frequency reference point f_0 is in principle an arbitrary frequency. We normally choose it to be the resonance frequency. The number of fit parameters sums up to seven, four for the stub tuner contribution (loss α , load R and the two lengths D_1 and D_2) and three for the background contribution (b , s and ϕ). Formulas for the two CTL parameters, the dielectric constant ϵ_{eff} and the characteristic impedance Z_0 , are given in section (2.3.1) or can be obtained from simulations.

If the stub tuner has two open ends, as it is the case in the stub tuner characterisation experiments presented in chapter 3.1.5 or when the load is a quantum dot in the Coulomb blockade regime (section 6.3.1), the impedance from the segment of length D_1 [Eq. (B.1)] simplifies to

$$Z_{D1} = Z_0^* \coth(\gamma D_1), \quad (\text{B.6})$$

and one fit parameter, R , drops out. Note that fitting the amplitude of an open stub tuner is not enough to find a unique solution. This is further discussed in section 3.1.4.

B.1.2. Lossless Stub Tuner with Large Load Resistance

Here, an approximate expression for the reflection coefficient Γ is derived in the case of a lossless stub tuner with a load resistance $R \gg Z_0$. It captures well the situation in our experiments, for which we use low-loss superconducting CTLs with $\alpha \ll 1$ and measure high resistance devices with resistances up to a megaohm.

The impedance of the terminated CTL segment given in Eq. (B.1) simplifies to

$$Z_{D1} = Z_0 \cdot \frac{R + i \cdot Z_0 \tan(\beta D_1)}{Z_0 + i \cdot R \tanh(\beta D_1)}, \quad (\text{B.7})$$

under the assumptions that $\alpha = 0$, $Z_0^* = Z_0$ and that the device impedance $Z_L = R$ is real. Moreover, the impedance of the open end after the distance D_2 becomes

$$Z_{D2} = -i \cdot Z_0 \cot(\beta D_2). \quad (\text{B.8})$$

Plugging the results of Eqs. (B.7) and (B.8) into Eq. (B.3) and neglecting the asymmetry factor leads to the stub tuner input impedance

$$Z_{\text{in}} = Z_o \cdot \frac{R \cot(\beta D_1) \cot(\beta D_2) + i \cdot Z_0 \cot(\beta D_2)}{Z_0 \cot(\beta D_1) \cot(\beta D_2) + i \cdot R \cot(\beta D_1) + i \cdot R \cot(\beta D_2) - Z_0}. \quad (\text{B.9})$$

The arguments in the *cot*-terms can be rewritten in terms of the relative frequency $\Delta f = f - f_0$ to

$$\beta D_i = \frac{2\pi f \sqrt{\epsilon_{\text{eff}}}}{c} D_i = \frac{2\pi f_0 \sqrt{\epsilon_{\text{eff}}}}{c} D_i + \frac{2\pi \Delta f \sqrt{\epsilon_{\text{eff}}}}{c} D_i, \quad (\text{B.10})$$

where D_i with $i = 1, 2$ are the CTL lengths. By using $f_0 = c/(\lambda_0 \sqrt{\epsilon_{\text{eff}}})$ and writing $D_i = \lambda_0/4 + \Delta D_i$, the argument reads

$$\beta D_i = \frac{\pi}{2} + \frac{\pi}{2} \cdot \frac{\Delta D_i}{\lambda_0/4} + \frac{2\pi \Delta f \sqrt{\epsilon_{\text{eff}}}}{c} \cdot \frac{\lambda_0}{4} + \frac{2\pi \Delta f \Delta D_i}{c}. \quad (\text{B.11})$$

As visible in Fig. 3.3 (a), the two stub lengths D_i approach $\lambda_0/4$ for large device resistances and therefore $\Delta D_i \ll 1$ in the limit $R \gg Z_0$. In addition, we are interested in frequencies close to resonance, where Δf is small, such that the last term in Eq. (B.11) can be neglected and

$$\beta D_i \approx \frac{\pi}{2} + \frac{\pi}{2} \left(\frac{\Delta D_i}{\lambda_0/4} + \frac{\Delta f}{f_0} \right). \quad (\text{B.12})$$

With this, the *cot*-terms can be expanded as follows:

$$\begin{aligned} \cot(\beta D_i) &\approx \cot \left[\frac{\pi}{2} + \frac{\pi}{2} \left(\frac{\Delta D_i}{\lambda_0/4} + \frac{\Delta f}{f_0} \right) \right] \\ &= -\tan \left[\frac{\pi}{2} \left(\frac{\Delta D_i}{\lambda_0/4} + \frac{\Delta f}{f_0} \right) \right] \\ &\approx -\frac{\pi}{2} \left(\frac{\Delta D_i}{\lambda_0/4} + \frac{\Delta f}{f_0} \right), \end{aligned} \quad (\text{B.13})$$

by using the expansion $\tan(x) \approx x$ for small x .

An expression for the lengths ΔD_i is found by applying the matching condition, which requires that $Z_{\text{in}} = Z_0$. Equating the real and imaginary parts of Z_{in} given in Eq. (B.9) results in the two equations

$$\begin{aligned} \text{Real part: } \frac{Z_0}{R} [\cot(\beta_0 D_1) \cot(\beta_0 D_2) - 1] &= \cot(\beta_0 D_1) \cot(\beta_0 D_2) \\ \text{Imaginary part: } \frac{R}{Z_0} [\cot(\beta_0 D_1) + \cot(\beta_0 D_2)] &= \cot(\beta_0 D_2). \end{aligned} \quad (\text{B.14})$$

Here, $\beta_0 = 2\pi/\lambda_0$ is the wavenumber at the resonance frequency. By solving for $\cot(\beta_0 D_1)$ and $\cot(\beta_0 D_2)$ in the limit $\frac{R}{Z_0} \gg 1$, one sees that at matching

$$\cot(\beta_0 D_1) \approx -\cot(\beta_0 D_2) \approx \sqrt{\frac{Z_0}{R}}. \quad (\text{B.15})$$

Comparing this with Eq. (B.13) at matching ($\Delta f = 0$) gives

$$\cot(\beta_0 D_i) \approx -\frac{\pi}{2} \frac{\Delta D_i}{\lambda_0/4} \approx \pm \sqrt{\frac{Z_0}{R}}. \quad (\text{B.16})$$

Or in other words

$$D_i \approx \frac{\lambda_0}{4} \cdot \left(1 \mp \frac{2}{\pi} \sqrt{\frac{Z_0}{R}} \right), \quad (\text{B.17})$$

which is in agreement with the solutions derived in the main text [Eqs. (3.8) and (3.9)] when using that for large $x = \sqrt{R/Z_0}$, $\arctan(x)$ can be expanded in first order as

$$\arctan(x) = \frac{\pi}{2} - \arctan\left(\frac{1}{x}\right) \approx \frac{\pi}{2} - \frac{1}{x}. \quad (\text{B.18})$$

By solving Eq. (B.16) for ΔD_i and plugging the result into Eq. (B.13), the *cot*-terms given in Eq. (B.13) can be written as

$$\cot(\beta D_i) \approx \pm \sqrt{\frac{Z_0}{R}} - \frac{\pi}{2} \frac{\Delta f}{f_0}. \quad (\text{B.19})$$

In the following, we use the expression with the plus sign for D_1 and the minus sign for D_2 , corresponding to the solution with $D_1 < D_2$.

Plugging the approximation of Eq. (B.19) into the stub tuner input impedance of Eq. (B.9), one ends up with

$$\begin{aligned} Z_{in} &\approx Z_0 \cdot \frac{\left(\frac{\pi}{2}\right)^2 \left(\frac{\Delta f}{f_0}\right)^2 - i\frac{\pi}{2} \frac{Z_0}{R} \frac{\Delta f}{f_0} - \frac{Z_0}{R} - i\frac{Z_0}{R} \sqrt{\frac{Z_0}{R}}}{\frac{Z_0}{R} \left(\frac{\pi}{2}\right)^2 \left(\frac{\Delta f}{f_0}\right)^2 - i\pi \frac{\Delta f}{f_0} - \frac{Z_0}{R} - \left(\frac{Z_0}{R}\right)^2} \\ &\approx Z_0 \cdot \frac{\left(\frac{\pi}{2}\right)^2 \left(\frac{\Delta f}{f_0}\right)^2 - \frac{Z_0}{R} - i\frac{\pi}{2} \frac{Z_0}{R} \frac{\Delta f}{f_0}}{\frac{Z_0}{R} \left(\frac{\pi}{2}\right)^2 \left(\frac{\Delta f}{f_0}\right)^2 - \frac{Z_0}{R} - i\pi \frac{\Delta f}{f_0}}, \end{aligned} \quad (\text{B.20})$$

where in the second line the last terms in the numerator and denominator are dropped.

Eventually, it is possible to give an approximate expression for the reflection coefficient Γ around the resonance:

$$\begin{aligned} \Gamma &= \frac{Z_{in} - Z_0}{Z_{in} + Z_0} \\ &\approx \frac{\left(\frac{\pi}{2}\right)^2 \left(\frac{\Delta f}{f_0}\right)^2 \left(1 - \frac{Z_0}{R}\right) + i\frac{\pi}{2} \frac{\Delta f}{f_0} \left(2 - \frac{Z_0}{R}\right)}{\left(\frac{\pi}{2}\right)^2 \left(\frac{\Delta f}{f_0}\right)^2 \left(1 + \frac{Z_0}{R}\right) - 2\frac{Z_0}{R} - i\frac{\pi}{2} \frac{\Delta f}{f_0} \left(2 + \frac{Z_0}{R}\right)} \\ &\approx \frac{\left(\frac{\pi}{2}\right)^2 \left(\frac{\Delta f}{f_0}\right)^2 + i\pi \frac{\Delta f}{f_0}}{\left(\frac{\pi}{2}\right)^2 \left(\frac{\Delta f}{f_0}\right)^2 - 2\frac{Z_0}{R} - i\pi \frac{\Delta f}{f_0}}, \end{aligned} \quad (\text{B.21})$$

where again the limit $Z_0/R \ll 1$ is applied in the last line.

The resonance bandwidth is defined as the full width at half maximum (FWHM) of the power spectrum $|\Gamma|^2$. The substitution $y = \left(\frac{\pi}{2} \frac{\Delta f}{f_0}\right)^2$ applied to Eq. (B.21) leads to

$$\begin{aligned}\Gamma &= \frac{y + i \cdot 2\sqrt{y}}{y - 2\frac{Z_0}{R} - i \cdot 2\sqrt{y}} \\ |\Gamma|^2 &= \frac{y^2 + 4y}{\left(y - 2\frac{Z_0}{R}\right)^2 + 4y}.\end{aligned}\tag{B.22}$$

Setting $|\Gamma|^2 = \frac{1}{2}$ and solving for y gives

$$y_{1/2} = -2 \pm 2\sqrt{1 + \left(\frac{Z_0}{R}\right)^2}.\tag{B.23}$$

According to the definition, y has to be positive. In addition, the square root can be expanded as $\sqrt{1+u} \approx 1 + \frac{1}{2}u$ for small u , which results in

$$y_{1/2} = \left(\frac{\pi}{2} \cdot \frac{\Delta f_{1/2}}{f_0}\right)^2 \approx \left(\frac{Z_0}{R}\right)^2.\tag{B.24}$$

In this framework, $\Delta f_{1/2}$ is the half width at half maximum and the FWHM is the double of it. In summary, one obtains the reflection bandwidth (FWHM) for a lossless stub tuner

$$\Delta f_{\text{FWHM}} = f_0 \cdot \frac{4}{\pi} \cdot \frac{Z_0}{R},\tag{B.25}$$

in the case of large $R \gg Z_0$. Consequently, the load quality factor reads

$$Q_L = \frac{f_0}{\Delta f_{\text{FWHM}}} = \frac{\pi}{4} \cdot \frac{R}{Z_0}.\tag{B.26}$$

B.2. Transmission

This section refers to the discussion of the stub tuner transmission for the high-impedance device side to the low-impedance measurement side found in section 3.1.7. In particular, the derivation for the wave coefficients of the CTLs stated in Eq. (3.16) is shown and the approximation of the transmission function leading to Eq. (3.19) is explained.

B.2.1. Voltage Coefficients

A schematic of the examined stub tuner circuit is shown in Fig. B.2. As a result of the telegraph equation (see section 2.1.1), the voltages and current in the left CTL segment take on the waveform from Eqs. (2.8) and (2.12):

$$\begin{aligned}V(x)_1 &= V_1^+ e^{-\gamma x} + V_1^- e^{\gamma x} \\ I(x)_1 &= \frac{V_1^+}{Z_0^*} e^{-\gamma x} - \frac{V_1^-}{Z_0^*} e^{\gamma x}.\end{aligned}\tag{B.27}$$

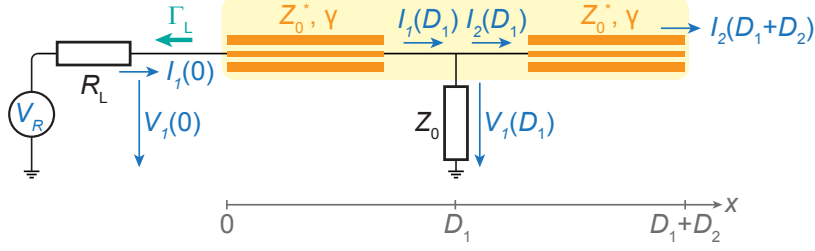


Figure B.2.: Schematic of the stub tuner on a yellow background with an attached load resistance R and measurement line resistance Z_0 . The two CTL segments are illustrated in orange. Voltages and currents at different places are indicated in blue.

The coefficients labelled with a plus (minus) correspond to right-moving (left-moving) waves, respectively. Likewise, the voltages and currents in the right, open-ended CTL are

$$\begin{aligned} V_2(x) &= V_2^+ e^{-\gamma x} + V_2^- e^{\gamma x} \\ I_2(x) &= \frac{V_2^+}{Z_0^*} e^{-\gamma x} - \frac{V_2^-}{Z_0^*} e^{\gamma x}. \end{aligned} \quad (\text{B.28})$$

The four voltage coefficients V_1^+ , V_2^- , V_2^+ and V_1^- are fixed by four boundary conditions. First, we require that the current at the open end vanishes:

$$I_2(D_1 + D_2) = 0. \quad (\text{B.29})$$

The voltage on the loaded end is set by Ohm's law to

$$V_1(0) = V_R - R I_1(0). \quad (\text{B.30})$$

Furthermore, the voltage has to be continuous at the connection of the two arms:

$$V_1(D_1) = V_2(D_1). \quad (\text{B.31})$$

At last, Kirchhoff's current law implies that at the junction between the two arms

$$I_1(D_1) = I_2(D_1) + \frac{V_1(D_1)}{Z_0}. \quad (\text{B.32})$$

What remains is a lengthy calculation with the resulting voltage coefficients (when $Z_0^* = Z_0$)

$$\begin{aligned} V_1^+ &= \frac{V_R}{R + Z_0} \cdot \frac{Z_0 \cdot e^{2\gamma D_1} \cdot [1 + 2 \cdot \coth(\gamma D_2)]}{R - Z_0 + (R + Z_0) \cdot e^{2\gamma D_1} \cdot [1 + 2 \cdot \coth(\gamma D_2)]} \\ V_1^- &= \frac{V_R Z_0}{Z_0 - R - (R + Z_0) \cdot e^{2\gamma D_1} \cdot [1 + 2 \cdot \coth(\gamma D_2)]} \\ V_2^+ &= \frac{V_R Z_0 e^{\gamma(2D_1+D_2)}}{(R + Z_0) e^{2\gamma D_1} [\sinh(\gamma D_2) + 2 \cosh(\gamma D_2)] + (R - Z_0) \sinh(\gamma D_2)} \\ V_2^- &= \frac{V_R Z_0 e^{-\gamma D_2}}{(R + Z_0) e^{2\gamma D_1} [\sinh(\gamma D_2) + 2 \cosh(\gamma D_2)] + (R - Z_0) \sinh(\gamma D_2)}. \end{aligned} \quad (\text{B.33})$$

These coefficients directly lead to the voltage transmission function stated in Eq. (3.16):

$$t_V(f) = \frac{V(D_1)}{V_R} = \frac{2Z_0}{R + Z_0} \cdot \frac{e^{\gamma D_1} \coth(\gamma D_2)}{\Gamma_L + e^{2\gamma D_1} \cdot [1 + 2 \coth(\gamma D_2)]}, \quad (\text{B.34})$$

where $\Gamma_L = (R - Z_0)/(R + Z_0)$ is the reflection coefficient before the stub tuner.

B.2.2. Lossless Stub Tuner with Large Load Resistance

An approximation of the transmission function t_V of Eq. (B.34) for a lossless stub tuner in the limit $R \gg Z_0$ and $\Delta f \ll f_0$ is achieved in the same way as before for the reflection coefficient (see section B.1.2). Here, the relative frequency $\Delta f = f - f_0$, with f_0 being the resonance frequency.

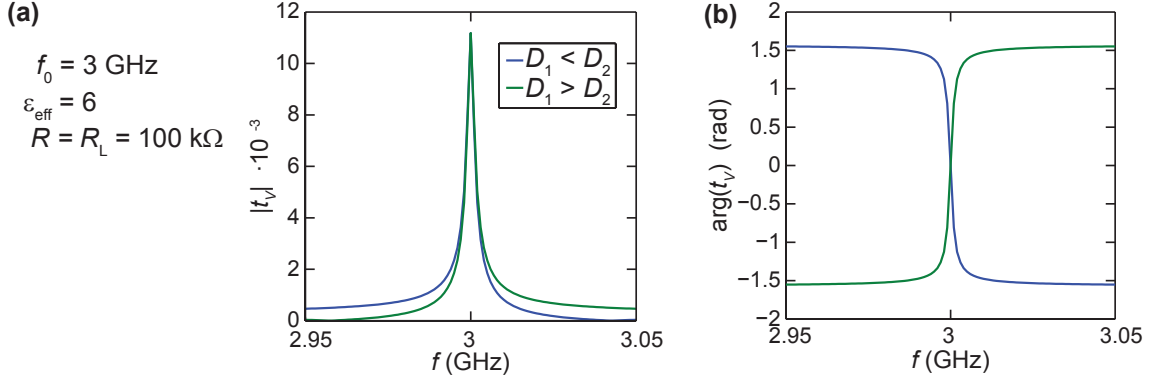


Figure B.3.: Large load resistance approximation of the transmission spectrum of a lossless stub tuner for a load of $R = 100$ kΩ. The circuit is matched to 100 kΩ at 3 GHz. The blue (green) curve correspond to the solutions with the stub tuner length D_1 longer (shorter) than D_2 , respectively. **(a)** Amplitude and **(b)** phase.

The propagation constant appearing in Eq. (B.34) is in general $\gamma = \alpha + i \cdot \beta$. For a lossless stub tuner ($\alpha = 0$), one can use that $\coth(ix) = -i \cdot \cot(x)$. According to Eq. (B.19), the resulting \cot -term can be approximated as

$$\cot(\beta D_2) \approx \pm \sqrt{\frac{Z_0}{R}} - \frac{\pi}{2} \cdot \frac{\Delta f}{f_0}, \quad (\text{B.35})$$

As seen in Eqs. (3.8) and (3.9), there are two kinds of solutions for the stub tuner lengths. The plus (minus) signs correspond to the solution with $D_1 < D_2$ ($D_1 > D_2$), respectively. Moreover, inserting ΔD_1 from Eq. (B.16) into Eq. (B.12) tell us that

$$\beta D_1 \approx \frac{\pi}{2} \pm \sqrt{\frac{Z_0}{R}} + \frac{\pi}{2} \cdot \frac{\Delta f}{f_0}. \quad (\text{B.36})$$

This allows to expand the exponentials as follows:

$$e^{i \cdot \beta D_1} \approx i$$

$$e^{i \cdot 2\beta D_1} \approx -1 \cdot \left[1 + i \cdot \pi \frac{\Delta f}{f_0} \pm i \cdot 2 \sqrt{\frac{Z_0}{R}} - \frac{1}{2} \cdot \left(\pi \frac{\Delta f}{f_0} \pm 2 \sqrt{\frac{Z_0}{R}} \right)^2 \right]. \quad (\text{B.37})$$

By inserting Eqs. (B.35) and (B.37) into Eq. (B.34) and neglecting the highest order terms, the transmission function simplifies to

$$t_V(\Delta f) \approx \frac{2Z_0}{R} \cdot \frac{\frac{\pi}{2} \cdot \frac{\Delta f}{f_0} \mp \sqrt{\frac{Z_0}{R}}}{\pm 4\frac{Z_0}{R} + i \cdot 2\pi \frac{\Delta f}{f_0}}. \quad (\text{B.38})$$

Note that still, the upper (lower) signs are valid in the case $D_1 < D_2$ ($D_1 > D_2$), respectively. As illustrated in Fig. B.3 (a), the amplitude of the transmission spectrum is slightly asymmetric and a sign change mirrors the amplitude with respect to f_0 . Fig. B.3 (b) shows that the phase change gets reversed by a change of sign.

The amplitude squared value of the transmission function can immediately be derived from Eq. (B.38) as being

$$|t_V(\Delta f)|^2 \approx \frac{Z_0}{4R} \cdot \frac{1}{1 + \left(\frac{\pi}{2} \cdot \frac{R}{Z_0} \cdot \frac{\Delta f}{f_0}\right)^2}, \quad (\text{B.39})$$

without the highest order terms in the numerator.

C Fabrication Recipes

To complete the fabrication chapter 4, the interested reader finds here detailed, step-by-step descriptions of the fabrication recipes developed and used during the PhD. As mentioned at the end of section 4.2.2, two different fabrication orders are applied: either CNTs are stamped and contacted first and the stub tuner is added afterwards, or the stub tuner is prepared first and the last step is to stamp and contact CNTs.

CNT stamping

Substrate	<ul style="list-style-type: none"> • Si with 170 nm thermal oxide on top
Patterning pillars	<ul style="list-style-type: none"> • E-beam lithography with PMMA/HSQ bilayer <ul style="list-style-type: none"> - Spin coat PMMA (thickness 1 μm) - Bake at 180 °C for 10 min. - Spin coat HSQ (6000 rpm, 60 s) - Bake at 90 °C for 5 min. - HSQ is a negative e-beam resist - Acceleration voltage 20 kV, aperture 120 μm - Area dose 200 $\mu\text{C}/\text{cm}^2$ • Developing <ul style="list-style-type: none"> - 25 s in TMAH (25 % solution) - Stop in water and then IPA, blow-dry with N_2
PMMA removal	<ul style="list-style-type: none"> • Plasma etching in Oxford reactive ion etching machine (RIE) <ul style="list-style-type: none"> - Parameters: O_2 16 sccm, 250 mTorr, 100 W, time 10 min.
SiO_2 etching	<ul style="list-style-type: none"> • Wet-etching with buffered HF (5 %) <ul style="list-style-type: none"> - Time 7 min., etch rate ~ 35 nm/min, (also removes HSQ)
Si etching	<ul style="list-style-type: none"> • Plasma etching in Oxford RIE <ul style="list-style-type: none"> - Parameters: SF_6 13 sccm, O_2 5 sccm, 75 mTorr, 100 W - Time 5 min., resulting pillar height ~ 4 μm
Wafer cleaving	<ul style="list-style-type: none"> • Cleave wafer to have one pillar area per piece • Sonicate thoroughly to remove any particles on the surface
Catalyst solution	<ul style="list-style-type: none"> • Recipe from Jörg Furrer [40] <ul style="list-style-type: none"> - 30 mg of Al_2O_3, 93 mg of $\text{Fe}(\text{NO}_3)_3 \cdot 9\text{H}_2\text{O}$ and 27 mg of MoO_2Cl_2, dissolved in 60 ml IPA

	<ul style="list-style-type: none"> - High-power sonication in cell disrupter, at least 1 h sonication time - Spin coat one drop of catalyst on the stamps with 4000 rpm for 30 s and repeat this 5 times to get a high CNT density
CVD growth	<ul style="list-style-type: none"> • Heat furnace to 950 °C under Ar flow (1500 sccm) and H₂ flow (500 sccm) • Growth: replace Ar by CH₄ (1000 sccm) for 10 min. • Cooldown under Ar and H₂ flow again until $T < 320^{\circ}\text{C}$
CNT stamping	<ul style="list-style-type: none"> • Mount target substrate in mask aligner (Süss MicroTec) • Glue stamp substrate on a glass plate with a drop of PMMA • Align the two substrates with the optical microscope to be on top of each other • Press them together until "WEC"=Ok, then move the stage 5 additional turns up

Bottom Gates Covered with Silicon Nitride

Substrate	<ul style="list-style-type: none"> • Undoped Si ($\rho > 5000 \Omega\text{cm}$) with 170 nm of thermal oxide on top
Patterning gates	<ul style="list-style-type: none"> • E-beam lithography with PMMA (thickness 300 nm) <ul style="list-style-type: none"> - Acceleration voltage 20 kV - Aperture 10 μm/120 μm for small/big markers - Area dose 240 $\mu\text{C}/\text{cm}^2$, line dose 1200 pC/cm² • Developing <ul style="list-style-type: none"> - 60 s in MIBK/IPA (1:3), stop in IPA, blow-dry with N₂
Evaporation	<ul style="list-style-type: none"> • In Sharon e-beam evaporator • 5 nm Ti and 30 nm Au
Lift-off	<ul style="list-style-type: none"> • In acetone (can be heated up to 50 °C to speed up) • Sonicate in acetone and IPA for cleaning
Si ₃ N ₄ deposition	<ul style="list-style-type: none"> • Plasma enhanced CVD (PECVD), done at PSI, thickness 50 nm
Si ₃ N ₄ etching	<ul style="list-style-type: none"> • E-beam lithography with PMMA (thickness 500 nm) <ul style="list-style-type: none"> - Acceleration voltage 20 kV - Area dose 200 $\mu\text{C}/\text{cm}^2$, aperture 10 μm • Developing <ul style="list-style-type: none"> - 60 s in MIBK/IPA (1:3), stop in IPA, blow-dry with N₂ • Plasma etching in Oxford RIE

- Parameters: CHF₃ 25 sccm, O₂ 4 sccm, 50 mTorr, 50 W
- Time 2 min. 30 s, Si₃N₄ etch rate ~ 30 nm/min

Stub tuners and resonators

Covering CNT area	<ul style="list-style-type: none"> • E-beam lithography with PMMA/HSQ bilayer <ul style="list-style-type: none"> - Spin coat PMMA (thickness 600 nm) - Bake at 180 °C for 10 min. - Spin coat HSQ (6000 rpm, 60 s) - Bake at 90 °C for 5 min. - HSQ is a negative e-beam resist - Acceleration voltage 20 kV, aperture 120 μm - Area dose 200 μC/cm² • Developing <ul style="list-style-type: none"> - 25 s in TMAH (25 % solution) - Stop in water and then IPA, blow-dry with N₂ • Remove PMMA in the RIE with an O₂ plasma <ul style="list-style-type: none"> - Parameters: O₂ 16 sccm, 250 mTorr, 100 W, 9 min.
Nb sputtering	<ul style="list-style-type: none"> • AJA magnetron sputtering machine <ul style="list-style-type: none"> - Parameters: Ar 40 sccm, 4 mTorr, 160 W - Stage rotation on in case the sample is large - Thickness 100 – 150 nm
Stub tuners and resonators are either patterned by e-beam or UV lithography	
E-beam lithography	<ul style="list-style-type: none"> • Resist PMMA, thickness 600 nm <ul style="list-style-type: none"> - Acceleration voltage 20 kV, aperture 60 μm - Area dose 130 μC/cm² • Developing <ul style="list-style-type: none"> - 60 s in MIBK/IPA (1:3), stop in IPA, blow-dry with N₂
UV lithography	<ul style="list-style-type: none"> • Resist AZ 1512 HS <ul style="list-style-type: none"> - Spin coating with 6000 rpm for 45 s - Baking at 100 °C for 60 s • UV exposure in mask aligner (Süss MicroTec) <ul style="list-style-type: none"> - Wavelength 365 nm (channel 1), time 1.2 s - Power 260 W, intensity 32 mW/cm² • Developing <ul style="list-style-type: none"> - 17 s in MIF 726, stop in water for 30 s, blow-dry
Nb etching	<ul style="list-style-type: none"> • Plasma etching in inductively coupled plasma (ICP) machine

- Parameters: Ar 25 sccm, Cl₂ 40 sccm, 1 Pa, ICP power 100 W, RF power 125 W
- Time 50 s, Nb etch rate ~ 4 nm/s

The contact line from the stub tuner to the device is either done before or after Nb sputtering. If done before with Pd or Au, there is an ohmic contact right away. If the stub tuner has to be contacted afterwards, a plasma etching is required to remove some oxide on the Nb surface, as described below:

Contacts on Nb	<ul style="list-style-type: none"> • E-beam lithography with PMMA (thickness 500 nm) • Oxide etching and metal deposition in the e-beam evaporator (Sharon) <ul style="list-style-type: none"> - Ar plasma etching for 30 s, recipe number 2 - Pd deposition: 50 (80) nm are enough to contact 100 (150) nm-high Nb
----------------	--

Contacting CNTs (and at the same time also the bottom gates)

Patterning	<ul style="list-style-type: none"> • E-beam lithography with ZEP 520A, diluted with anisole to achieve a thickness of 300 nm <ul style="list-style-type: none"> - Spin coating: speed 4000 rpm, time 40 s - Baking at 180 °C for 3 min. • E-beam writing with 10 μm aperture <ul style="list-style-type: none"> - For large trapezoidal undercut (important for lift-off of thermally or e-beam evaporated materials, in our case Pd, Ti, Au and Pb): Acceleration voltage 10 kV, area dose 34 μC/cm² - For vertical resist profile (important for sputtered materials, in our case Ti and Nb): Acceleration voltage 20 kV, area dose 68 μC/cm² • Developing <ul style="list-style-type: none"> - 60 s in pentylacetate and 10 s in MIBK/IPA (9:1) - Stop in IPA (for 20 s), blow-dry with N₂
------------	--

In the following, there are explanations for the different metals and layered metal systems we used to contact CNTs:

Palladium	<ul style="list-style-type: none"> • Thermal evaporation in the BesTec machine <ul style="list-style-type: none"> - Chamber cooled to -180 °C, sample head cooled to -30 °C - Source at 1510 °C
-----------	---

	<ul style="list-style-type: none"> - Evaporation rate $\sim 0.1 \text{ \AA/s}$, thickness $\sim 40 \text{ nm}$
Titanium/gold	<ul style="list-style-type: none"> • E-beam evaporation in the Sharon machine - First 10 nm of Ti, rate $0.5 - 1 \text{ \AA/s}$ - Then Au with a rate $\sim 1 \text{ \AA/s}$, thickness $30 - 60 \text{ nm}$
Titanium/ niobium	<ul style="list-style-type: none"> • Sputtering in the AJA machine - Parameters for Ti: Ar 35 sccm, 5 mTorr, 20 W, time 18 min. $\rightarrow 4.3 \text{ nm}$ - Parameters for Nb: Ar 40 sccm, 4 mTorr, 160 W, \rightarrow thickness $\sim 60 \text{ nm}$
Palladium/lead/ indium	<ul style="list-style-type: none"> • E-beam evaporation in the Balzers machine - Pd: at a head temperature $< -40^\circ\text{C}$, rate 0.3 \AA/s, thickness 4.5 nm - Pb: at a head temperature $< -90^\circ\text{C}$, high rate $1.5 - 1.8 \text{ \AA/s}$, thickness 110 nm - In: at a head temperature $< -90^\circ\text{C}$, rate $0.6 - 0.8 \text{ \AA/s}$, thickness 20 nm
Lift-off	<ul style="list-style-type: none"> • The same procedure applies for all materials apart from Pb, for which everything has to be done at room temperature and accordingly for a longer time, owing to the low melting point of lead and indium. - 15 min. in NMP at $70 \text{ }^\circ\text{C}$ - Blow surface with a syringe to remove metal residues - 30 min. in acetone at $50 \text{ }^\circ\text{C}$ (to remove NMP) - Rinse with IPA and blow-dry with N_2

D List of Setup Components

As a supplementary to chapter 5, the following table lists all components of the cryogenic measurement setup and the used instruments in a rather random order. An illustrative sketch is given in Fig. 5.2, showing where the different components are placed.

	Brand and part number	Specifications
Cryostat	Oxford Triton 200 cryo-free dilution refrigerator	Base temperature 20 mK
Magnet	Oxford 3D vector magnet	Maximum field strength in - x-direction: 1 T - y-direction: 1 T - z-direction: 6 T
Directional coupler	Fairview microwave MC 2104-20	Frequency range 1 – 4 GHz
Bias tee	Mini-Circuits ZFBT-6GW+	Original frequency range 0.1 – 6 GHz, capacitance lowered to 22 pF
Circulator	QuinStar CTD0304KC	Frequency range 2.75 – 3.25 GHz
Low-pass filter on the DC side of the bias tee	Mini-Circuits VLFX-80	Pass-band DC - 80 MHz
Low-temperature amplifier	Low Noise Factory LNF-LNC1_12A	Frequency range 1–12 GHz, gain \sim 35 dB
First room-temperature amplifier	Miteq AMF-3F-01000400-08-10P	Frequency range 1–4 GHz, gain \sim 35 dB
Second room-temperature amplifier	Miteq NSP1000-NVG	Frequency range 0.1–10 GHz, gain \sim 35 dB
Pi-filters in break-out box	Tusonix 4201-001LF	Pass-band DC - 10 MHz
DC wires	Constantan loom	24 \times 2 wires (twisted pairs)
Coaxial cable down to MC plate	UT85	Centre and outer conductors stainless steel, operating frequency $<$ 18 GHz

Coaxial cable from MC plate to puck	UT85	Centre and outer conductors copper, operating frequency < 18 GHz
Coaxial cable inside puck	Huber+Suhner EZ_47_TP_M17	Operating frequency < 100 GHz
Sample holder PCB	Designed with Design-Spark PCB, ordered from Probst Hightech	Substrate: Rogers RO4003C metals: Cu 40 – 43 μm , Ni 3 – 6 μm , Au 50-100 nm
PCB mount SMP connectors	Rosenberger 19K101-270L5	Material brass (gold plated), male
PCB mount DC connectors (Nano-connector)	Omnetics A42046-001 (MNPO-25-DD-C-ETH-M)	25 pins, male

Measurement instruments

Vector network analyser	R&S ZNB8	Frequency range 0.1 – 8.5 GHz
Signal and spectrum analyser	R&S FSW8	Frequency range 2 Hz – 8 GHz
Digital multimeter	Agilent 34410A	For DC measurements
I/V-converter	SP 938	Feedback resistance 10^7 or $10^8 \Omega$, home-made by the electronics workshop
Voltage DAC	SP 927	8 channel voltage source, home-made by the electronics workshop

Curriculum Vitae

Thomas Hasler

Born on 27 August 1987 in Wolhusen (LU, Switzerland)

Education

- 2012–2016 *PhD in experimental physics at the University of Basel*
- Dissertation in the group of Prof. C. Schönenberger:
“Microwave Noise Detection of a Quantum Dot with Stub Impedance Matching”
- 2010–2012 *Master of Science in Physics at ETH Zürich*
- Master thesis in the group of Prof. K. Ensslin and Prof. T. Ihn: “The effect of processing and resonators on the magneto-transport in high-mobility wafers”
 - Project thesis in the group of Prof. K. Ensslin and Prof. T. Ihn: “Quantum Capacitance Measurements with an AlGaAs Heterostructure”
- 2006–2010 *Bachelor of Science in Physics at ETH Zürich*
- 2000–2006 *Matura at Kantonsschule Willisau (LU)*

Positions

- 2012–2016 *Teaching assistant for physics at the University of Basel*

Publications

Publications

- *Electrolyte gate dependent high-frequency measurement of graphene field-effect transistor for sensing applications*
W. Fu, M. El Abbassi, T. Hasler, M. Jung, M. Steinacher, M. Calame, C. Schönenberger, G. Puebla-Hellmann, S. Hellmüller, T. Ihn, and A. Wallraff, [Applied Physics Letters](#) **104**, 013102 (2014).
- *Clean carbon nanotubes coupled to superconducting impedance-matching circuits*
V. Ranjan, G. Puebla-Hellmann, M. Jung, T. Hasler, A. Nunnenkamp, M. Muoth, C. Hierold, A. Wallraff, and C. Schönenberger, [Nat. Commun.](#) **6**, 7165 (2015).
- *Shot Noise of a Quantum Dot Measured with Gigahertz Impedance Matching*
T. Hasler, M. Jung, V. Ranjan, G. Puebla-Hellmann, A. Wallraff, and C. Schönenberger, [Phys. Rev. Applied](#) **4**, 054002 (2015).

Talk

- *Superconducting impedance matching circuit to measure carbon nanotube quantum dots at GHz frequencies*
Talk at the QSIT junior meeting, Passugg, 13 June 2014

Poster Contributions

- *Carbon nanotube quantum dots coupled to a stub-tuner impedance matching circuit*
T. Hasler, M. Jung, V. Ranjan, G. Puebla-Hellmann, A. Wallraff, and C. Schönenberger, Poster at the conference “Condensed Matter in Paris 2014”, Paris, 25 August 2014
- *Noise measurements of carbon nanotube quantum dots at GHz frequencies*
T. Hasler, M. Jung, V. Ranjan, G. Puebla-Hellmann, A. Wallraff, and C. Schönenberger, Poster at the conference “IWEPNM”, Kirchberg, 9 March 2015

Acknowledgements

There are many people who played an important role during the PhD time by some means or other and who deserve to be mentioned here.

Special thanks go to my thesis supervisor Prof. Christian Schönenberger. I am very grateful that I could be part of his group, use the lab facilities he provided, attend several conferences and profit from his remarkable physics and electronics knowledge and intuition. He enabled a unique, exciting possibility to get in touch with cutting-edge research. His amazing guidance and advice during our weekly project meetings are well appreciated and helped a lot to push the RF project forward. I am still surprised with how much enthusiasm and how fast and reliably he was caring about all emerging issues. Seeing this effort is a motivation for me and the other group members to follow his example.

I want to express my gratitude to the two referees Prof. Thomas Ihn and Dr. Fabien Portier for taking the time to study my thesis and to take part in the defence. It was a honour to have you in the PhD committee.

Both referees played already an important role as collaborators in earlier times. Thomas Ihn and his student Sarah Hellmüller introduced us to the concept of stub impedance matching at the project start. Later on, Fabien Portier and his student Chloé Rolland were sharing with us their experience on planar LC matching circuits, in particular by sending us their Sonnet simulation file. Another fruitful collaboration was with Prof. Takis Kontos and his group members Jay Viennot and Laure Bruhat. They learned us how they are stamping carbon nanotubes on substrates containing a microwave circuit, which became a crucial step in our fabrication process. Furthermore, I thank Christopher Wild, Dario Marty and Prof. Jens Gobrecht from the PSI and Alexander Stettler from D-BSSE of ETH in Basel for depositing silicon nitride on our samples.

While writing the dissertation, I was extremely grateful for Péter Makk's thorough proof-reading. He pointed out many weaknesses in the text and made very useful suggestions for improvements. Moreover, I thank Vishal Ranjan and Mihai-Cezar Harabula for their helpful comments.

The results in this thesis would not have been possible without the invaluable effort of all people working on the RF project. This includes our postdoc Minkyung Jung with his large lab experience and tremendous dedication to the project, our short-time collaborator Gabriel Puebla-Hellmann, who initiated on-chip stub impedance matching with superconducting circuits during his PhD in the group of Prof. Andreas Wallraff at ETH Zürich, and the two colleagues Vishal Ranjan and Mihai-Cezar Harabula.

In one way or another, I am indebted to all former and current members of the nanoelectronics group. These are: Alexey Tarasov, Andreas Baumgartner, Anton Vladyka, Axel Fanget, Christian Jünger, Clewin Handschin, Cornelia Nef, Frank Freitag, Gábor Fábrián, Gulibustan Abulizi, Jan Brunner, Jan Overbeck, Jens Schindele, Jörg Gramich, Julia Samm, Kishan Thodkar, Lujun Wang, Maria El Abbassi, Masoud Baghernejad, Mathias Wipf, Matthias Bräuningner, Michel Calame, Mihai-Cezar Harabula, Minkyung Jung, Péter Makk, Peter Rick-

haus, Ralph Stoop, Romain Maurand, Samuel d'Hollosy, Simon Zihlmann, Stefan Nau, Toni Fröhlich, Vishal Ranjan and Wangyang Fu. All these people contributed to the great group atmosphere and supported me in the lab. Apart from the time at the university, I really enjoyed the trips to the mountains at leisure time with some of the group members.

Furthermore, my thanks go to the department staff for providing excellent service. I want to mention in particular Michael Steinacher from the electronics workshop, Sascha Martin, Patrick Stöcklin, Daniel Sacker and Dominik Sifrig from the mechanical workshop, and Barbara Kammermann and Astrid Kalt from the secretary.

Last but not least, I am very grateful for the constant support I received from my parents Monika and Georges Hasler in all private matters and who made it actually possible that I could go to university.